SYNTHESIS AND CHARACTERIZATION OF TEP-EDTA-REGULATED BIOACTIVE HYDROXYAPATITE

by

DANIEL JOSEPH HADERS II

A Dissertation submitted to the

Graduate School-New Brunswick

Rutgers, The State University of New Jersey

in partial fulfillment of the requirements

for the degree of

Doctor of Philosophy

Interdisciplinary Graduate Program in Materials Science and Engineering

and Biomedical Engineering

written under the direction of

Professor Richard E. Riman

and approved by

_____

_____

_____

_____

New Brunswick, New Jersey

May, 2008

ABSTRACT OF THE DISSERTATION

SYNTHESIS AND CHARACTERIZATION OF TEP-EDTA-REGULATED BIOACTIVE HYDROXYAPATITE

By DANIEL JOSEPH HADERS II

Dissertation Director:

Professor Richard E. Riman

Hydroxyapatite (HA), $Ca_{10}(PO_4)_6(OH)_2$, the stoichiometric equivalent of the ceramic phase of bone, is the preferred material for hard tissue replacement due to its bioactivity. However, bioinert metals are utilized in load-bearing orthopedic applications due to the poor mechanical properties of HA. Consequently, attention has been given to HA coatings for metallic orthopedic implants to take advantage of the bioactivity of HA and the mechanical properties of metals. Commercially, the plasma spray process (PS-HA) is the method most often used to deposit HA films on metallic implants. Since its introduction in the 1980's, however, concerns have been raised about the consequences of PS-HA's low crystallinity, lack of phase purity, lack of film-substrate chemical adhesion, passivation properties, and difficulty in coating complex geometries. Thus, there is a need to develop inexpensive reproducible next-generation HA film deposition

techniques, which deposit high crystallinity, phase pure, adhesive, passivating, conformal HA films on clinical metallic substrates.

The aim of this dissertation was to intelligently synthesize and characterize the material and biological properties of HA films on metallic substrates synthesized by hydrothermal crystallization, using thermodynamic phase diagrams as the starting point. In three overlapping interdisciplinary studies the potential of using ethylenediamine-tetraacetic acid/triethyl phosphate (EDTA/TEP) doubly regulated hydrothermal crystallization to deposit HA films, the TEP-regulated, time-and-temperature-dependent process by which films were deposited, and the bioactivity of crystallographically engineered films were investigated. Films were crystallized in a 0.232 molal $Ca(NO_3)_2$-0.232 molal EDTA-0.187 molal TEP-1.852 molal KOH-H_2O chemical system at 200 °C. Thermodynamic phase diagrams demonstrated that the chosen conditions were expected to produce Ca-P phase pure HA, which was experimentally confirmed. EDTA regulation of Ca^{2+} concentration enabled the HA crystallization process to be growth dominated, producing films composed of high crystallinity, hexagonal grains on multiple metallic substrates. TEP regulation of HA crystallization enabled the deposition of an adhesive $CaTiO_3$ intermediate layer, and then HA in a continuous, phase sequenced process on Ti6Al4V substrates, the first such process reported in the hydrothermal HA literature. The HA film was found to be deposited by a passivating competitive growth mechanism that enabled the [0001] crystallographic orientation of hexagonal single crystals to be engineered with synthesis time. Bioactivity analysis demonstrated that films were bioactive and bone

bonding. Together, these results suggest that these HA films are candidates for use on metallic orthopedic implants, namely Ti6Al4V.

PREFACE

This dissertation is based on research conducted primarily in the Department of Materials Science and Engineering, the Department of Biomedical Engineering, and the Department of Cell Biology and Neuroscience at Rutgers, The State University of New Jersey, USA. Research was also conducted in the Department of Materials at the University of Oxford, England, United Kingdom.

The dissertation is based on the following manuscripts, which compose the main body of the dissertation:

1. Haders D.J., Burukhin A, Zlotnikov E, Riman R. E. TEP/EDTA Doubly Regulated Hydrothermal Crystallization of Hydroxyapatite Films on Metal Substrates. Submitted to Chemistry of Materials.
2. Haders D.J., Burukhin A, Huang Y, Cockayne D.J.H., Riman R. E. Phase Sequenced Deposition of Calcium Titanate/Hydroxyapatite Films with Controllable Crystallographic Texture onto Ti6Al4V by TEP Regulated Hydrothermal Crystallization. Submission to Crystal Growth and Design April 2008.
3. Haders D.J., Kazanecki C.C., Burukhin A, Denhardt D.T., Riman R.E. Crystallographically Engineered, Hydrothermally Crystallized Hydroxyapatite Films – an *In vitro* Study of Bioactivity. Submission to Biomaterials April 2008.

DEDICATION

In loving memory of my Grandparents. I wish you were here to share in this moment. I would also like to dedicate this dissertation to my future children; I build this life for you.

ACKNOWLEDGEMENTS

I am grateful to many people who have been part of my life and who have made this dissertation possible. Many of those individuals are listed below, however, many more have played a role in my development as a person and a scientist.

I would like to thank my advisor Professor Richard Riman for his guidance and support throughout my Ph.D. studies. I am grateful for his patience and willingness to support my aspirations of obtaining an interdisciplinary degree and studying abroad, knowing the extra time and work that would be required of him. I am also thankful for his unwillingness to accept mediocrity or work that was simply good enough. This dissertation is the result of his insistence on exceptional scholarship from all his mentees and his consistent belief in my ability.

I would like to thank my dissertation committee, Professor David Denhardt, Professor Adrian Mann, and Professor Prabhas Moghe, for their valuable suggestions and frank comments. The committee's high standards and their commitment to both fundamental understanding and interdisciplinarity were instrumental to the development of this dissertation project. I would especially like to thank my secondary advisor Professor Denhardt. Without his teaching and mentorship in cell biology, the biological studies in this dissertation would not have been possible.

I would like to thank my foreign research advisor Professor David Cockayne of the University of Oxford and his research group including Dr. Yizhong Huang and Katherine

Hartwell. Professor Cockayne's willingness to accept me into his research group and home, provide access to world-class facilities and people, and mentor enabled a unique experience that benefited both this dissertation and my personal life.

I would like to thank the Rutgers University National Science Foundation IGERT on Biointerfaces fellowship program for support and interdisciplinary training. Specifically, I would like to thank the program's primary investigator Professor Prabhas Moghe, program coordinator Dr. Linda Anthony, and my fellow trainees. The training, professional development, and scholarly environment created by the establishment of this program helped to enable the success of this interdisciplinary dissertation and my study abroad experience. I would also like to thank the Center for Ceramic Research, the Rutgers University Department of Education GAANN Fellowship Program in Molecular, Cellular, and Nanosystems Bioengineering, the Rutgers University Laurence M. and Dorothy L. Leeds Scholarship program, the Rutgers University Special Study Opportunity Grant program, the Rutgers University Graduate School New Brunswick Fellowship program, the Rutgers University Conference Travel Award program, and the Rutgers University Roger G. Ackerman Fellowship program for their support of my Ph.D. studies.

I would like to thank my friend and fellow graduate student Dr. Chris Kazanecki. Chris's willingness to collaborate and excitement in doing so were instrumental in executing the biological studies in this dissertation. The conversation, encouragement, and friendship he provided as a colleague and friend, however, were invaluable to the completion of the

dissertation as a whole. I would also like to thank friends and fellow-graduate students Ronald Perez and Ania Knapinska for their support and encouragement.

I would like to thank the present and former members of the Riman research group including but not limited to Phyllis Cassell, Janet Pescinski, Ana Sever, Jennifer Czerepinski, Dr. Vahit Atakan, Dr. Eugene Zlotnikov, and Dr. German Popov. Your advice, help, scholarship, and friendship enabled the success of this dissertation. I am especially grateful to Dr. Alexander Burukhin whose work as a post-doctoral scientist in Professor Riman's group seeded this dissertation.

I would like to thank the professors, teachers, coaches, mentors, and the institutions they represent for the support, encouragement, and opportunity they provided, which equipped me with the tools necessary to succeed in this and future endeavors including Professor Troy Shinbrot (Rutgers University), Professor Clark Hung (Columbia University), Dr. Tom Shaw (I.B.M.), Professor John Hunt (Columbia University), Dr. Fran Ligler (N.R.L.), Dr. Sowmya Ganapathi-Desai (E.P.A), Linda Pennington (Scott High School), Jerry Mohr (Scott High School Track, Cross-Country, and Swimming), and Susan Litton (Taylor Mill Elementary). All of those mentioned and many that are unnamed went above and beyond what was required of them to take an interest in my life and personal development that provided me with a foundation upon which I was able to grow as a person and as a scientist. In the same way, I would also like to thank Columbia University. Columbia and its need-blind financial aid program gave a young man with promise, but limited resources the opportunity of a lifetime.

I would like to thank Dave Parker, Scott Kreimborg, Eric Borg, Mike Reinersman, Chris Lenhof, and Matt Bryant who I have been able to call friends for 12 - 22 years each. It is rare that a man is able to have so many loyal friends and enduring friendships, which span from childhood to adulthood. The laughs and times we have shared have provided me with a well-rounded, well-lived life that has allowed me to endure the rigors of the Ph.D. process. I would especially like to thank Dave Parker for his consistent and steady friendship over the last 22 years. I would also like to thank Rich Serton whose friendship, although more recent, I appreciate no less.

I would like to thank my family who created the foundation upon which I now stand. My Mother and my Father provided me with everything as a child, including the love, support, and experiences, which have made this dissertation and my adult life possible. They sacrificed much to enable me to get to where I am today, and I will be eternally grateful to them for that. My siblings, Muffey, Scott, and Salley, have helped teach me what family is about. My Grandparents helped build my sense of self through nurturing, teaching, encouraging, and admittedly spoiling me. I would also like to thank my aunts, uncles, and cousins who have provided me with great family experiences and memories, and my Mother- and Father-In Laws who long ago welcomed me into their family.

Finally, I would like to thank my Wife. It is rare that a man finds a woman who so perfectly matches him in every way. She is the most brilliant, elegant woman I know. Her friendship, love, and companionship over the last ten years are the rock upon which I

have built my adult life. The experiences and conversations we have shared have provided me with a well-lived life. Her commitment to her own profession, medicine, and her unequivocal confidence in my potential inspired me to push on even in the bleakest days of the Ph.D. process. This dissertation is as much hers as it is mine.

TABLE of CONTENTS

LIST of TABLES

LIST of FIGURES

Chapter 1

INTRODUCTION

The ceramic phase of bone is a poorly crystalline, anion/cation-substituted, non-stoichiometric hydroxyapatite (HA), $Ca_{10}(PO_4)_6(OH)_2$ [1,2]. Due to its biocompatibility, HA is considered the preferred material for hard tissue replacement [2,3]. However, the poor mechanical properties and low reliability of HA necessitates the use of bioinert metals, which often become encapsulated by fibrous tissue *in vivo*, in load-bearing orthopedic applications [2-6]. Consequently, attention has been given to HA coatings for metallic orthopedic implants in an effort to take advantage of the bioactivity of HA and the mechanical properties of clinically used metals [2,3]. Numerous reviews have described how HA-coated metallic orthopedic implants bridge larger gaps between the implant and bone with new bone tissue, accelerate bone apposition, are more tolerant of osteoporotic bone, and have increased bone-implant bond strength as compared with alternative orthopedic implant surfaces including sintered metallic porous coatings, plasma-sprayed titanium coatings, and roughened or untreated metallic implant surfaces [2,5,7-12].

Commercially, most hydroxyapatite coatings are applied using plasma spray methods (PS-HA) [2,9,11-14]. Conceptually simple, the process has many variables, which result in coatings of inconsistent quality with variable crystallinity and variable percentages of secondary and amorphous phases [2,12-17]. Since the introduction of PS-HA coatings in the 1980's [2], numerous studies have raised concern about the consequences of PS-HA's high resorption rates [2,4,15,18], which are reported to reduce bone apposition; lack of film-substrate chemical bonding [2,14,16,17,19], which have resulted in coating delamination *in vivo*

[2,6,10,20,21]; inability to passivate metal substrates [22], which permits the release of toxic metal ions into the body [23,24], and line-of-sight limitations, which result in an inability to coat the internal surfaces of porous or curved three-dimensional structures [12]. In addition, plasma sprayed HA films fail to take advantage of hexagonal HA crystallography to functionalize the film surface with the $\{10\bar{1}0\}$ crystallographic face and actively engineer protein adhesion. Molecular modeling and *in vitro* studies have shown that acidic bone proteins and other proteins found to bind HA with high affinity, bind to the $\{10\bar{1}0\}$ face of HA, which is prominently displayed on the six equivalent faces of hexagonal crystals of HA [25-27]. Therefore, there is a need to develop inexpensive reproducible crystallization processes, which deposit high crystallinity, phase pure, non-resorbing, adhesive, passivating, conformal, hexagonal grained HA films on metallic substrates.

The literature reports numerous additional HA film synthesis techniques including sol-gel, pulsed laser deposition, magnetron sputtering, ion-beam deposition, biomimetic, and hydrothermal crystallization [3]. Sol-gel, magnetron sputtering, pulsed laser deposition, and ion-beam deposition require post-deposition high-temperature heat-treatment to increase crystallinity, density, and often phase purity, and the latter three are line-of-sight limited processes [28-31]. Biomimetic deposition requires multi-day syntheses to produce low crystallinity films [32]. However, non-line-of-sight, solution mediated hydrothermal crystallization has many of the qualities necessary to obtain the films outlined in the previous paragraph. Numerous authors have shown that by regulating processing variables, it is possible to dictate the direct crystallization of desired phases from

homogeneous solutions using this technique [33,34]. Specifically, a number of authors have reported hydrothermal crystallization processes that synthesize phase pure, crystalline, HA films [35-40]. Substrates including titanium, alumina, calcium titanate, monetite, doped tetragonal zirconia, iron, aluminum, and copper have been coated with HA using these methods [35-41].

The literature, however, highlights drawbacks of current HA hydrothermal processes. Authors using multiple substrates have reported substrate-dependent and roughness-dependent effects on precipitation behavior, and films formed on titanium, calcium titanate, aluminum, copper, doped tetragonal zirconia, and alumina are a combination of non-uniform, low density, and non-passivating [35,38-41]. In one study, cross-sections of films formed on alumina are uniform and appear dense and passivating, however, these claims are not specifically made and the authors do not report additional studies on multiple substrates [42]. Grain morphology on iron, aluminum, copper, titanium, calcium titanate, doped tetragonal zirconia, and alumina substrates is limited to plate-, needle-, or rod-like, with diameters less than 5 μm and often near 1 μm, however [38-41]. Two-step processes that use one reaction solution to deposit $CaTiO_3$ and another to deposit HA are required to form both an interfacial layer, which improves film-substrate adhesion, and HA on the clinically relevant Ti6Al4V alloy (alloyed titanium with 6 wt.% aluminum and 4 wt.% vanadium) [35,39,41]. Therefore, there is a need to develop hydrothermal HA crystallization processes that deposit uniform, dense, passivating, hexagonal grained HA films on multiple substrates, in addition to a $CaTiO_3$ interfacial layer on titanium substrates, in a single, phase-sequenced process.

Limitations in the current hydrothermal HA crystallization literature may be overcome by doubly regulating the concentration of Ca^{2+} and PO_4^{3-} ions in the homogeneous reaction solution. Ethylenediamine-tetraacetic acid ($EDTA^{4-}$) is often used to chelate calcium ions to regulate the concentration of uncomplexed Ca^{2+} and control HA nucleation and growth on substrates [36-41]. It has been reported, however, that temperature and pH affect the dissociation of the $Ca(EDTA)^{2-}$ complex [36,38,40]. Therefore, by controlling temperature and pH, uncomplexed Ca^{2+} concentration may be further regulated, enabling the engineering of growth dominated film crystallization processes that result in films that have a characteristic shape, hexagonal for HA, and high crystallinity [43]. Results from the literature have also demonstrate that HA grain aspect ratio may be controlled by regulating Ca^{2+} concentration together with EDTA/Ca ratio, temperature, and pH [44,45]. There are no reports of HA hydrothermal methods that control film nucleation and growth by regulating the concentration of free PO_4^{3-}. One potential route would be to use triethyl phosphate (TEP), which requires completion of a three-step hydrolysis reaction to release PO_4^{3-} ions:

(1) $(C_2H_5O)_3PO + H_2O \rightarrow [(C_2H_5O)_2P(O)_2]^- + C_2H_5OH + H^+$

(2) $[(C_2H_5O)_2P(O)_2]^- + H_2O \rightarrow [(C_2H_5O)P(O)_3]^{2-} + C_2H_5OH + H^+$

(3) $[(C_2H_5O)P(O)_3]^{2-} + H_2O \rightarrow \mathbf{PO_4^{3-}} + C_2H_5OH + H^+$

Research describing the hydrolysis of TEP and related tri-alkyl phosphates has been reported in the literature [46-48]. At or below 110 °C the first ethoxide group hydrolyzes rapidly in a base- or neutral- catalyzed reaction relative to the second and third ethoxide groups, which hydrolyze in an acid-catalyzed reaction [47]. Kinetics studies of the

hydrolysis of the first group at 110 °C show that the reaction rate increases with pH [46]. At higher temperatures (115 – 125 °C) and higher pH (0.8 – 1.4 mole/L KOH) base-catalyzed hydrolysis of di-ethyl phosphate (DEP) is reported [48]. By delaying the release of uncomplexed phosphate ions, reactions involving calcium ions and the substrate may be initiated to form substrate-HA intermediate layers that would enable substrate-HA chemical binding. One possibility would be reacting Ca^{2+} with titanium substrates to form $CaTiO_3$. These Ca^{2+} containing substrate-HA intermediate layers could then be utilized to nucleate and grow HA in a manner that leads to the formation of a continuous uniform film [49,50]. Therefore, through control of temperature and pH and use of TEP and EDTA reagents there exists the potential to doubly regulate the concentration of uncomplexed Ca^{2+} and PO_4^{3-} ions, and consequently, the size, morphology, crystallinity, adhesion, and passivation of HA films.

To intelligently engineer the crystallization process, thermodynamic calculations and models may be utilized to identify the equilibrium phase space (i.e. temperature, pH, reagent concentration combinations) required to produce HA from fundamental principles [34,40,51]. This approach reduces or eliminates time consuming trial and error laboratory methods [34,51]. Riman et al. has previously validated the process of defining HA processing variable space using thermodynamic software, and then synthesizing HA particles based on those diagrams [51].

The aim of this dissertation is to intelligently synthesize and characterize the material and biological properties of HA films on metallic substrates synthesized by hydrothermal

crystallization, using thermodynamic phase diagrams as the starting point. In three overlapping interdisciplinary studies the potential of using EDTA/TEP doubly regulated hydrothermal crystallization to deposit HA films, the TEP-regulated, time-and-temperature-dependent process by which films were deposited, and the bioactivity of crystallographically tunable films were investigated. From the results of these studies a conclusion is reached on the potential of these films to serve as coatings on clinical, load-bearing, metallic, orthopedic substrates.

Chapter 2

TEP/EDTA Doubly-Regulated Hydrothermal Crystallization of Hydroxyapatite Films on Metal Substrates

Daniel J. Haders[1,2], Alexander Burukhin[1], Eugene Zlotnikov[1], Richard E. Riman[1,2]

[1] Department of Material Science and Engineering, Rutgers, The State University of New Jersey, 607 Taylor Road, Piscataway, NJ 08854

[2] Department of Biomedical Engineering, Rutgers, The State University of New Jersey, 599 Taylor Road, Piscataway, NJ 08854

Abstract

The aim of this study was to investigate the use of $Ca(EDTA)^{2-}$ and tri-ethyl phosphate (TEP) to regulate the hydrothermal crystallization of hydroxyapatite (HA) films. HA was coated on various substrates including titanium, Ti6Al4V, grit-blasted Ti6Al4V, 316 stainless steel, and Co28Cr6Mo via hydrothermal synthesis at 200 °C for 24 h utilizing a 0.232 molal $Ca(NO_3)_2$ -0.232 molal EDTA-0.187 molal TEP-1.852 molal KOH-H_2O chemical system. The role of film deposition processing variables on HA crystallization was studied using thermodynamic process simulation and experimental TEP hydrolysis kinetics data. Profilometry, XRD, FESEM, and adhesion testing (ASTM D3359) were used to characterize substrates and films. Kinetics studies of TEP hydrolysis revealed that phosphate was available for the formation of HA at temperatures above 180 °C and synthesis times greater than 4 h. Thermodynamic modeling demonstrated both that the formation of phase pure HA was thermodynamically favored at 200 °C on all substrates and that the equilibrium concentration of free Ca^{2+} was lower in this system than in

hydrothermal HA film crystallization systems reported elsewhere. Materials characterization results indicate that high crystallinity (99+ %), (0002) crystallographically oriented, passivating, Ca-P (calcium-phosphate) phase pure HA films composed of hexagonal faceted grains (8-12 μm diameter) were formed on all substrates. Based on these results, it is concluded that the use of TEP necessitates a continuous two-step film deposition process that deposits phase pure HA at temperatures above 180 °C. The use of $Ca(EDTA)^{2-}$/pH regulation of Ca^{2+} concentration enables the hydrothermal HA crystallization process to be growth dominated, producing films composed of high crystallinity, hexagonal grains.

Introduction

The ceramic phase of bone is a poorly crystalline, anion/cation-substituted, non-stoichiometric hydroxyapatite (HA), $Ca_{10}(PO_4)_6(OH)_2$ [1,2,52]. Due to its biocompatibility, HA is considered the preferred material for hard tissue replacement [2,3]. However, the poor mechanical properties and low reliability of HA necessitates the use of bioinert metals, which often become encapsulated by fibrous tissue *in vivo*, in load-bearing orthopedic applications [2-6]. Consequently, attention has been given to HA coatings for metallic orthopedic implants in an effort to take advantage of the bioactivity of HA and the mechanical properties of clinically used metals [2,3]. Numerous reviews have described how HA-coated metallic orthopedic implants bridge larger gaps between the implant and bone with new bone tissue, accelerate bone apposition, are more tolerant of osteoporotic bone, and have increased bone-implant bond strength as compared with alternative

orthopedic implant surfaces including sintered metallic porous coatings, plasma-sprayed titanium coatings, and roughened or untreated metallic implant surfaces [2,5,7-12].

Commercially, most hydroxyapatite coatings are applied using plasma spray methods (PS-HA) [2,9,11-14]. Conceptually simple, the process has many variables, which result in coatings of inconsistent quality with variable crystallinity and variable percentages of secondary and amorphous phases [2,12-17]. Since the introduction of PS-HA coatings in the 1980's [2], numerous studies have raised concern about the consequences of PS-HA's high resorption rates [2,4,15,18], which are reported to reduce bone apposition; poor adhesion properties [2,14,16,17,19], which have resulted in coating delamination *in vivo* [2,6,10,20,21]; inability to passivate metal substrates [22], which permits the release of toxic metal ions into the body [23,24], and line-of-sight limitations, which result in an inability to coat the internal surfaces of porous or curved three-dimensional structures [12]. Therefore, there is a need to develop inexpensive reproducible crystallization processes, which deposit high crystallinity, phase pure, non-resorbing, adhesive, passivating, conformal HA films on metallic substrates.

The literature reports numerous additional HA film synthesis techniques including sol-gel, pulsed laser deposition, magnetron sputtering, ion-beam deposition, biomimetic, and hydrothermal crystallization [3]. Sol-gel, magnetron sputtering, pulsed laser deposition, and ion-beam deposition require post-deposition high-temperature heat-treatment to increase crystallinity, density, and often phase purity, and the latter three are line of sight limited processes [28-31]. Biomimetic deposition requires multi-day syntheses to produce low

crystallinity films [32]. However, non-line-of-sight, solution mediated hydrothermal crystallization has many of the qualities necessary to obtain the films outlined in the previous paragraph. Numerous authors have shown that by regulating processing variables, it is possible to dictate the direct crystallization of desired phases from homogeneous solutions using this technique [33,34]. Specifically, a number of authors have reported hydrothermal crystallization processes that synthesize phase pure, crystalline, HA films [35-40]. Substrates including titanium, alumina, calcium titanate, monetite, doped tetragonal zirconia, iron, aluminum, and copper have been coated with HA using these methods [35-41].

The literature, however, highlights drawbacks of current HA hydrothermal processes. Authors using multiple substrates have reported substrate-dependent and roughness-dependent effects on precipitation behavior, and films formed on titanium, calcium titanate, aluminum, copper, doped tetragonal zirconia, and alumina are a combination of non-uniform, low density, and non-passivating [35,38-41]. In one study, cross-sections of films formed on alumina are uniform and appear dense and passivating, however, these claims are not specifically made and the authors do not report additional studies on multiple substrates [42]. Hexagonal grains of HA are known to display the $\{10\bar{1}0\}$ crystallographic plain, which has been shown to bind bone proteins and bone protein amino acid sequences with high affinity [25-27]. Grain morphology on iron, aluminum, copper, titanium, calcium titanate, doped tetragonal zirconia, and alumina substrates is limited to plate-, needle-, or rod-like, with diameters less than 5 μm and often near 1 μm, however [38-41]. Two-step processes that use one reaction solution to deposit $CaTiO_3$ and

another to deposit HA are required to form both an interfacial layer, which improves film-substrate adhesion, and HA on the clinically relevant Ti6Al4V alloy (alloyed titanium with 6 wt.% aluminum and 4 wt.% vanadium) [35,39,41]. Therefore, there is a need to develop hydrothermal HA crystallization processes that deposit uniform, dense, passivating, hexagonal grained HA films on multiple substrates, in addition to a $CaTiO_3$ interfacial layer on titanium substrates, in a single continuous process.

Limitations in the current hydrothermal HA crystallization literature may be overcome by doubly regulating the concentration of Ca^{2+} and PO_4^{3-} ions in the homogeneous reaction solution. Ethylenediamine-tetraacetic acid ($EDTA^{4-}$) is often used to chelate calcium ions to regulate the concentration of uncomplexed Ca^{2+} and control HA nucleation and growth on substrates [36-41]. It has been reported, however, that temperature and pH affect the dissociation of the $Ca(EDTA)^{2-}$ complex [36,38,40]. Therefore, by controlling temperature and pH, uncomplexed Ca^{2+} concentration may be further regulated, enabling the engineering of growth-dominated film crystallization processes that result in films that have a characteristic shape, hexagonal for HA, and high crystallinity [43]. Results from the literature have also demonstrate that HA grain aspect ratio may be controlled by regulating Ca^{2+} concentration together with EDTA/Ca ratio, temperature, and pH [44,45]. There are no reports of HA hydrothermal methods that control film nucleation and growth by regulating the concentration of free PO_4^{3-}. One potential route would be to use triethyl phosphate (TEP), which requires completion of a three-step hydrolysis reaction to release PO_4^{3-} ions:

(5) $(C_2H_5O)_3PO + H_2O \rightarrow [(C_2H_5O)_2P(O)_2]^- + C_2H_5OH + H^+$

(6) $[(C_2H_5O)_2P(O)_2]^- + H_2O \rightarrow [(C_2H_5O)P(O)_3]^{2-} + C_2H_5OH + H^+$

(7) $[(C_2H_5O)P(O)_3]^{2-} + H_2O \rightarrow \mathbf{PO_4^{3-}} + C_2H_5OH + H^+$

Research describing the hydrolysis of TEP and related tri-alkyl phosphates has been reported in the literature [46-48]. At or below 110 °C the first ethoxide group hydrolyzes rapidly in a base- or neutral- catalyzed reaction relative to the second and third ethoxide groups, which hydrolyze in an acid-catalyzed reaction [47]. Kinetics studies of the hydrolysis of the first group at 110 °C show that the reaction rate increases with pH [46]. At higher temperatures (115 – 125 °C) and higher pH (0.8 – 1.4 mole/L KOH) base-catalyzed hydrolysis of di-ethyl phosphate (DEP) is reported [48]. By delaying the release of uncomplexed phosphate ions, reactions involving calcium ions and the substrate may be initiated to form substrate-HA intermediate layers. One possibility would be reacting Ca^{2+} with titanium substrates to form $CaTiO_3$. Therefore, through control of temperature and pH and use of TEP and EDTA reagents there exists the potential to doubly regulate the concentration of uncomplexed Ca^{2+} and PO_4^{3-} ions, and consequently, the size, morphology, crystallinity, and adhesion of HA films.

To intelligently engineer the crystallization process, thermodynamic calculations and models may be utilized to identify the equilibrium phase space (i.e. temperature, pH, reagent concentration combinations) required to produce HA from fundamental principles [34,40,51]. This approach reduces or eliminates time consuming trial and error laboratory methods [34,51]. Riman et al. has previously validated the process of defining HA processing variable space using thermodynamic software, and then synthesizing HA particles based on those diagrams [51].

This study reports the first use of EDTA/TEP doubly-regulated hydrothermal crystallization of hydroxyapatite films on multiple substrates. The study explores the kinetics of TEP hydrolysis and the thermodynamics of free calcium concentration and HA phase equilibria, as well as the effect of substrate on the microstructure, thickness, constituent phases, crystallinity, and adhesion of HA films.

Experimental Section

a. Thermodynamic Process Simulation

Thermodynamic phase equilibria models were calculated using thermo-chemical simulation software (OLI Systems, Inc., Morris Plains, NJ). The fundamental basis for the algorithms used in the software is reported in Lencka and Riman [53]. HA thermodynamic phase equilibria models for the $CaO - P_2O_5 - NH_4NO_3 - H_2O$ chemical system are reported in Riman et al. [51].

Experimental conditions for hydrothermal crystallization of HA films in the $Ca(NO_3)_2$ – EDTA - TEP – KOH - H_2O chemical system were chosen based upon calculated phase boundaries of the $Ca(NO_3)_2$ – EDTA - H_3PO_4 – KOH - H_2O system in the presence of titanium, 316 stainless steel (Fe-Cr-Ni), and Co-Cr at 200 °C. These metals were considered representative of the substrates used in this work (Ti6Al4V, grit blasted Ti6Al4V, Ti, 316 stainless steel, Co28Cr6Mo, see below), which were chosen based on their current or prior use in clinical load bearing orthopedic applications. The software database does not contain TEP because there is no reported thermodynamic data for TEP

in the literature. Thus, H_3PO_4 was utilized in its place for thermodynamic calculations. The use of this acid allows the model to account for products of TEP hydrolysis, PO_4^{3-} and $3H^+$, without the explicit use of TEP. TEP kinetics results, reported below, indicate that complete hydrolysis occurs at 180 °C, which validates the substitution of H_3PO_4 for TEP in the model at 200°C. The third product of TEP hydrolysis, C_2H_5OH, was ignored due to its dilute state in the solution, 0.561 molal after full TEP hydrolysis. This omission was justified by comparing the phase diagrams of the 0.232 molal $Ca(NO_3)$-0.232 molal EDTA-0.187 molal H_3PO_4-1.852 molal KOH-Ti-H_2O chemical system and the 0.232 molal $Ca(NO_3)$-0.232 molal EDTA-0.187 molal H_3PO_4-0.561 molal C_2H_5OH-1.852 molal KOH-Ti-H_2O chemical system at 200 °C. A comparison of the two diagrams demonstrated no differences in the position of phase boundaries at pH relevant to the work in this study. After the creation of phase diagrams the specific pH/Ca^{2+} combination for the 0.232 molal $Ca(NO_3)_2$-0.232 molal EDTA-0.187 molal H_3PO_4-1.852 molal KOH - H_2O chemical system used for synthesis in this paper, see below, in the presence of each substrate at 200 °C was calculated and plotted on each respective diagram.

b. TEP Hydrolysis Kinetics and Reactor Heating Dynamics

To characterize the release of phosphate ions from TEP, model mixtures containing KOH (Fisher Scientific Hampton, NH) and TEP (Sigma Aldrich, St. Louis, MO) were prepared. KOH and TEP were dissolved in de-ionized water at the same concentrations used for synthesis, see below, and loaded into a 1 L stirred Teflon®-lined autoclave (Model 4531, Parr Instruments, Moline, IL). The autoclave was equipped with a needle valve with dip tube that allowed sampling at elevated pressure and temperature. Excess calcium nitrate tetrahydrate (Fisher Scientific) was added to samples of reaction products

of TEP hydrolysis taken from the reactor at various temperatures to monitor free phosphate formation. The solution was filtered and assayed for the presence of Ca-P precipitate. To evaluate the heating rate of the reaction solution autoclave heating dynamics were investigated by directly placing K-type thermocouples into 125 mL Parr 4731 autoclaves filled with a model non-volatile liquid, technical grade glycerol. Autoclaves were placed in an oven pre-heated to 200 °C and internal changes in temperature were monitored with time. Heating dynamics were compared to TEP hydrolysis kinetics to determine the reaction time above which uncomplexed PO_4^{3-} was available for formation of HA.

c. Equilibrium Ca^{2+} concentration

Equilibrium Ca^{2+} concentrations were calculated using commercial thermo-chemical simulation software referred to previously (OLI Systems, Inc.). The equilibrium concentration of Ca^{2+} was calculated for temperatures from 25 – 180 °C in the 0.232 molal $Ca(NO_3)_2$-0.232 molal EDTA-1.852 molal KOH-H_2O system in the presence of Ti. This model predicts the concentration of Ca^{2+} prior to complete TEP hydrolysis (see below). Due to the absence of TEP in the software database (see above) the results from the model do not take into account the products of partial TEP hydrolysis, $2H^+$ and $2C_2H_5OH$. For comparison, the concentration of Ca^{2+} was calculated for temperatures from 25 – 160 °C (initial HA deposition temperature) in the 0.05 molal $Ca(EDTA)^{2-}$-0.05 molal NaH_2PO_4–NaOH–H_2O-Ti hydrothermal synthesis system, demonstrated by Fujishiro et al. to form phase pure HA [40]. Equilibrium Ca^{2+} concentrations at the initial HA deposition temperature of the system presented here, 180 °C (see below), and the system reported by Fujishiro et al., 160 °C, were compared to evaluate the

thermodynamic effect of pH and temperature on uncomplexed Ca^{2+} concentration and to predict/explain morphological differences between the two films.

d. Film Synthesis

Metal substrates (Ti6Al4V, grit blasted Ti6Al4V, Ti, 316 stainless steel, Co28Cr6Mo) were chosen based on their current or prior use in clinical load bearing orthopedic applications. The choice of substrates enabled an investigation of the ability of the crystallization process to uniformly coat substrates with various chemistries and surface roughnesses with HA. The choice of substrates also enabled an investigation of the effect of crystallography on HA deposition - Ti6Al4V, grit blasted Ti6Al4V, Ti, and Co28Cr6Mo have hexagonal crystal lattices and 316 stainless steel has a cubic lattice.

Prior to synthesis, 1 in diameter rods of Ti6Al4V alloy (ASTM-B348 Grade 5, McMaster Carr, Dayton, NJ), titanium (98.9 % pure, ASTM-B348 Grade 2, McMaster Carr), 316 stainless steel (ASTM-A276, McMaster Carr), and Co28Cr6Mo alloy (ASTM-F75, Stryker Orthopaedics, Mahwah, NJ) were cut into discs, 1 in (diameter) x 1/8 in (thickness), and used as substrates. Where indicated, Ti6Al4V alloy substrates were grit blasted using 35-100 Al_2O_3 media (McMaster Carr) to roughen the surface. Grit was removed by cleaning in an ultrasonic bath (FS30, Fisher Scientific). All substrates, titanium foil (0.127mm, 99.7%, Sigma-Aldrich) substrate holders, and Teflon® reaction vessel liners (125 mL, Parr Instrument) were cleaned with Citronox detergent (Alconox, White Plains, NY), acetone (Fisher Scientific), ethyl alcohol (Pharmco-AAPER, Brookfield, CT), and deionized water and dried in a 60 °C oven prior to synthesis.

Aqueous stock solutions of 0.232 molal calcium nitrate tetrahydrate, $Ca(NO_3)_2*4H_2O$ (99.38 %, Fisher Scientific), 0.232 molal ethylenediamine-tetraacetic acid (EDTA), $C_{10}H_{16}N_2O_8$ (99.4 %, Fisher Scientific), 0.187 molal triethyl phosphate (TEP), $C_6H_{15}O_4P$ (99.8+ %, Sigma Aldrich), and 1.852 molal potassium hydroxide, KOH (89.3 %, Fisher Scientific) were used for hydrothermal reactions and prepared as follows:
Calcium nitrate tetrahydrate, EDTA, and TEP were mixed together and dissolved in deionized H_2O. In a second container KOH was dissolved in deionized H_2O. Once dissolved, the KOH solution was placed in a cold-water bath to cool to room temperature. When cool, the KOH solution was added to the former solution and stirred until visible particulates had dissolved. The stock solution was then filtered (220 nm pore size, Nalgene, Rochester, NY) and stored in a tightly sealed container.

The typical hydrothermal reaction was conducted as follows: The substrate was fixed in the substrate holder and placed inside a 125 ml Teflon®-lined reaction vessel (4731 reactor, Parr Instrument). The substrate holder placed the sample in a position that inhibited the settling of homogeneously formed nuclei onto the surface by means of gravity (Figure 2.1). Stock solution, 70 mL, was added to the reaction vessel, which was then sealed. The reactor was then placed in an oven pre-heated to 200 °C for 24 hours. The reactor was removed from the oven and allowed to cool to room temperature in air. The substrate was removed from the reactor and rinsed for several minutes in running tap water and then in deionized water. The sample was then placed in a 60 °C oven to dry.

e. Substrate and Film Characterization

A profilometer (scan length 500 μm, Dektak 3030, Veeco, Woodbury, NY) was used to measure the surface roughness, Ra, of each substrate. Field emission scanning electron microscopy (FESEM) (DSM 982 Gemini, Carl Zeiss, Oberkochen, Germany) was used to examine the bare substrate and film microstructure in cross-section, top-on, and after adhesion experiments. Cross sectional samples were prepared by cutting two cross-sections from each substrate-film sample with a diamond saw (Vari/Cut VC-50, Leco Corporation, St. Joseph, MI). These were then embedded face-to-face in epoxy (SPI-PON® Epoxy Embedding Kit, SPI Supplies, West Chester, PA), polished until substrates achieved a mirror finish, and sputter coated with a conducting 25nm Au/Pd film (Balzers SCD 004, OC Oerlikon Balzers AG, Balzers, Liechtenstein). Film thickness was computed by direct measurement of the thickness of FESEM cross-sections at 22 μm intervals (10 points) along the length of the micrograph using commercial image analysis software. Grain diameter was determined by direct measurement of 10 randomly selected grains shown in top-on FESEM micrographs using commercial image analysis software. Average film thickness, average grain diameter, and the standard deviation of the means were calculated using Excel (Microsoft, Redmond, WA). A two-tailed, heteroscedastic t-test was used to determine if differences in grain diameters were significant (α=0.5, Microsoft Excel). An estimate of grain aspect ratio was calculated by dividing average film thickness by average grain diameter. The calculation assumes that grains run continuously from the substrate surface to the film surface. X-ray diffraction (XRD) (step size = 0.005 °, 1 step/sec, 45 KV, 40 mA, Ni-filtered CuK_α radiation, parallel beam optics, Philips Hi-Resolution X'PERT X-Ray Diffractometer, PANalytical B.V., Almelo, Netherlands) was used to determine the phases present in the films and the substrate.

XRD patterns from Co28Cr6Mo and 316 stainless steel substrates were obtained using an additional graphite diffracted beam monochromator (PANalytical B.V.) to remove background fluorescence. Experimental XRD patterns were matched to patterns in the Powder Diffraction File (PDF, ICDD, Newtown Square, PA) database using Jade 6.5 software (MDI, Livermore, CA). Subsequent to curve fitting (Jade 6.5, MDI), the crystallinity of hydroxyapatite was calculated by comparing the area of HA crystalline peaks in the range 28-35 ° and of the amorphous calcium-phosphate (ACP) hump centered at approximately 30 - 31 ° (2θ) using the following equation [14]:

$$(4)\quad X\% = \left[\frac{\sum_{i=1}^{c} A_c}{\left(\sum_{i=1}^{c} A_c + \sum_{i=1}^{a} A_a \right)} \right] * 100\%$$

where, ΣA_c is the sum of the areas under all the HA crystalline peaks and ΣA_a is the sum of the area under the ACP hump. Peak intensities were also used to calculate HA (0002)/(21 $\bar{3}$ 1) peak ratios. Peak de-convolution was used to determine (21 $\bar{3}$ 1) peak intensity due to the overlapping peak profiles of the (21 $\bar{3}$ 1) and (11 $\bar{2}$ 2) peaks in the HA profile (Jade 6.5). The adhesion of the film to the substrate was measured using the ASTM (American Society for Testing and Materials, West Conshohocken, Pennsylvania) standard D3359-02 tape test A. Adhesion was rated on a scale of 0-5 with 5 representing no peeling and 0 representing complete removal, as specified by ASTM. Four measurements were averaged and reported for each film. For comparison purposes, Metalastic DTM Acrylic Modified Enamel (Cleveland, OH, Sherwin Williams) with an ASTM D3359 adhesion rating of 5 and Industrial Shop Primer (Gardnerville, NV,

Aervoe Industries Incorporated) with an ASTM D3359 adhesion rating of 3 were used as standards.

Results

a. Thermodynamic Process Simulation

Computed phase stability diagrams for the $Ca(NO_3)_2$–EDTA-H_3PO_4–KOH-H_2O system in the presence of titanium, 316 stainless steel, and Co-Cr substrates at 200 °C are shown in Figures 2.2a-c. The diagrams illustrate a wide stability range for HA under these conditions. The diagrams also illustrate that titanium, 316 stainless steel, and Co-Cr substrates are not thermodynamically stable, leading to the formation of oxides. The specific pH/$[Ca^{2+}]$ point for the 0.232 molal $Ca(NO_3)_2$–0.232 molal EDTA–0.187 molal H_3PO_4–1.852 molal KOH-H_2O system in the presence of each respective substrate is marked. For each substrate the pH/$[Ca^{2+}]$ data point lies in a region where both an oxide and hydroxyapatite are stable. These diagrams demonstrate that the formation of Ca-P (calcium-phosphate) phase pure HA is thermodynamically favored in the presence of all substrates under these reaction conditions, and confirm the stability of HA in alkaline solutions.

b. TEP Kinetics

TEP hydrolysis kinetics were examined under alkaline hydrothermal conditions. Results revealed that Ca-P particles precipitated in samples taken from solutions with temperatures above 180 °C, after the addition of excess calcium nitrate. This agrees with hydrolysis results from the literature, which suggest that temperatures above 110 °C are needed to hydrolyze the second and third ethyl groups in basic solutions [46-48]. The heating

dynamics for the autoclave used in this study were also examined. Heating from room temperature to 180 °C was observed to take 4 h (Figure 2.3). Thus, the use of TEP necessitates a two-step film deposition process. The first step, which occurs between 0-4 hours, encompasses the heating of the reaction mixture from room temperature to 180 °C. During this step incomplete TEP hydrolysis and the absence of free phosphate ions exclude the possibility of HA crystallization. In the second step, after 4 hours, the autoclave is heated from 180 °C to the final isothermal temperature of 200 °C, complete TEP hydrolysis occurs, and free phosphate is available for the formation of HA.

c. Equilibrium Ca^{2+} Concentration

The equilibrium concentration of uncomplexed Ca^{2+} in the 0.232 molal $Ca(NO_3)_2$-1.852 molal KOH-0.232 molal EDTA-Ti reaction mixture used in this study is displayed in Figure 2.4. When phosphate is first available from TEP hydrolysis at 180 °C (see above), the model calculates an uncomplexed Ca^{2+} concentration of $3.02*10^{-8}$ molal at a pH of 10.91. For comparison, the concentration of uncomplexed Ca^{2+} in the 0.05 molal $Ca(EDTA)^{2-}$-0.05 molal NaH_2PO_4–NaOH–H_2O-Ti hydrothermal synthesis system, demonstrated by Fujishiro et al. to form phase pure HA in this system, was modeled [40]. Thermochemical modeling of the system reported by Fujishiro et al. predicts an uncomplexed Ca^{2+} concentration of $3.31*10^{-6}$ molal at their initial HA deposition temperature and pH, 160 °C, pH 6. Results demonstrate that Fujishiro et al.'s system has a two order of magnitude greater concentration of uncomplexed Ca^{2+} than the system reported here, at each system's respective initial HA deposition temperature. The concentration of calcium precursor used in the study reported here, however, is nearly 5-fold greater than the concentration of calcium precursor used by Fujishiro et al. The

explanation for this result is pH. The literature has reported that increasing the pH of a solution decreases the ability of the Ca-EDTA^{2-} complex to dissociate [36,38]. At 180 °C the pH of the solution used in this study is thermodynamically calculated to be 10.91, at 160°C the pH of Fujishiro et al.'s solution is 6. Thus, by using EDTA^{4-}, increasing pH, and having a lower concentration of uncomplexed Ca^{2+} this synthesis process should favor crystal growth over crystal nucleation resulting in films that have a characteristic shape, and high crystallinity [43]. In addition, multiple authors have reported that the length and/or aspect ratio of HA crystals formed in solution by non-stirred homogeneous precipitation using EDTA are a function of Ca^{2+} concentration together with PO_4^{3-} concentration, EDTA/Ca ratio, temperature, and pH, indicating that a variation in grain aspect ratio should be expected from that reported elsewhere [44,45].

d. Substrate Characterization

Figure 2.5 and Figure 2.6 display complementary scanning electron micrographs and X-ray diffraction patterns of Ti6Al4V, Ti, roughened Ti6Al4V, stainless steel, and Co28Cr6Mo substrates prior to hydrothermal treatment. SEM micrographs demonstrate that all non-roughened substrates lack distinct features or topography except for periodic polishing marks. The grit-blasted Ti6Al4V substrate, on the other hand, has an irregular crevassed surface with numerous pits of different sizes and shapes. These differences in surface topography are reflected in the profilometer surface roughness results reported in Table 2.1. Phase analysis of XRD patterns, reported in Table 2.1, confirm the expected identity of each material. Corundum is found in the roughened Ti substrate due to the use of Al_2O_3 media, and its implantation into the substrate during the grit-blasting process. This finding is in agreement with other authors using the same roughening technique [16,19].

Peak ratio texture analysis results are reported in Table 2.1 as well. Through comparison with Powder Diffraction File standards it can be concluded that all substrates display some degree of preferred crystallographic orientation.

e. Film Phase and Crystallinity

Figure 2.6 displays X-ray diffraction patterns of films deposited on Ti6Al4V, Ti, roughened Ti6Al4V, stainless steel, and Co28Cr6Mo substrates after hydrothermal treatment. Phase analysis confirms that HA is the only Ca-P phase formed on each substrate. The films formed on the Ti6Al4V, Ti, and roughened Ti6Al4V also display a small peak at 26.98 ° that is at the same position of the 100 % TiO_2 (110) peak. The analysis software did not identify an ACP hump for any sample (Table 2.2). Therefore, all films were calculated to have crystallinity indexes of 99 %. The lack of an amorphous hump made any affect of preferred orientation, see below, on peak areas and, thus, the crystallinity calculation moot. Nonetheless, a crystallinity index less than 100 % is reported due to the inherent error in the calculation. These results demonstrate that the hydrothermal crystallization process presented here deposits highly crystalline, Ca-P phase pure HA regardless of substrate chemistry, crystallography, or surface roughness (Figure 2.5, Figure 2.6, Table 2.1, Table 2.2). Phase pure, high crystallinity HA is a requirement of next generation HA films due to the lower solubility and higher bone apposition percentages that have been reported for HA coatings with increasing chemical stability [4,15,18,54].

f. Film Morphology and Orientation

Figure 2.7 displays scanning electron micrographs of films deposited on Ti6Al4V, Ti, roughened Ti6Al4V, stainless steel, and Co28Cr6Mo substrates after hydrothermal

treatment. Deposited films are composed of uniform hexagonally faceted grains that appear to have grown perpendicular to the substrate surface on all substrates. The hexagonal prism is one of the idealized forms of crystals in HA's 6/m crystal class [43]. The formation of grains of this type indicates that these films form through a low energy growth controlled process [55]. This HA morphology is important biologically as it known to display crystallographic faces that bind bone proteins and bone protein amino acid sequences with high affinity [25-27].

Average grain diameter and grain diameter uniformity are observed to vary from titanium-based substrates, 12+/-4 μm, to non-titanium substrates, 8+/-5 μm (Figure 2.7, Table 2.2). t-test analysis of results demonstrate, however, that differences are not significant for $\alpha = 0.05$. From this result it may be concluded that substrate chemistry and surface roughness do not play a significant role in grain nucleation and growth. Average grain diameters are larger than elsewhere in the literature, and 3-4 fold larger than those reported by Fujishiro et al., at the synthesis conditions modeled above [38-42]. Assuming that grains are continuous from the substrate surface to the film surface, a rough estimate of grain aspect ratio of 1-2 may be calculated by comparing average grain diameter to average film thickness, reported below, for each substrate. Grain aspect ratios for HA films reported elsewhere in the homogeneous precipitation hydrothermal literature are on the order of 10 [39-41,56]. Thus, it may be concluded that the synthesis conditions reported here compose a novel set that enable the growth of near equiaxed grains of HA.

X-ray diffraction peak ratio texture analysis results report (0002)/(21 $\bar{3}$ 1) HA peak ratios that are larger than what is predicted for randomly oriented grains, 0.28, by the Powder Diffraction File, for films formed on all substrates (Figure 2.6, Table 2.2). From these results it may be concluded that hexagonal grains within all HA films are preferentially oriented with respect to the (0002) crystallographic plane regardless of substrate. Peak ratios vary from 0.66 to greater than 100 (Table 2.2), however, it is not appropriate to draw conclusions from these differences. Peak ratio texture analysis is a qualitative technique used to determine the presence or lack or crystallographic texture in a sample, not the degree of texture [57]. Techniques such as X-ray diffraction pole figures are required to determine the degree of texture. In a follow-up manuscript we will report detailed time elapsed XRD, SEM, and X-ray pole figure analysis of crystallographic orientation evolution on Ti6Al4V substrates as a function of hydrothermal reaction time [58].

Analysis of substrate XRD patterns report that Ti6Al4V, grit blasted Ti6Al4V, Ti, and CoCrMo substrates have (0002) crystallographic orientation and hexagonal crystal lattices (Figure 2.6, Table 2.1). Because HA also has a hexagonal crystal lattice, these results, together with the results of HA film preferred orientation analysis (Figure 2.6, Table 2.1), suggests that (0002) HA crystallographic orientation is due to epitaxy. The film formed on the non-hexagonal non-(002) oriented 316 stainless steel, however, has a (0002)/(21 $\bar{3}$ 1) ratio larger than the value reported in PDF 60-6484. Thus, it may be concluded that the source of grain orientation is not epitaxy, but instead a process such as competitive growth, which also results in preferentially oriented films [59]. This conclusion

agrees with results from the hydrothermal literature that also report larger than predicted (0002)/(21 $\bar{3}$ 1) HA peak ratios for films formed on non-hexagonal iron and alumina after hydrothermal treatment [37,38].

g. Passivation

Scanning electron micrographs are displayed in Figure 2.8 of cross-sections from films deposited on Ti6Al4V, Ti, roughened Ti6Al4V, stainless steel, and Co28Cr6Mo substrates after hydrothermal treatment . All micrographs display an irregular structure with grains emanating from underlying dense, continuous, passivating films. The delamination of the film formed on Co28Cr6Mo could be an artifact of the polishing process or be related to film-substrate adhesion results reported below (Figure 2.8e.). Passive film growth models and results report that the formation of a passivating film occurs through a single process - an initial 2D film is formed followed by 3D growth [60]. Thus, the formation of passivating films on all substrates indicates that the nucleation and growth process is similar on each substrate. Average film thickness values vary from 22+/-8 μm (Ti6Al4V) to 12+/-7 μm (Co28Cr6Mo) (Table 2.2). Due to the limited area sampled by a cross-section and the topology of the samples it is not possible to draw conclusions regarding differences in film thickness from one substrate to another. Nonetheless, the formation of a dense, passivating film is important because it has the potential to inhibit the dissolution of toxic metal ions from substrates into the surrounding tissue [23,24]. The chemical stability of crystalline HA together with the passivation of the substrate surface may make this crystallization process appropriate for anti-corrosion applications as well.

h. Adhesion

Results of adhesion testing are reported in Table 2.2 and Figure 2.9. According to the standardized ASTM- D3359-02 adhesion scale of 0-5, the films deposited on Ti6Al4V, Ti, and roughened Ti6Al4V substrates scored a 5. Further, scanning electron microscopy analysis of the surface of a representative titanium substrate indicates no peeling or film removal outside the line directly cut with a razor blade. At the intersection of the cross cut, the film forms sharp points indicating strong film adhesion. The films deposited on 316 stainless steel substrates scored an average rating of 4. These films demonstrated variability in adhesion, however. Two of four samples received a rating of 4, one sample received a rating of 5, and one sample received a rating of 3. Films deposited on Co28Cr6Mo substrates scored an adhesion rating of 3. Scanning electron micrographs of the surface of a representative Co28Cr6Mo substrate display consistent and jagged film removal on either side of the original cut. Extensive film removal inhibits the formation of sharp points at the intersection of the cross cut. These results demonstrate that adhesion is a function of substrate chemistry, and primarily related to the presence of titanium in a substrate. Next generation HA films require high HA film-substrate adhesion to eliminate *in vivo* coating delamination and its resulting complications, which are known to increase the failure rate of PS-HA coatings [6,10,20,21].

Discussion

The engineering of the crystallization process was facilitated by the use of thermodynamic process simulation. Through the use of process-simulation methods reported by Riman et al., phase stability diagrams were developed at 200 °C that allowed reactant concentration and pH combinations, favorable for HA deposition on multiple

substrates, to be chosen prior to experimental work (Figure 2.2) [34,51]. This eliminated the need to undertake time-consuming trial and error laboratory methodologies.

TEP hydrolysis kinetics studies revealed that under the chosen reaction conditions free phosphate was not available for HA synthesis until 180 °C at 4 hours synthesis time (Figure 2.4). Thus, the use of a delayed release phosphate source provided the opportunity to deposit HA-substrate intermediates prior to TEP hydrolysis, and HA post-hydrolysis in a continuous crystallization process. This is in contrast to processes reported in the literature, which require multiple reaction solutions to form $CaTiO_3$-HA films on titanium substrates that improve film-substrate adhesion [35,39,41]. Results from ASTM - D3359-02 tape test A demonstrated that films formed on titanium-based substrates, regardless of alloying components or surface roughness, possessed superior adhesion properties to films formed on 316 stainless steel and Co28Cr6Mo alloy (Table 2.1, Table 2.2, Figure 2.9). Consequently, the explanation for this result is likely the formation of a substrate-HA chemical intermediate on titanium based substrates, $CaTiO_3$, but not on 316 stainless steel or Co28Cr6Mo prior to HA deposition. Due to the thickness of the HA film and the limited detection capabilities of x-ray diffraction, it is possible that an interfacial phase could go undetected by XRD. The film-Ti6Al4V substrate interface is examined in detail in a follow-up manuscript by Haders et al. [58].

Thermodynamic process simulation facilitated the choice of reaction conditions that both were in the region of HA phase stability and regulated the amount of uncomplexed Ca^{2+}. Thermodynamic process simulation results reported a two-order-of-magnitude lower Ca^{2+}

ion concentration for the hydrothermal system in this study, than the hydrothermal system reported by Fujishiro et al., at their respective HA deposition temperature and pH [40] (Figure 2.3). Based on the results of other hydrothermal HA film crystallization processes, this is a result of the decreased ability of the Ca-EDTA^{2-} complex to dissociate in solutions with increasing pH [36,38]. By lowering Ca^{2+} concentration it was hypothesized that the reaction conditions used here would favor crystal growth over crystal nucleation.

Growth-dominated film crystallization processes typically result in films with grains that have a characteristic shape and high crystallinity [43]. Results reported above show that uniform morphological films composed of phase pure, high crystallinity, hexagonal faceted HA grains were formed on all substrates. Therefore, it may be concluded that the use of pH together with the Ca-EDTA^{2-} complex regulate the HA hydrothermal crystallization process by reducing the concentration of supersaturating Ca^{2+} ions, enabling the engineering of a growth-controlled crystallization process.

Grain aspect ratio is reportedly a function of Ca^{2+} concentration along with PO_4^{3-} concentration, EDTA/Ca ratio, temperature, and pH [44,45]. Results reported above demonstrate that the HA grains formed in this study have the largest diameters (8-12 μm) and smallest aspect ratios (1-2) reported in the homogeneous precipitation hydrothermal HA film literature. A comparison of results from the literature cited above demonstrates an interdependence of the crystallization variables noted above, which makes it difficult to definitively conclude why a nearly equiaxed aspect ratio was achieved in this study.

Nonetheless, these conditions may be added to the literature to aid further understanding of the relation between grain aspect ratio and synthesis conditions.

The growth mechanism of the films may be inferred from cross-sectional SEM and top-on SEM results (Figure 2.7, Figure 2.8). Evaluation of cross sectional samples revealed the formation of dense, continuous, passivating films on all substrates. Based on passive film growth theory and data, film formation occurs through the development of an initial 2D film followed by 3D growth [60]. Evaluation of the surface and the cross-section of films indicate that after the formation of a passive 2D film, hexagonal grains grow independently and vertically, with their c-axis orthogonal to the substrate surface. The topology of the surface confirms this observation. This growth model follows XRD orientation results (Figure 2.6, Table 2.2), which suggest polycrystalline film thickening by competitive growth theory [59]. Figure 10 graphically illustrates this growth process. This topic is further studied further in a follow-up manuscript by Haders et al. [58].

Conclusions

Thermodynamic process simulation facilitates the engineering of hydrothermal processes for the development of designer hydroxyapatite films. The results presented here extend our ability to use equilibrium diagrams to explore processing variable space from HA particles to HA films. The use of a TEP/EDTA doubly regulated hydrothermal crystallization scheme, the first reported in the literature, enables both the growth controlled hydrothermal crystallization of passivating HA films on numerous substrates, and, apparently, the deposition of HA-substrate intermediates that improve film adhesion

in a single continuous process. These results emphasize that hydrothermal synthesis is particularly well suited to the crystallization of designer films with controlled size, morphology, crystallinity, phase, adhesion, and conformance for orthopedic and non-orthopedic applications.

Acknowledgements

We gratefully acknowledge the research support by the Rutgers Center for Ceramic Research, the National Science Foundation/Rutgers IGERT on Biointerfaces, the Department of Education/Rutgers GAANN in Molecular, Cellular, and Nanosystems Bioengineering, the Rutgers University Graduate School New Brunswick, the New Jersey Center for Biomaterials, and the Rutgers University Roger G. Ackerman Fellowship. The authors wish to thank Valentin Starovoytov for sputter coating film cross-sections, and Stryker Orthopaedics for donating Co28Cr6Mo samples.

Abbreviations

HA – Hydroxyapatite
PS-HA – Plasma sprayed hydroxyapatite
EDTA – Ethylenediamine-tetraacetic acid, $C_{10}H_{16}N_2O_8$
TEP - Triethyl phosphate, $C_6H_{15}O_4P$
Ca-P – Calcium-Phosphate
XRD – X-Ray diffraction
ACP – Amorphous calcium phosphate
FESEM – Field emission scanning electron microscopy
PDF – Powder diffraction file
ASTM - American Society for Testing and Materials
Ti6Al4V - Alloyed titanium with 6 wt.% aluminum and 4 wt.% vanadium
Co28Cr6Mo - Alloyed cobalt with 28 wt.% chromium and 4 wt.% molybdenum

Table

Table 2.1 Substrate roughness, phase, and relevant XRD peak ratios.

Substrate	Roughness, Ra (nm)	Identified Phase(s)	Ti - (0002)/(10-11)	Austenite - (200)/(111)	Co - (0002)/(10-11)
Ti6Al4V	414	Ti	1.19	-	-
Ti	1172	Ti	2.16	-	-
Rough- Ti6Al4V	3569	Ti, Corundum	0.36	-	-
Stainless Steel	531	Austenite	-	0.05	-
Co28Cr6Mo	678	Co	-	-	3.24
PDF 44-1294	-	Ti	0.3	-	-
PDF 33-0397	-	Austenite	-	0.45	-
PDF 05-0727	-	Co	-	-	0.6

Table 2.2 Deposited film crystallinity, (0002)/(21 $\bar{3}$ 1) peak ratio, particle size, thickness, and adhesion rating.

Substrate	HA Crystallinity (%)	(0002)/(21-31)	Avg Particle Diameter (μm)	Thickness (μm)	Adhesion Rating
Ti6Al4V	99	15.26	12 +/- 4	22 +/- 8	5A
Ti	99	14.51	12 +/- 4	13 +/- 3	5A
Rough- Ti6Al4V	99	4.04	11 +/- 2	18 +/- 4	5A
Stainless Steel	99	0.66	8 +/- 5	16 +/- 7	4A
Co28Cr6Mo	99	>>100	8 +/- 5	12 +/- 7	3A

Captions for Figures

Figure 2.1 Cross-sectional diagram Parr (Model 4731) reactor.

Figure 2.2 Calculated thermo-chemical phase equilibria diagram for the 0.232 molal $Ca(NO_3)_2$-0.232 molal EDTA-0.187 molal H_3PO_4-1.852 molal KOH-H_2O chemical system at 200 °C in the presence of various substrates (a) Titanium, (b) 316 Stainless steel, (c) Co-Cr. The black box represents the equilibrium pH/[m Ca^{2+}] (m=molal) combination calculated for each system under these conditions. The initial room temperature pH of the starting slurries has been recalculated to the pH at the experimental temperature. From that point the pH has been titrated to higher and lower values.

Figure 2.3 Autoclave heating dynamics were investigated by direct placement of K-type thermocouples into autoclaves placed in an oven pre-heated to 200 °C and filled with a model non-volatile liquid, technical grade glycerol.

Figure 2.4 Thermo-chemical modeling of Ca^{2+} concentration (m=molal) versus temperature as a function of ionic calcium species in a hydrothermal reaction solution containing (a) 0.05 molal $CaCl_2$-0.05 molal Na_2H_2EDTA-0.05 molal NaH_2PO_4-NaOH-H_2O (b) 0.232 molal $Ca(NO_3)_2$-1.852 molal KOH-0.232 molal EDTA-H_2O both in the presence of titanium.

Figure 2.5 Scanning electron micrographs of various substrates before hydrothermal treatment. (a) Ti6Al4V, (b) Ti, (c) Roughened Ti6Al4V, (d) 316 Stainless Steel, (e) Co28Cr6Mo alloy (Magnification x500).

Figure 2.6 X-ray diffraction patterns of various substrates before and after hydrothermal treatment for 24 h at 200 °C. (a) Ti6Al4V, (b) Ti, (c) Roughened Ti6Al4V (d) Stainless Steel, (e) Co28Cr6Mo alloy. For each substrate: (1) pre-hydrothermal treatment, (2) post-hydrothermal treatment.

Figure 2.7 Scanning electron micrographs of films deposited on various substrates after hydrothermal treatment for 24 h at 200 °C. (a) Ti6Al4V, (b) Ti, (c) Roughened Ti6Al4V, (d) Stainless Steel, (e) Co28Cr6Mo alloy (Magnification x500).

Figure 2.8 Scanning electron micrographs of the cross-sections of films deposited on various substrates after 24 h of hydrothermal treatment at 200 °C. (a) Ti6Al4V (b) Ti (c) Roughened Ti6Al4V (d) Stainless Steel (e) Co28Cr6Mo alloy (Magnification x500).

Figure 2.9 Scanning electron micrographs of the surface of representative hydroxyapatite films deposited on substrates by hydrothermal treatment (24 h at 200 °C) after adhesion testing. (a) Roughened Ti6Al4V, (b) Roughened Ti6Al4V, (c) Co28Cr6Mo alloy, (c) Co28Cr6Mo alloy.

Figure 2.10 Proposed film growth mechanism - competitive polycrystalline film growth - as concluded from cross-sectional SEM and XRD orientation results using square facetted grains with a (111) fast growth direction to explain the process. Initially, a passive 2D film is formed. Subsequently, thickening of the initial 2D film leads to the termination of grains with (010), (100), and (001) texture by crystals with (111) texture. This occurs because the crystals with (111) texture are oriented to have their fast growth direction normal to and in the plane of the film. Adapted from Thompson et al. [59]

Figures

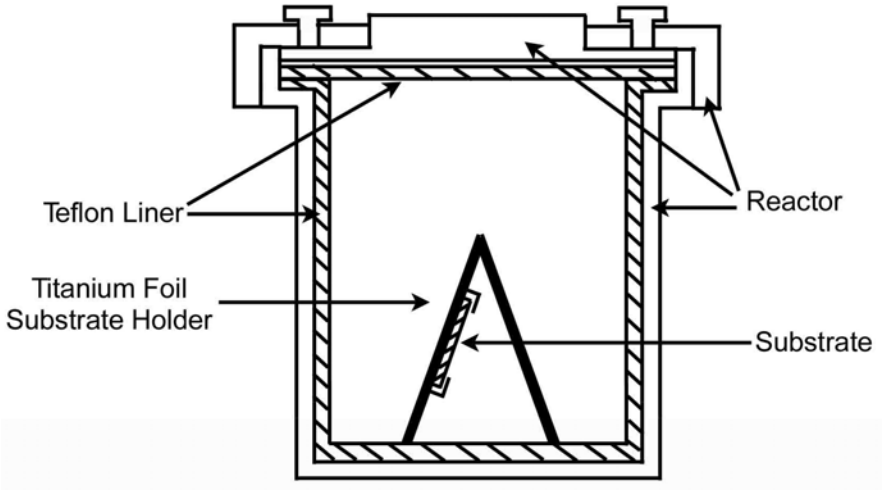

Figure 2.1

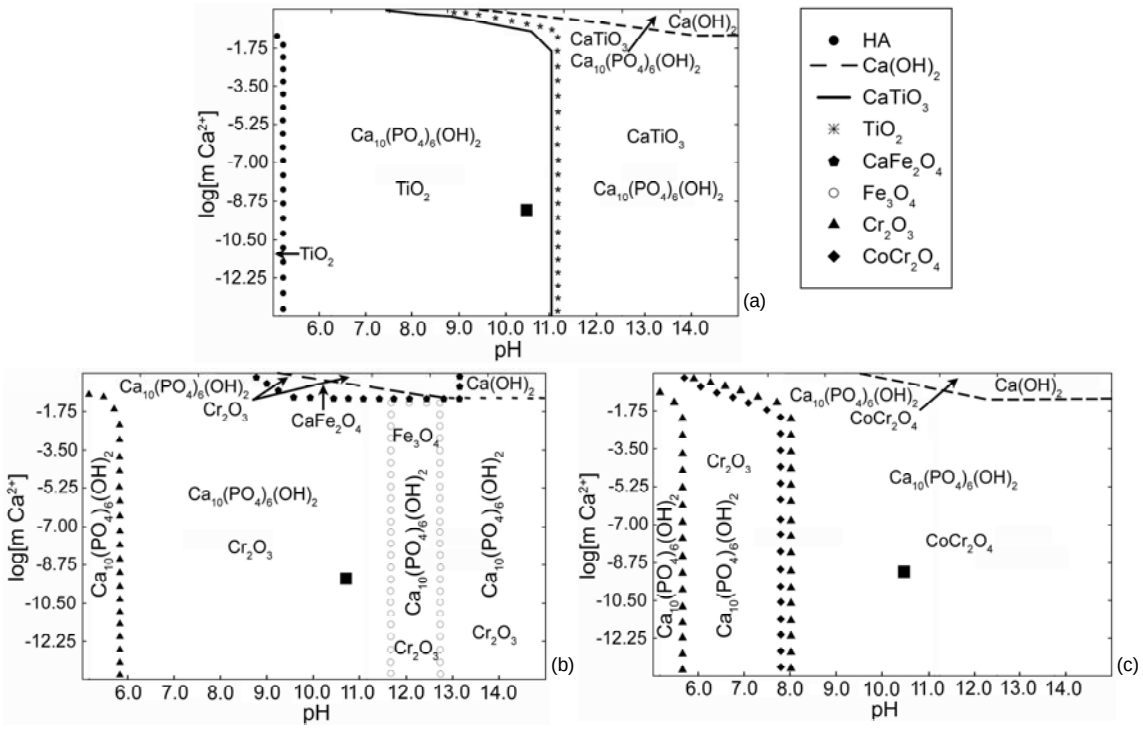
HA
Ca(OH)2
CaTiO3
TiO2
CaFe2O4
Fe3O4
Cr2O3
CoCr2O4
log[m Ca2+]
pH
(a)
(b)
(c)

Figure 2.2

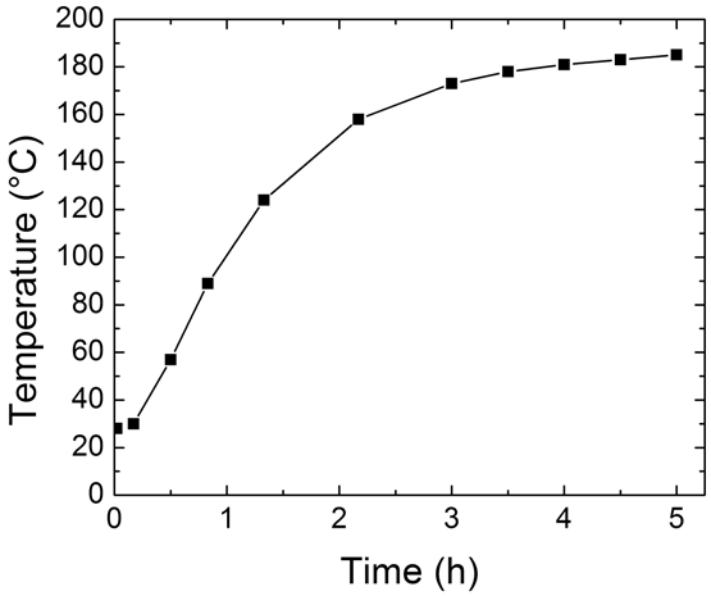
Temperature (°C)
Time (h)
0
20
40
60
80
100
120
140
160
180
200
0
1
2
3
4
5

Figure 2.3

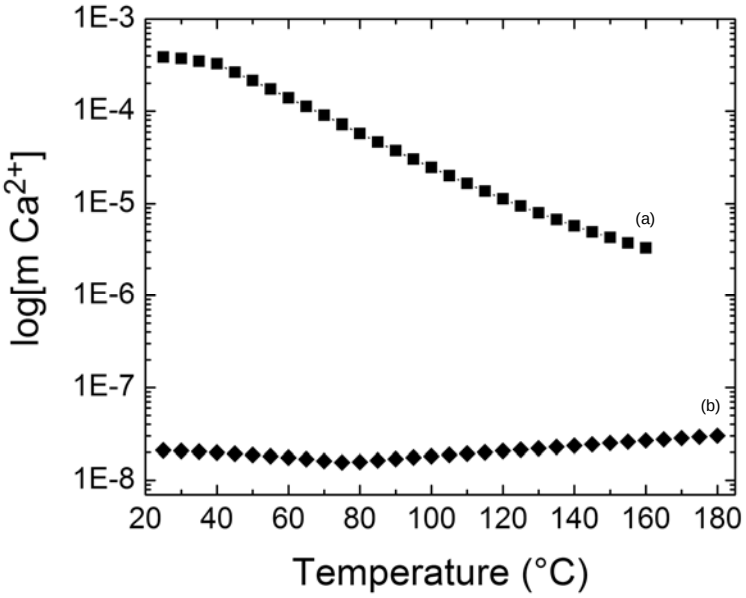
1E-3
1E-4
1E-5
1E-6
1E-7
1E-8
log[m Ca2+]
(a)
(b)
20
40
60
80
100
120
140
160
180
Temperature (°C)

Figure 2.4

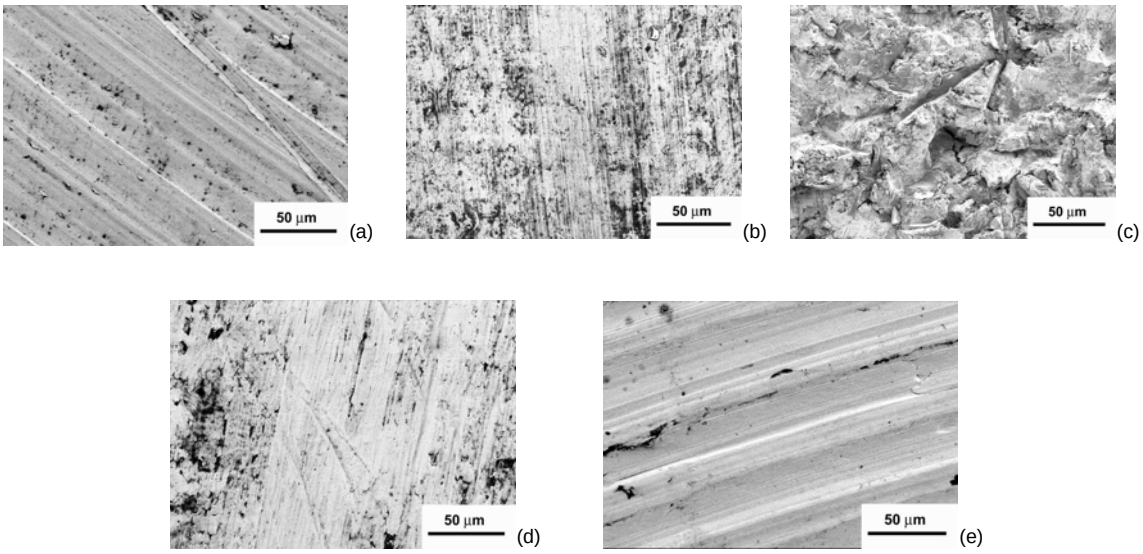

Figure 2.5

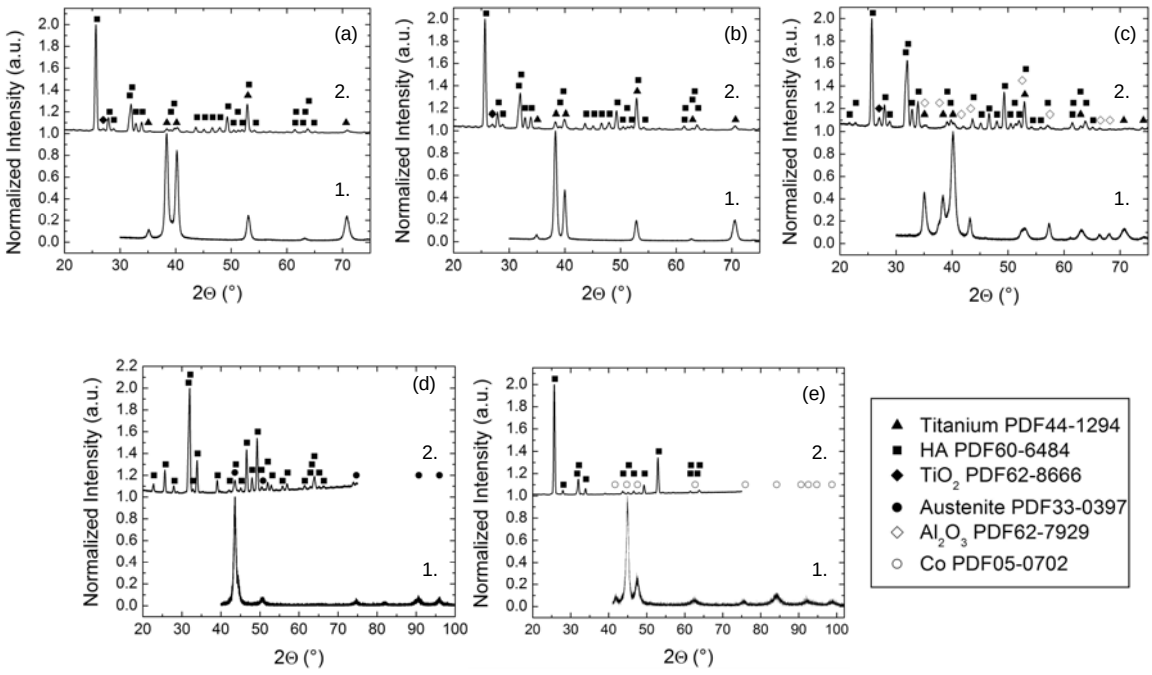
(a)
(b)
(c)
(d)
(e)
1.
2.
Normalized Intensity (a.u.)
2Θ (°)
Titanium PDF44-1294
HA PDF60-6484
TiO2 PDF62-8666
Austenite PDF33-0397
Al2O3 PDF62-7929
Co PDF05-0702

Figure 2.6

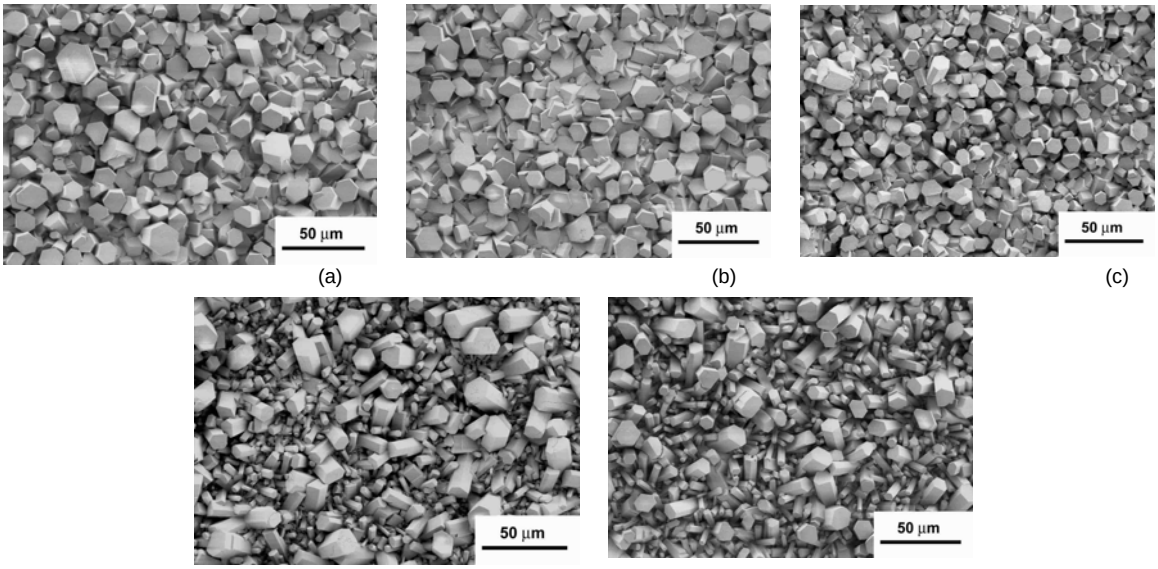

Figure 2.7

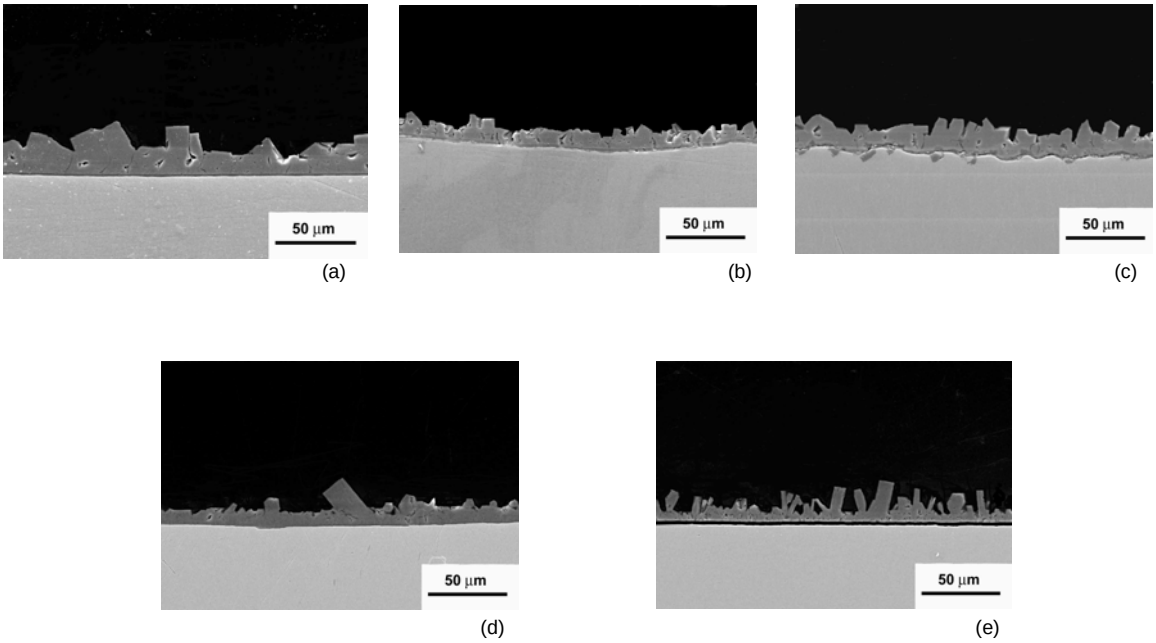

Figure 2.8

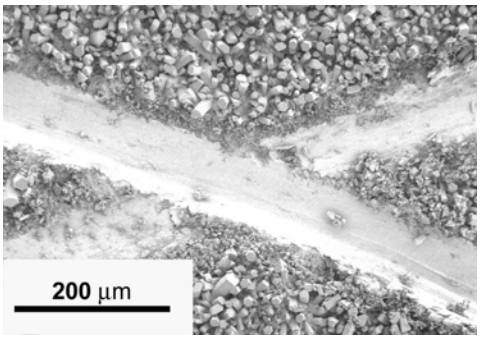

(a)

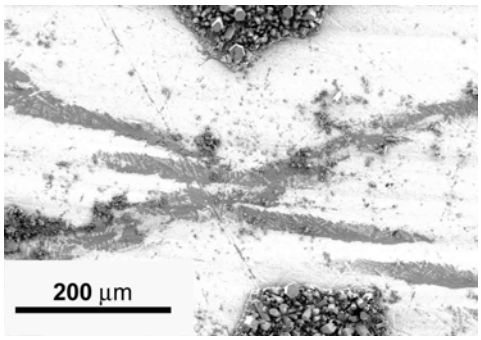

(c)

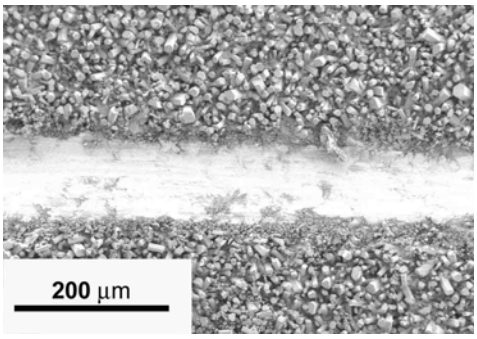

(b)

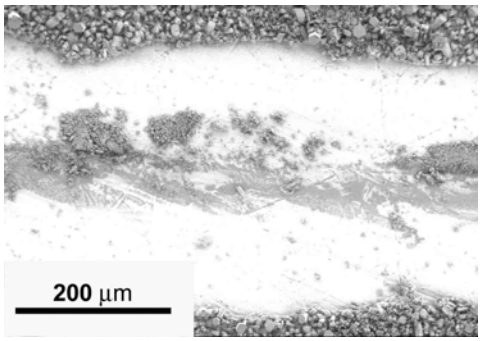

(d)

Figure 2.9

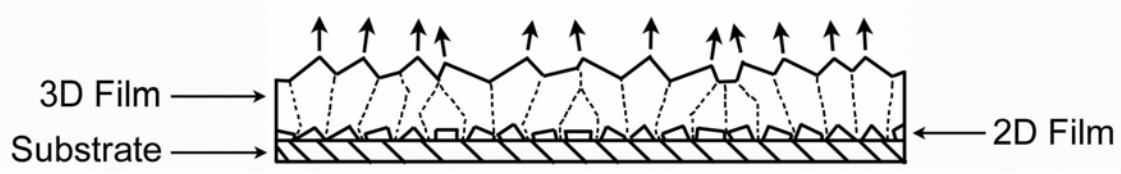

Figure 2.10

Chapter 3

Phase Sequenced Deposition of Calcium Titanate/Hydroxyapatite Films with Controllable Crystallographic Texture onto Ti6Al4V by TEP Regulated Hydrothermal Crystallization.

D. J. Haders[1,2,3], A. Burukhin[1], Y. Huang[3], D.J.H. Cockayne[3], R.E. Riman[1,2]

[1] Department of Material Science and Engineering, Rutgers, The State University of New Jersey, Piscataway, New Jersey

[2] Department of Biomedical Engineering, Rutgers, The State University of New Jersey, Piscataway, New Jersey

[3] Department of Materials, University of Oxford, Oxford, United Kingdom

Abstract

The aim of this study was to investigate the use of tri-ethyl phosphate (TEP) to regulate the hydrothermal crystallization of hydroxyapatite (HA) films onto Ti6Al4V substrates. The growth mechanism of the HA film and development of [0001] HA crystallographic texture were studied. Films were crystallized in a 0.232 molal $Ca(NO_3)_2$-0.232 molal EDTA-0.187 molal TEP–1.852 molal KOH-H_2O chemical system with a final isothermal temperature of 200 °C, and then evaluated at synthesis times from 0-46 h by XRD, FESEM, TEM, EDX, and X-ray pole figures. Thermodynamic phase stability diagrams were calculated to validate experimental findings. XRD, FESEM, TEM, and EDX results demonstrated the crystallization of a $CaTiO_3$ film below 180 °C and a HA film above 180 °C. SEM and X-ray pole figure analysis revealed a refinement of the orientation of the (0002) HA crystallographic plane and the c-axis of hexagonal single crystals of HA,

[0001], with increasing synthesis time. Based on these results it is concluded that the use of TEP- regulated hydrothermal crystallization enables the deposition of $CaTiO_3$ and then HA in a single, phase sequenced process, the first such process reported in the hydrothermal HA literature. The HA film is deposited by means of a competitive growth mechanism that enables the [0001] crystallographic orientation of hexagonal single crystals to be engineered with synthesis time.

Introduction

Hydroxyapatite (HA), $Ca_{10}(PO_4)_6(OH)_2$, the stoichiometric equivalent of the ceramic phase of bone, is considered the preferred material for hard tissue replacement due to its bioactivity [1,3,52]. However, bioinert metals are utilized in load-bearing orthopedic applications on account of the poor mechanical properties of HA [3-6]. Consequently, attention has been given to HA coatings for metallic orthopedic implants in an effort to take advantage of the bioactivity of HA and the mechanical properties of metals. Numerous reviews have described how HA-coated metallic orthopedic implants posses many advantages as compared with alternative orthopedic implant surfaces including sintered metallic porous coatings, plasma-sprayed titanium coatings, and roughened or untreated metallic implant surfaces [5,7-11]. First, HA films bridge larger gaps between the implant and bone with new bone tissue. Second, they accelerate bone apposition. Third, HA films enable more fixation in osteoporotic bone. Finally, they have increased bone-implant bond strength.

Commercially, the plasma spray process (PS-HA) is the method most often used to deposit HA films on metallic implants [9,12,13]. Films applied to the clinically relevant Ti6Al4V alloy (alloyed titanium with 6 wt.% aluminum and 4 wt.% vanadium), however, lack a Ti-HA chemical intermediate bonding layer such as $CaTiO_3$, and rely on mechanical interlock rather than chemical bonding to adhere the film to the substrate [16,19,61]. As a result, *in vivo* coating delamination has been reported due to the greater interfacial strength between HA and bone, than HA and titanium [6,10,15,20,21]. Concerns have also been raised about the consequences of PS-HA's low crystallinity, lack of phase purity, passivation properties, and line-of-sight-limitations [12,13,22]. In addition, plasma sprayed HA films fail to take advantage of hexagonal HA crystallography to functionalize the film surface with the bioactive $\{10\bar{1}0\}$ crystallographic face and actively engineer protein adhesion. Molecular modeling and *in vitro* studies have shown that acidic bone proteins and other proteins found to bind HA with high affinity, bind to the $\{10\bar{1}0\}$ face of HA, which is prominently displayed on the six equivalent faces of hexagonal crystals of HA [25-27]. HA films deposited by other techniques including sol-gel, pulsed laser deposition, magnetron sputtering, ion-beam deposition, and biomimetic crystallization share all or some of PS-HA's limitations [3,28-32]. Therefore, there is a need to develop inexpensive reproducible HA film crystallization processes for Ti6Al4V substrates that deposit highly crystalline, phase pure, passivating, conformal HA films with engineered hexagonal crystallography and a Ti-HA chemical intermediate bonding layer.

In a previous paper, we reported that the use of triethyl phosphate (TEP)/ ethylenediamine-tetra-acetic acid (EDTA) doubly regulated hydrothermal crystallization enabled the deposition of highly crystalline, phase pure, passivating, hexagonal-grained HA films on multiple substrates at 24 h and 200 °C [62]. In addition, it was determined both that TEP acted as a delayed release phosphate source, which released PO_4^{3-} at 180 °C, and that HA film adhesion was superior on titanium-based substrates as compared to 316 stainless steel and Co28Cr6Mo substrates [62]. One potential explanation for the latter result is the formation of an adhesive $CaTiO_3$ intermediate layer on Ti substrates prior to HA deposition. Specifically, it is hypothesized that the use of TEP necessitates a continuous two-step phase sequenced film deposition process. In the first step, the reaction mixture is heated from room temperature to 180 °C. During this step incomplete TEP hydrolysis and the absence of free phosphate ions exclude the possibility of HA crystallization. By delaying the release of uncomplexed phosphate ions, however, reactions involving calcium ions and the substrate may be initiated to form adhesive HA-Ti interfacial layers, such as $CaTiO_3$, that enable substrate/film chemical bonding. Above 180 °C, complete TEP hydrolysis and free PO_4^{3-} then enable the deposition of HA. Together, elemental (Energy dispersive X-ray spectroscopy, EDX), phase (X-ray diffraction, XRD), and physical (Transmission electron microscopy, TEM/Scanning electron microscopy, SEM) analyses of films at multiple deposition time points has the potential to confirm this hypothesis. Therefore, there is a need to examine the film-substrate interface and the time-lapsed crystallization process to determine if the use of TEP enables the deposition of $CaTiO_3$ and then HA in a single phase-sequenced process on titanium substrates.

Passive film growth theory and data report that passive film formation occurs through the formation of a compact primary layer followed by growth of a porous secondary layer [60]. Upon formation of a continuous polycrystalline film (compact primary layer) thickening (secondary layer growth) occurs epitaxially on existing grains and preferentially in certain crystallographic directions resulting in crystallographic texturing that increases with film thickness [59]. In a previous study it was demonstrated that our hydrothermal crystallization process enables the deposition of a passive film with [0001] crystallographic texture [62]. Thus, it is hypothesized that if the films reported here follow this growth mechanism, then the [0001] crystallographic orientation of the crystals on the surface of the film may be engineered through control of synthesis time. Physical (SEM), phase (XRD), crystallographic (XRD), and texture (Pole Figure) analyses of films at multiple deposition time points have the potential to confirm this hypothesis. Therefore, there is a need to understand the growth mechanism of these films, and determine if the regulation of synthesis time presents a potentially novel route to engineer the [0001] crystallographic orientation of hexagonal HA grains. One potential application of controllable crystallographic orientation includes engineering orientation to preferentially increase the surface area of specific HA crystallographic faces presented to the body, such as the bioactive $\{10\bar{1}0\}$ face noted above.

This study analyzes the potential of utilizing the delayed-release phosphate source TEP to engineer a single hydrothermal crystallization process that deposits $CaTiO_3$ and then HA

in a phase sequenced process. The study then investigates the HA film growth mechanism and the development of [0001] crystallographic texture with synthesis time.

Experimental Procedure

Ti6Al4V alloy was chosen as the substrate for this study due to its clinical use in load-bearing orthopedic applications. Ti6Al4V was also chosen due to the perfect adhesion value (5, ASTM D3359) reported for HA films previously synthesized by this method on this substrate [62]. Ti6Al4V samples were treated hydrothermally for various times and characterized to investigate the phases deposited by this hydrothermal method, hexagonal grain crystallography, the film growth mechanism, and [0001] crystallographic orientation with synthesis time. Thermodynamic phase diagrams, based on previously reported TEP kinetics studies [62], were then created to validate/explain experimental results.

a. Film Synthesis

Ti6Al4V samples were treated hydrothermally for various times to investigate the film growth process in terms of previously reported TEP kinetics and autoclave heating dynamics, [62] and time. One-inch diameter rods of Ti6Al4V alloy (ASTM-B348 Grade 5, McMaster Carr, Dayton, NJ) were cut into discs, 1 in (diameter) x 1/8 in (thickness), and used as substrates. All substrates, titanium foil (0.127 mm, 99.7%, Sigma-Aldrich, St. Louis, MO) substrate holders, and Teflon ® reaction vessel liners (125 mL, model 4731, Parr Instrument, Moline, IL) were cleaned with Citronox detergent (Alconox, White Plains, NY), acetone (Fisher Scientific), ethyl alcohol (Pharmco-AAPER, Brookfield, CT), and deionized water and dried in a 60 °C oven prior to synthesis.

One set of solution conditions was used for all hydrothermal experiments. Aqueous stock solutions of 0.232 molal calcium nitrate tetrahydrate, $Ca(NO_3)_2*4H_2O$ (99.38 %, Fisher Scientific), 0.232 molal ethylenediamine-tetraacetic acid (EDTA), $C_{10}H_{16}N_2O_8$ (99.4 %, Fisher Scientific), 0.187 molal triethyl phosphate (TEP), $C_6H_{15}O_4P$ (99.8+ %, Sigma Aldrich), and 1.852 molal potassium hydroxide, KOH (89.3 %, Fisher Scientific) were prepared as follows:

Calcium nitrate tetrahydrate, EDTA, and TEP were mixed together and dissolved in deionized H_2O. KOH was dissolved in a second container in deionized H_2O. Once dissolved, the KOH solution was placed in a cold-water bath and cooled to room temperature. When cool, the KOH solution was added to the former solution and stirred until visible particulates had dissolved. The stock solution was then filtered (220 nm pore size, Nalgene, Rochester, NY) and stored in a tightly sealed container.

The typical hydrothermal reaction was conducted as follows: The substrate was fixed in the substrate holder and placed inside a 125 ml Teflon®-lined reaction vessel (4731 reactor, Parr Instrument). The substrate holder placed the sample in a position that inhibited the settling of homogeneously formed particles onto the surface by means of gravity [62]. Stock solution, 70 mL, was added to the reaction vessel, which was then sealed. The reactor was then placed in an oven pre-heated to 200 °C for 2, 4, 6, 8, 10, 12, 14, 24, or 46 h. The reactor was removed from the oven and allowed to cool to room temperature in air. The substrate was removed from the reactor and rinsed for several

minutes in running tap water and then in deionized water. The sample was then placed in a 60 °C oven to dry.

b. Film Characterization

X-ray diffraction (XRD) (step size = 0.005 °, 1 step/sec, 45 KV, 40 mA, Ni-filtered CuK_{α} radiation, parallel beam optics, Philips Hi-Resolution X'PERT X-Ray Diffractometer, PANalytical B.V., Almelo, Netherlands) was used to determine the phases present in the films and the substrate. Field emission scanning electron microscopy (FESEM) (3kV, DSM 982 Gemini, Carl Zeiss, Oberkochen, Germany) was used to examine the substrate and films. Transmission electron microscopy (TEM) and Energy Dispersive X-Ray Spectroscopy (EDX) samples were prepared one of two ways. Samples, 2 mm x 3 mm x 500 μm, were cut from a 46 h sample using a diamond saw (Vari/Cut VC-50, Leco Corporation, St. Joseph, MI). Samples were mechanically polished to a thickness of less than 50 μm and mounted on a copper grid. A 1 μm wide area of the film-substrate interface was then polished to electron transparency, approximately 100 nm, using a Focused Ion Beam (FIB) (FIB 200, FEI, Hillsboro, Oregon) and an H-bar technique. The FIB was used to directly cut electron transparent samples from a 6 h sample using a lift-out technique, which were then mounted on copper grids for analysis. Transmission electron microscopy analysis was carried out on a Philips CM20 (200 kV, FEI, Hillsboro, Oregon) and EDX analysis was carried out on an attached Oxford Instruments Inca energy dispersive X-ray spectrometer (Whitney, Oxon, United Kingdom). For EDX line-scan data the background was calculated at each position on the sample by averaging the background counts at three unique points on the keV spectrum (keV = 3, 6.5, 15) that did not overlap with an elemental peak. A standard deviation of the background was then

calculated and added to the average background value at each position on the sample. This value was then subtracted from the element counts at each corresponding position on the sample to remove the background. $CaTiO_3$ film thickness was computed by direct measurement of the thickness of TEM cross-sections at 10 equally spaced points along the length of the micrograph using image analysis software (Adobe Photoshop, Adobe Systems Inc., San Jose, CA). Average film thickness and the standard deviation of the mean were calculated using Excel (Microsoft, Redmond, WA). The [0001] crystallographic texture of films was evaluated by collecting pole figures of the (0002) HA crystallographic plane using a Philips Hi-Resolution X'PERT X-Ray Diffractometer (PANalytical, Netherlands, 45 KV, 40 mA, Ni-filtered CuK_α radiation, Φ: 0 °-360 ° (substrate rotation), 1 °/sec, Ψ: 0 °-90 ° (substrate tilt - relative to the substrate orthogonal), 1 °/step) for films deposited for 8, 10, 14, and 24 h as well as for a randomly oriented HA powder sample synthesized in-house. Intensity plots, which represent the population distribution of (0002) planes relative to the substrate surface, are normalized to the most intense psi/phi combination in each plot, varying from 0-1 arbitrary units. To further describe the crystallographic texture, the intensity of phi from 0 °-360 ° was totaled for each degree of psi to give an intensity distribution versus psi. This distribution was then divided by the psi intensity distribution of the randomly oriented powder sample to correct for changes in illumination area with tilt angle and defocus, and to provide data in terms of multiples random distribution (MRD) [63], which is given by the following expression:

$$(4)\quad MRD^{X^0} = \frac{\psi_S^{X^0}}{\psi_{ROPS}^{X^0}}$$

where $\psi_S^{X^0}$ is the x-ray intensity at Ψ = X ° for the sample, $\psi_{ROPS}^{X^0}$ is the x-ray intensity at Ψ = X ° for the randomly oriented powder sample, and MRD^{X^0} is the multiples random of the sample at Ψ = X °. To determine if hexagonal grains were single crystals, the 6 internal angles of 5 grains were measured from a 24 h synthesis SEM micrograph using image analysis software (Abobe Photoshop).

c. Thermodynamic Process Simulation

All thermodynamic diagrams were calculated using OLI thermo-chemical simulation software (OLI Systems, Inc., Morris Plains, NJ). The fundamental basis for the algorithms used in the software is reported in Lencka and Riman [53]. HA thermodynamic phase equilibria models created using this software have been reported previously by Riman et al. and Haders et al. [51,62].

Phase stability diagrams for the $Ca(NO_3)_2$ – EDTA – KOH - H_2O system in the presence of titanium substrates at 50 °C and 180 °C were calculated. These diagrams thermodynamically model the $Ca(NO_3)_2$ – EDTA - TEP – KOH - H_2O – Ti system during reactor heating and prior to full hydrolysis of TEP at 180 °C [62]. The software database does not contain TEP because there is no reported thermodynamic data for TEP in the literature. Due to the absence of TEP data, the results from the model do not take into account the products of partial TEP hydrolysis, namely $2H^+$ and $2C_2H_5OH$. After the creation of phase diagrams, the specific pH/$[Ca^{2+}]$ point for the 0.232 molal $Ca(NO_3)_2$– 0.232 molal EDTA–1.852 molal KOH–H_2O-Ti system at 50 °C and 180 °C was calculated and plotted on each respective diagram.

The phase stability diagram for the $Ca(NO_3)_2$ – EDTA - H_3PO_4 – KOH - H_2O system in the presence of a titanium substrate at 180 °C was also calculated. This diagram models the reaction conditions of the $Ca(NO_3)_2$ – EDTA - TEP – KOH - H_2O – Ti system after full hydrolysis of TEP at 180 °C [62]. Since the thermodynamic software database does not include TEP data, H_3PO_4 was substituted as a component. The use of this acid allows the model to account for products of TEP hydrolysis, PO_4^{3-} and $3H^+$, without the explicit use of TEP. The third product of TEP hydrolysis, C_2H_5OH, was ignored due to its dilute state in the solution, 0.561 molal after full TEP hydrolysis. This omission was justified in a previous manuscript by comparing the phase diagrams of the 0.232 molal $Ca(NO_3)$-0.232 molal EDTA-0.187 molal H_3PO_4-1.852 molal KOH-Ti-H_2O chemical system and the 0.232 molal $Ca(NO_3)$-0.232 molal EDTA-0.187 molal H_3PO_4-0.561 molal C_2H_5OH-1.852 molal KOH-Ti-H_2O chemical system at 200 °C [62]. A comparison of the two diagrams demonstrated no differences in the position of phase boundaries at pH relevant to the work in this study. After the creation of the phase diagram the specific pH/Ca^{2+} combination for the 0.232 molal $Ca(NO_3)_2$-0.232 molal EDTA-0.187 molal H_3PO_4-1.852 m KOH-H_2O-Ti chemical system at 180 °C was calculated and plotted on the diagram. The phase stability diagram for the $Ca(NO_3)_2$ – EDTA - H_3PO_4 – KOH - H_2O system in the presence of a titanium substrate at the system's isothermal temperature, 200 °C, was presented previously [62].

Results

a. Film-Substrate Interface

Figure 3.1 and Figure 3.2 display time matched X-ray diffraction patterns and scanning electron micrographs of the non-treated Ti6Al4V substrate and of Ti6Al4V substrates after 2 and 4 h of hydrothermal treatment, which is prior to full TEP hydrolysis based on previously reported results [62]. At 2 h, no phase other than titanium is detected by XRD. SEM micrographs, however, demonstrate the presence of a nano-pitted film. At 4 h $CaTiO_3$ and titanium are detected by XRD. At this time the substrate surface is covered with a passivating film composed primarily of overlapping inter-grown rectangular plates less than 1 μm in apparent width and thickness, as displayed in Figure 3.2. Based on these results it can be concluded that the passivating film is $CaTiO_3$. The film observed at 2 h is likely a thin precursor to the crystalline film observed at 4 h, such as amorphous $CaTiO_3$, that was present in too limited of a quantity to be detected by XRD.

Several large rectangular grains are observed by SEM, in addition to the films formed at 2 and 4 h (Figure 3.2). XRD phase analysis detection capabilities typically do not enable the detection of phases that compose less than 3-5 wt% of the sample. Therefore, it is possible that these features could represent a second undetected phase such as HA. Figure 3.3 displays TEM micrographs and EDX elemental maps of a cross-section of a film at 6 h synthesis time cut from an area containing only the film and rectangular grains observed at 4 h. EDX elemental analysis reports that titanium, calcium, and oxygen have overlapping distributions in an area that morphologically corresponds to the film and two protruding rectangular grains. Phosphorus mapping provides no evidence for its presence in either the film or the unidentified rectangular grains. The phosphorus that is observed in the EDX map is a false positive - created due to an overlap in electron energy with

platinum that was used to coat the film surface. Thus, it is possible that the passivating film and the rectangular grains at 2 and 4 h are both $CaTiO_3$, and together compose a continuous, phase pure film with an average film thickness of 479 +/- 27 nm.

The structure of the Ti/$CaTiO_3$ interface was analyzed by TEM and EDX line-scan (Figure 3.3, Figure 3.4). TEM micrographs display a 20-40 nm bright line that runs the length of the sample. This line was concluded to represent the morphological interface that physically separates the deposited $CaTiO_3$ film from the Ti substrate. EDX elemental analysis of the chemical interface indicates that titanium concentration reduces gradually from the bulk Ti substrate to the Ti-$CaTiO_3$ morphological interface, decreases rapidly across the morphological interface, and reaches a constant value in the $CaTiO_3$ film. From this result, it can be concluded that titanium diffuses from the Ti bulk and through the morphological interface to form $CaTiO_3$. Calcium, concurrently, is found not only in the $CaTiO_3$ film but also in the morphological interface and in the substrate to a depth of over 100 nm. The physical region of this chemical transition zone is noted in the TEM micrograph in Figure 3.3b. Based on this information it may be concluded that the Ti substrate/$CaTiO_3$ film chemical interface is composed of a layered structure that transitions from the bulk Ti substrate to the $CaTiO_3$ film through a 100+ nm chemical transition zone that extends beyond the morphological interface and into the substrate.

Transmission electron micrographs, EDX elemental maps, and EDX elemental line-scan data were obtained from a cross-section near the substrate/film interface of a film synthesized for 46 h. Micrographs, maps, and data were analyzed to determine if

subsequent HA film crystallization, after 4 h, altered the $CaTiO_3$ film or the Ti/$CaTiO_3$ interface (data not shown). Transmission electron micrographs display a 90-110 nm bright line that was interpreted to represent the morphological interface that physically separates the deposited $CaTiO_3$ film from the Ti substrate, similar to that seen in the 6 h sample. Energy dispersive X-ray spectroscopy mapping and line scan analysis also reveal results similar to those observed in the 6 h sample, with respect to the chemical interface. Elemental mapping of the film immediately above the substrate demonstrates a continuous several hundred nanometer thick region that contains titanium, calcium, and oxygen, but no phosphorus. Line scan data reveals that titanium diffuses from the bulk Ti substrate and through the morphological interface to form $CaTiO_3$. Line scan data also demonstrate that calcium is present not only in the $CaTiO_3$ film but also in the morphological interface and in the substrate to a depth of over 100 nm. Based on this information it may be concluded that the $CaTiO_3$ film and the Ti/$CaTiO_3$ interfacial structure are maintained at synthesis times up to at least 46 h and is not significantly affected by the subsequent HA film growth process - a 3-D phase mix of $CaTiO_3$ and HA is not formed at the titanium interface at synthesis times after 4 h.

b. Hydroxyapatite Film Growth

Figure 3.5 and Figure 3.6 display corresponding X-ray diffraction patterns and SEM micrographs of films deposited on Ti6Al4V substrates for 6, 8, and 10 h by hydrothermal treatment. At 6 h phase analysis demonstrates that the $(21\bar{3}1)$ HA peak, at 31.7 °, is present along with peaks representing $CaTiO_3$ and Ti. At this time point SEM demonstrates the formation of hexagonal grains on the underlying $CaTiO_3$ film. Based on this information it may be concluded that the hydrothermal crystallization process

presented here deposits hexagonal grains of HA on the $CaTiO_3$ interfacial layer beginning after 4 h synthesis time.

The relationship between hexagonal grain morphology and the crystallographic unit cell was established by measuring the angles between equivalent faces. Hydroxyapatite is in the 6/m crystal class. One of the typical forms of crystals with this symmetry is the hexagonal prism, which is composed of 6 faces that are parallel to the same principal crystallographic axis [43]. If the hexagonal grains that make up the HA films reported here are single crystals of this form, then Steno's law states that the internal angles between adjacent equivalent faces should be constant [43]. Based on fundamental geometry this angle is 120 ° for hexagons. The average measurement of the angles between the six equivalent faces of 5 different grains was found to be 120.5 ° +/- 3.6 °. Thus, the measured internal angle and the low standard deviation confirm that the hexagons are single crystals of HA. The small observed standard deviation is likely due to limitations in the measurement technique.

As synthesis time increases the XRD peak intensity of HA peaks increases in absolute and relative terms as compared to Ti and $CaTiO_3$ peaks (Figure 3.5). Based on XRD fundamentals peak intensity is a function of the number of diffracting grains. Consequently, the change in HA peak intensity must be related to an increase in coverage and/or thickness of the HA film at reaction times of 6 h or longer. The reduction in the relative peak height of $CaTiO_3$ and Ti is then a result of fewer incident x-rays reaching the $CaTiO_3$ film and Ti substrate and fewer diffracted x-rays escaping the sample as a

result of x-ray absorption. SEM micrographs confirm this conclusion (Figure 3.6). From 6 h the originally dispersed hexagonal HA crystals are observed to nucleate and grow until 10 h. At this time a nearly continuous film is formed on top of the initial $CaTiO_3$ film. There is no indication of nucleation and/or growth of the $CaTiO_3$ film or of rectangular $CaTiO_3$ grains during this time. Based on this information it may be concluded that the film formed from 4 – 10 h is a continuous HA film and not a 3-D $CaTiO_3$/HA phase mixture.

Figure 3.6 was examined in further detail to determine the role of nucleation in the formation of the HA film from 4 – 10 h. At both 6 and 8 h a minority of hexagonal crystals less than 1 μm in size are observed among a majority of larger, micron plus sized, crystals on the surface of the $CaTiO_3$ film. At 10 h no sub-micron grains were observed in the small voids of the nearly continuous film. Based on this result it can be concluded that heterogeneous HA nucleation on $CaTiO_3$ begins sometime after 4 h of hydrothermal treatment and continues either intermittently or continuously until at least 8 h. Concurrently, it may be concluded that the heterogeneous nucleation supersaturation limit for Ca^{2+} and PO_4^{3-}, in regard to HA, is crossed soon after 4 h. and is maintained continuously or intermittently until at least 8 h.

Figure 3.6 was also examined in detail to determine the role of crystal growth in the formation of the HA film from 4 – 10 h. First, the micrographs reveal that the size of the largest “non-agglomerated” crystals, which are approximately equiaxed, increases from about 1.5 – 4 μm from 6 – 8 h. Consequently, the thickness of the incomplete film at 8 h

is observed to be approximately 4 μm because the crystals are equiaxed. Second, as crystals grow it is observed that they grow over and around each other, which results in crystals becoming interlocked and the formation of grain clusters with irregular surface morphology. Third, at 8 h the film is continuous with the exception of islands, several microns to tens of microns in diameter, which contain non-interlocked micron-plus sized crystals along with smaller sub-micron crystals. By 10 h, these islands are nearly completely filled in with equiaxed crystals of approximately 10 μm. The film morphology in these areas is observed to be less faceted, however. From these observations it is concluded that the reaction conditions used in this study lead to the formation and growth of equiaxed hexagonal crystals of HA, which grow over and around each other upon impingement. The islands observed at 8 h are potentially a consequence of low nuclei density in some areas at early time points. As a consequence of the low density, crystals are able to grow without impingement from other crystals, leading to the less faceted film morphology observed in some regions at 10 h.

Figure 3.7 displays X-ray diffraction patterns of films deposited on Ti6Al4V substrates for 12, 14, and 24 h by hydrothermal treatment. As synthesis time increases the XRD peak intensity of HA peaks increases in absolute and relative terms as compared to Ti and $CaTiO_3$ peaks, indicating further film thickening. In addition, the (0002)/($21\bar{3}1$) XRD peak intensity ratio increases substantially during this time, indicating (0002) crystallographic texturing.

To further evaluate this film thickening mechanism X-ray diffraction pole figure analysis was utilized (Figure 3.8). Pole figures report a refinement of the (0002) population distribution relative to the sample surface from 8-24 h. A quantitative examination of the pole figures in terms of multiples random distribution (MRD) is displayed in Figure 3.9. The data at 24 h confirm the trend reported in Figure 3.8 and demonstrates that the volume fraction of hexagonal HA grains with their (0002) plane parallel to the sample surface (psi = 0°) is several multiples greater than expected for a randomly oriented sample. Based on this analysis it is concluded that film thickening after 10 h leads to increasing [0001] crystallographic orientation with synthesis time.

Time lapsed SEM micrographs from 12 – 24 h are displayed in Figure 3.10. At 12 h it is observed that a complete and continuous film has formed and that numerous hexagonal rods are protruding from the underlying film. As synthesis time increases from 12 – 24 h a qualitative increase in hexagonal crystals with their c-axis, [0001] crystallographic direction, perpendicular to the substrate surface is observed. These results agree with XRD/pole figure results, which concluded that film thickening leads to increasing [0001] crystallographic orientation with synthesis time.

Discussion

In a previous study, analysis of TEP hydrolysis kinetics revealed that under the reaction conditions used here free phosphate was not available for the formation of HA until 180 °C at 4 h synthesis time [62]. Previous results also demonstrated that HA film adhesion was superior on titanium based substrates as compared to 316 stainless steel and Co28Cr6Mo

substrates [62]. Based on these results it was hypothesized that the use of TEP necessitated a continuous, two-step, phase sequenced film deposition process during reactor heating from room temperature to 200 °C. More specifically, it was hypothesized that below 180 °C incomplete TEP hydrolysis and the absence of free phosphate ions excluded the possibility of HA crystallization. By delaying the release of uncomplexed phosphate ions, however, reactions involving calcium ions and the Ti substrate would be initiated to form adhesive HA-Ti interfacial layers, such as $CaTiO_3$, that would enable film/substrate chemical bonding. Above 180 °C, complete TEP hydrolysis and free PO_4^{3-} would then enable the deposition of HA.

XRD, SEM, TEM, and EDX results confirmed the formation of a $CaTiO_3$ layer prior to TEP hydrolysis at 4 h synthesis time, validating the first half of the proposed hypothesis (Figures 3.1-3.4). A mechanism for the formation of $CaTiO_3$ on titanium substrates in high alkaline $Ca(EDTA)^{2-}$ solutions has been proposed previously by Fujishiro et al., which appears applicable to the work presented in this paper [41]:

(1) $Ca(EDTA)^{2-} \leftrightarrow Ca^{2+} + EDTA^{4-}$

(2) $Ti + H_2O + 2OH^- \rightarrow TiO_3^{2-} + 2H_2$

(3) $TiO_3^{2-} + Ca^{2+} \rightarrow CaTiO_3 + H_2O$

Figure 3.11a graphically displays this crystallization process. To determine if there was a thermodynamic basis for the observed result, thermodynamic process simulation software was utilized to create phase stability diagrams based on the reactants and reactant concentrations used in this study. Figures 3.12a and 3.12b display the computed phase stability diagrams for the $Ca(NO_3)_2$ – EDTA - TEP – KOH - H_2O system in the presence

of a titanium substrate at 50 and 180 °C, prior to complete TEP hydrolysis. The diagrams illustrate that titanium is not thermodynamically stable, leading to the formation of TiO_2 at lower pH, $CaTiO_3$ at higher pH, and a mixture of both at intermediate pH. The specific pH/[Ca^{2+}] point for the 0.232 molal $Ca(NO_3)_2$–0.232 molal EDTA–1.852 molal KOH-H_2O-Ti system at both respective temperatures is marked. At both 50 °C and 180 °C the pH/[Ca^{2+}] data point lies in a region where only $CaTiO_3$ is thermodynamically stable. The diagrams demonstrate that the observed formation of the Ti-HA chemical intermediate, $CaTiO_3$, can be explained by fundamental thermodynamics.

XRD and SEM results confirmed that after the hydrolysis of TEP at 4 h and 180 °C, hexagonal single crystals of Ca-P phase pure HA are deposited on the initial $CaTiO_3$ film, validating the remainder of the proposed hypothesis (Figures 3.5-3.6). The settling of homogeneously formed crystals onto the film surface is prohibited due to the placement of the sample in the reactor. HA nucleation must therefore occur heterogeneously on the substrate surface. Thus, calcium ions on the surface of $CaTiO_3$ grains, together with Ca^{2+} ions, PO_4^{3-} ions, and OH^- ions from the solution likely take part in nuclei formation in a three-step process, which chemically bonds the HA to $CaTiO_3$, as demonstrated below: (The *italics* Ca^{2+} in equation six represent calcium on the surface of the $CaTiO_3$ film)

(4) $Ca(EDTA)^{2-} \leftrightarrow Ca^{2+} + EDTA^{4-}$

(5) $(C_2H_5O)_3PO + 3H_2O \rightarrow 3C_2H_5OH + PO_4^{3-} + 3H^+$

(6) $_nCa^{2+} + {}_{10-n}Ca^{2+} + 6PO_4^{3-} + 2OH^- \rightarrow Ca_{10}(PO_4)_6(OH)_2$

Figure 3.11a graphically displays this crystallization process. In addition, Hung et al. have previously demonstrated that hydrothermally crystallized titanium perovskites

($ATiO_3$) have an A-site surface enrichment [64]. The occurrence of this phenomenon in the $CaTiO_3$ synthesized here would enrich the film surface with calcium ions and further enable the HA nucleation and $CaTiO_3$-HA bonding scheme proposed above. To determine if there was a thermodynamic basis for the observed result, thermodynamic process simulation software was again utilized. Figure 3.12c displays the computed phase stability diagrams for the $Ca(NO_3)_2$–EDTA–H_3PO_4–KOH-H_2O system in the presence of a titanium substrate at 180 °C, after complete TEP hydrolysis. The diagram illustrates a wide stability range for HA under these conditions. The specific pH/[Ca^{2+}] point for the 0.232 molal $Ca(NO_3)_2$–0.232 molal EDTA–0.187 molal H_3PO_4-1.852 molal KOH-H_2O system at 180 °C is marked. The diagram demonstrates that the observed formation Ca-P phase pure HA can be explained by fundamental thermodynamics. This is the first phase sequenced $CaTiO_3$/HA film deposition process reported in the hydrothermal HA literature.

Information regarding HA nucleation in this system may be inferred from SEM micrographs, which demonstrated an apparent extended nucleation period from 4 h to at least 8 h (Figure 3.6). Increasing solution pH has been concluded to slow the dissociation of the Ca-$EDTA^{2-}$ complex [36,38]. This controlled dissociation enables a solution to maintain a reservoir of Ca^{2+} ions in the form of Ca-$EDTA^{2-}$ that may be released over extended synthesis times. The extended release of Ca^{2+} then enables the heterogeneous supersaturation limit of HA to be breached continuously or intermittently, with respect to Ca^{2+}, over an extended period of time. Thus, the inferred extended nucleation period is

likely a result of heterogeneously precipitating HA from a homogeneous solution containing Ca-$EDTA^{2-}$ at a high pH (~10.5 – 11).

Multiple authors have reported that the length and/or aspect ratio of HA crystals formed in solution by non-stirred homogeneous precipitation using EDTA are a function of Ca^{2+} concentration, PO_4^{3-} concentration, EDTA/Ca ratio, temperature, and pH [44,45]. In general the trend is that crystal length/aspect ratio increases with an increase in each of these variables. Above certain PO_4^{3-} and Ca^{2+} concentrations and temperatures, the trend was reported to reverse, however. Fujishiro et al. attributed the PO_4^{3-} result to changes in HA solubility and the number of nuclei. Andes-Verges et al. attributed the Ca^{2+} and temperature result to the partial dependence of each variable on the other. Importantly, Fujishiro et al. studying a 0.1 M $Ca(NO_3)_2$–0.1 M $(EDTA)^{4-}$-0.3 M H_3PO_4 system at pH 8 (NH_4OH/HNO_3 adjusted) for 1 h with temperatures that varied from 150 °C to 225 °C did not see the crystal length/aspect ratio trend reversal that Andes-Verges et al. reports in a 0.05 M $Ca(NO_3)_2$–0.05 M Na_2(EDTA)-0.03 $(NH_4)_2HPO_4^{3-}$ system at pH 11 (NH_3 adjusted) for 1 h with temperatures that varied from 150 °C to 220 °C. Together these results indicates that Ca^{2+} concentration, PO_4^{3-} concentration, EDTA/Ca ratio, temperature, and pH do not strictly dictate crystal length/aspect ratio independently, but rather in concert. Consequently, it can be concluded that the observed formation of low aspect ratio crystals during the formation of the continuous film, 4 – 10 h, is a function of these reaction conditions. With the given literature, however, it does not appear possible to specifically determine why low aspect ratio crystals are formed during this period. A

comparison to other hydrothermal HA film crystallization processes is not possible either due to a lack of comparable data.

In a previous study it was demonstrated that this hydrothermal crystallization process enables the deposition of a passive film with [0001] crystallographic texture [62]. Passive film growth theory and data demonstrate that passive film formation occurs through the formation of a compact primary layer followed by growth of a porous secondary layer [60]. Upon formation of a continuous polycrystalline film (compact primary layer) thickening (secondary layer growth) occurs epitaxially on existing grains and preferentially in certain crystallographic directions resulting in crystallographic texturing that increases with film thickness [59]. Based on this information it was hypothesized that if the films synthesized here follow this growth mechanism, then the [0001] crystallographic orientation of the crystals on the surface of the film may be engineered through the control of synthesis time.

SEM results confirm the formation of an initial compact primary layer, illustrating that HA crystals nucleate and grow from 4 h until a continuous, passivating, film is formed sometime between 10 and 12 h (Figure 3.6, Figure 3.10). It has been suggested that a negatively charged surface is required to attract Ca^{2+} ions to a surface and then nucleate and grow HA in a manner that leads to the formation of a continuous passivating uniform film, as presented here [49,50]. The formation of a continuous $CaTiO_3$ film prior to HA crystallization and the availability of calcium atoms on the surface of the $CaTiO_3$ for HA nuclei formation, however, make this requirement unnecessary for this system. After 10

h, during film thickening (secondary layer growth), XRD, SEM, and pole figure results demonstrate a refinement of the orientation of hexagonal HA single crystals, such that the population fraction of crystals with their c-axis, or [0001] zone axis, orthogonal to the substrate increases (Figure 3.7-3.10). This result follows the typical model for polycrystalline film growth, after the formation of a continuous film [59] and confirms the hypothesis offered above. Figure 3.11c graphically demonstrates this film growth mechanism. The slow extended release of free Ca^{2+} in this system, which is attributed to the controlled dissociation of the Ca-$EDTA^{2+}$ complex in high pH solutions as discussed above and demonstrated in the extended nucleation period of HA observed in this study and by thermodynamic modeling of free Ca^{2+} concentration in a previous manuscript [62] means that crystal growth is unlikely to occur via Oswald ripening during the synthesis times studied in this manuscript. Thus, the HA film thickening process is concluded to occur by competitive growth in the [0001] HA crystallographic direction. As a result, this growth mechanism provides the opportunity to create HA films composed of hexagonal single crystals with engineered [0001] crystallographic orientation through control of synthesis time. One potential application of controllable crystallographic orientation includes engineering orientation to preferentially increase the surface area of specific HA crystallographic faces presented to the body, such as the bioactive $\{10\bar{1}0\}$ face that is displayed on the 6-equivalent faces of hexagonal crystals.

Conclusions

Utilization of the delayed-release phosphate source, TEP, enables the deposition of the Ti-HA chemical intermediate $CaTiO_3$ and HA in a single phase-sequenced process. The phase-sequenced process, which enables HA-Ti chemical bonding, is the first such

process reported in the hydrothermal HA literature. An examination of the film growth mechanism demonstrated that film thickening of hexagonal crystals occurs by means of competitive growth in the [0001] HA crystallographic direction, enabling [0001] crystallographic texture to be controlled with synthesis time. This method for controlling HA crystallographic orientation may have novel biological applications.

Acknowledgements

We gratefully acknowledge the research support by the Rutgers Center for Ceramic Research, the National Science Foundation/Rutgers IGERT on Biointerfaces, the Department of Education/Rutgers GAANN in Molecular, Cellular, and Nanosystems Bioengineering, the Rutgers University Graduate School New Brunswick, the New Jersey Center for Biomaterials, and the Rutgers University Roger G. Ackerman Fellowship. The authors wish to thank Valentin Starovoytov for critical point drying and sputter coating of biological samples.

Abbreviations

HA – Hydroxyapatite
PS-HA – Plasma sprayed hydroxyapatite
EDTA – Ethylenediamine-tetraacetic acid, $C_{10}H_{16}N_2O_8$
TEP - Triethyl phosphate, $C_6H_{15}O_4P$
XRD – X-Ray diffraction
FESEM – Field emission scanning electron microscopy
TEM – Transmission electron microscopy
EDX – Energy dispersive X-ray spectroscopy
FIB - Focused ion beam
PDF – Powder diffraction file
Ti6Al4V - Alloyed titanium with 6 wt.% aluminum and 4 wt.% vanadium

Captions for Figures

Figure 3.1 X-ray diffraction patterns of the Ti6Al4V substrate and films formed on Ti6Al4V substrates after hydrothermal treatment for 0 – 4 h: (a) 0 h, (b) 2 h, (c) 4 h.

Figure 3.2 SEM micrographs of the Ti6Al4V substrate and films formed on Ti6Al4V substrates after hydrothermal treatment for 0 – 4 h: (a) 0 h - Mag. x2000, (b) 2 h - Mag. X2000, (c) 2 h – Mag. x10,000, (d) 4 h - Mag. x2000, (e) 4 h – Mag. x10,000.

Figure 3.3 TEM micrographs and EDX maps of a cross-section of a film formed on a Ti6Al4V substrate by hydrothermal synthesis for 6 h: TEM micrographs - (a) Mag x28,100, (b) Mag. x59,400, EDX elemental maps - (c) Titanium, (d) Aluminum, (e) Vanadium, (f) Calcium, (g) Oxygen, (h) Phosphate, (i) Platinum.

Figure 3.4 Normalized EDX line-scan chemical data of a cross-section of a film formed on a Ti6Al4V substrate by hydrothermal synthesis for 6 h. The scan moves from above the deposited film, 0 nm, through the film, and to the bulk substrate, 1400 nm+. Background counts were subtracted at each position. See the experimental section for details.

Figure 3.5 X-ray diffraction patterns of the Ti6Al4V substrate and films formed on Ti6Al4V substrates after hydrothermal treatment for 6 – 10 h: (a) 6 h, (b) 8 h, (c) 10 h.

Figure 3.6 SEM micrographs of films after hydrothermal treatment for 6 – 10 h: (a) 6 h - Mag. x2000, (b) 6 h – Mag. x10,000, (c) 8 h - Mag. x1000, (d) 8 h – Mag. x10,000, (e) 8 h – Mag. x20,000, (f) 10 h - Mag. x1000, (g) 10 h - Mag. x5000.

Figure 3.7 X-ray diffraction patterns of the Ti6Al4V substrate and films formed on Ti6Al4V substrates after hydrothermal treatment for 12 – 24 h: (a) 12 h, (b) 14 h, (c) 24 h.

Figure 3.8 (0002) HA pole figures for films formed on Ti6Al4V substrates after hydrothermal treatment at multiple synthesis time points: (a) 8 h, (b) 10 h, (c) 14 h, (d) 24 h, (e) Legend. Intensity is normalized to the most intense Phi/Psi combination in each plot, varying from 0 – 1 arbitrary units.

Figure 3.9 (0002) HA pole figures for films formed on Ti6Al4V substrates after hydrothermal treatment at multiple synthesis time points in terms of MRD.

Figure 3.10 SEM micrographs of films formed on Ti6Al4V substrates after hydrothermal treatment for 10 – 24 h: (a) 12 h - Mag. x1000, (b) 14 h - Mag. x1000, (c) 24 h - Mag. x1000.

Figure 3.11 Proposed film growth process on Ti6Al4V substrates: (a) $CaTiO_3$ formation below 180 °C and from 0-4 h synthesis time, (b) Continuous HA film formation from 4-10 h synthesis time, (c) Competitive HA film thickening from 10 h on - square facetted

grains with a (111) fast growth direction are used to illustrate this process. Thickening of the initial 2D film leads to the termination of grains with (010), (100), and (001) texture by crystals with (111) texture. This occurs because the crystals with (111) texture are oriented to have their fast growth direction normal to and in the plane of the film, (d) Proposed concentration of Ca^{2+} with synthesis time relative to $CaTiO_3$ and HA solubility lines and heterogeneous nucleation supersaturation limits. Adapted from Fujishiro et al.[41], Thompson et al.[59], and Haders et al [58].

Figure 3.12 Calculated thermo-chemical phase equilibria diagrams for reaction solutions containing (a) 0.232 molal $Ca(NO_3)_2$-0.232 molal EDTA-1.852 molal KOH-H_2O at 50 °C. (b) 0.232 molal $Ca(NO_3)_2$-0.232 molal EDTA-1.852 molal KOH-H_2O at 180 °C, and (c) 0.232 molal $Ca(NO_3)_2$-0.232 molal EDTA-0.187 molal H_3PO_4-1.852 molal KOH-H_2O at 180 °C, all in the presence of Titanium. The black box represents the pH/[m Ca^{2+}] (m=molal) combination calculated for each system under these conditions. The initial room temperature pH of the starting slurries has been recalculated to the pH at the experimental temperature. From that point the pH has been titrated to higher and lower values.

Figures

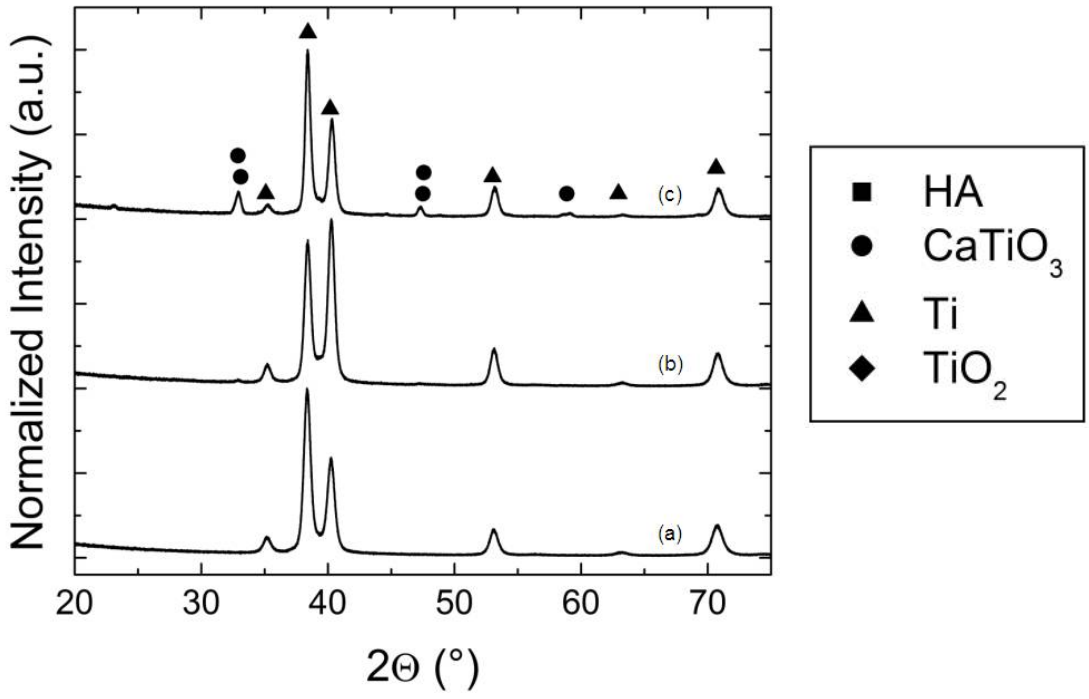

Figure 3.1

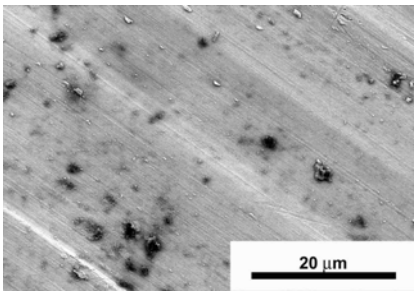

(a)

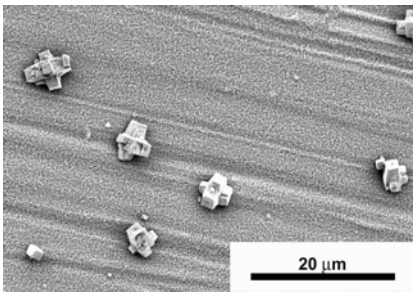

(b)

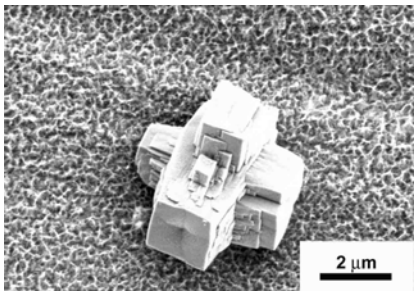

(c)

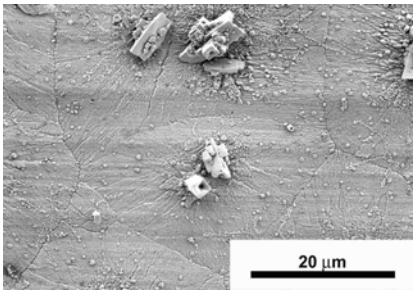

(d)

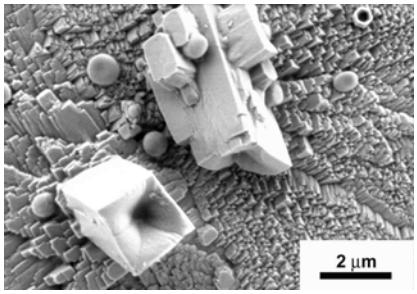

(e)

Figure 3.2

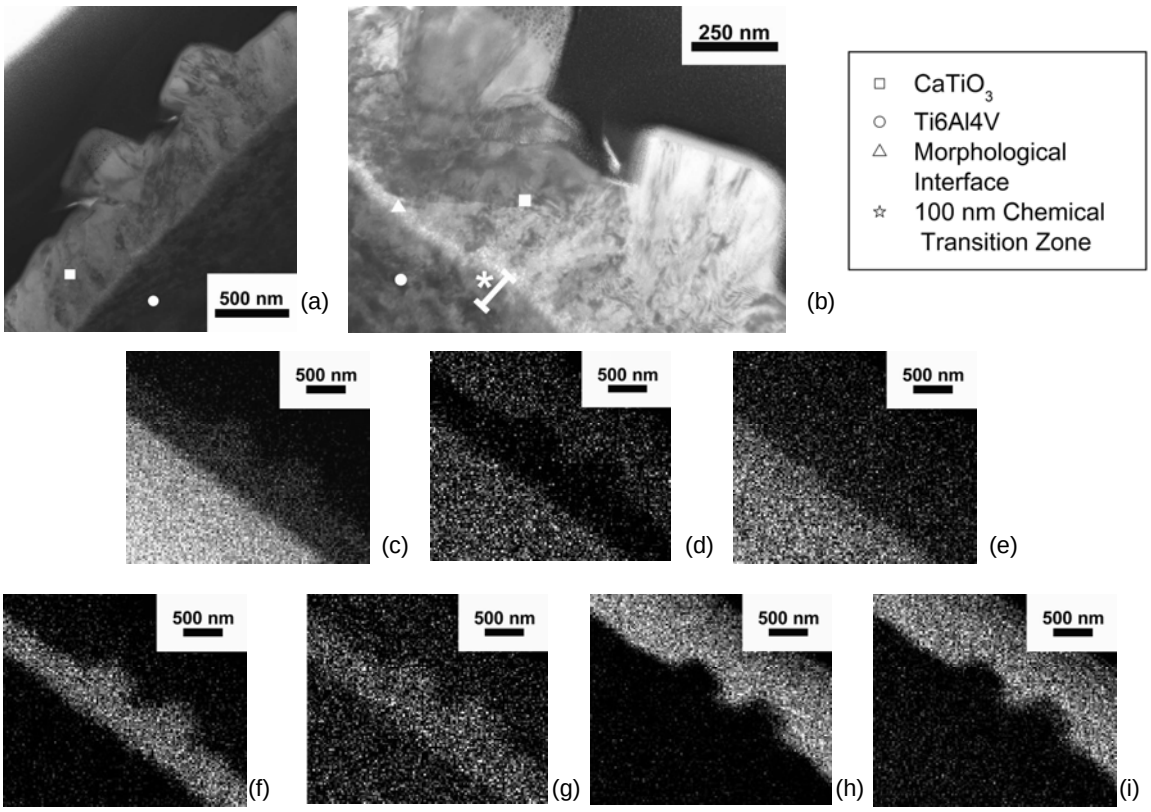
500 nm
(a)
250 nm
(b)
CaTiO3
Ti6Al4V
Morphological Interface
100 nm Chemical Transition Zone
500 nm
(c)
500 nm
(d)
500 nm
(e)
500 nm
(f)
500 nm
(g)
500 nm
(h)
500 nm
(i)

Figure 3.3

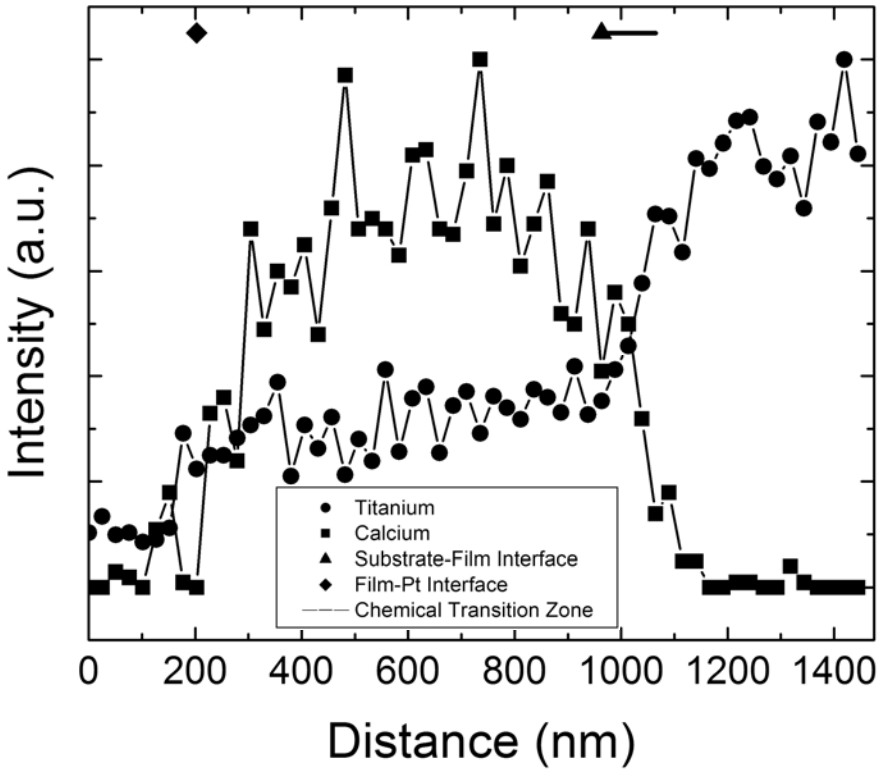
Intensity (a.u.)
Titanium
Calcium
Substrate-Film Interface
Film-Pt Interface
Chemical Transition Zone
0
200
400
600
800
1000
1200
1400
Distance (nm)

Figure 3.4

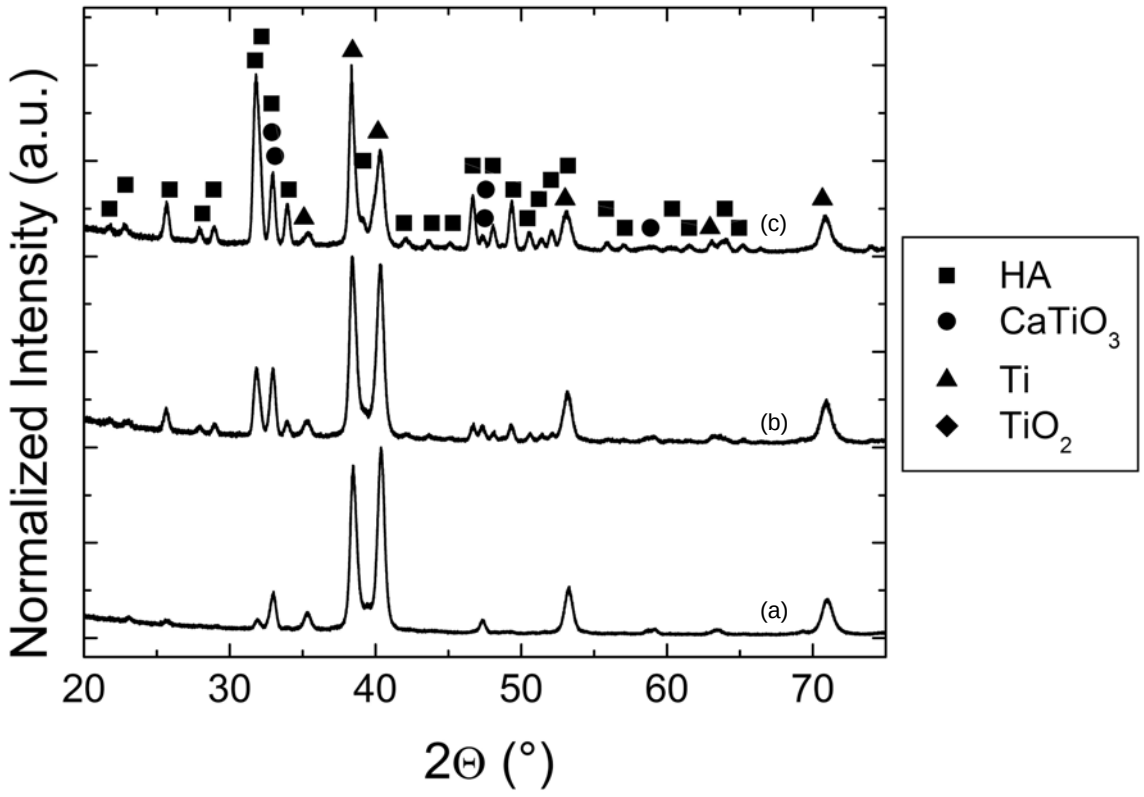
Normalized Intensity (a.u.)
20
30
40
50
60
70
2Θ (°)
(c)
(b)
(a)
HA
CaTiO3
Ti
TiO2

Figure 3.5

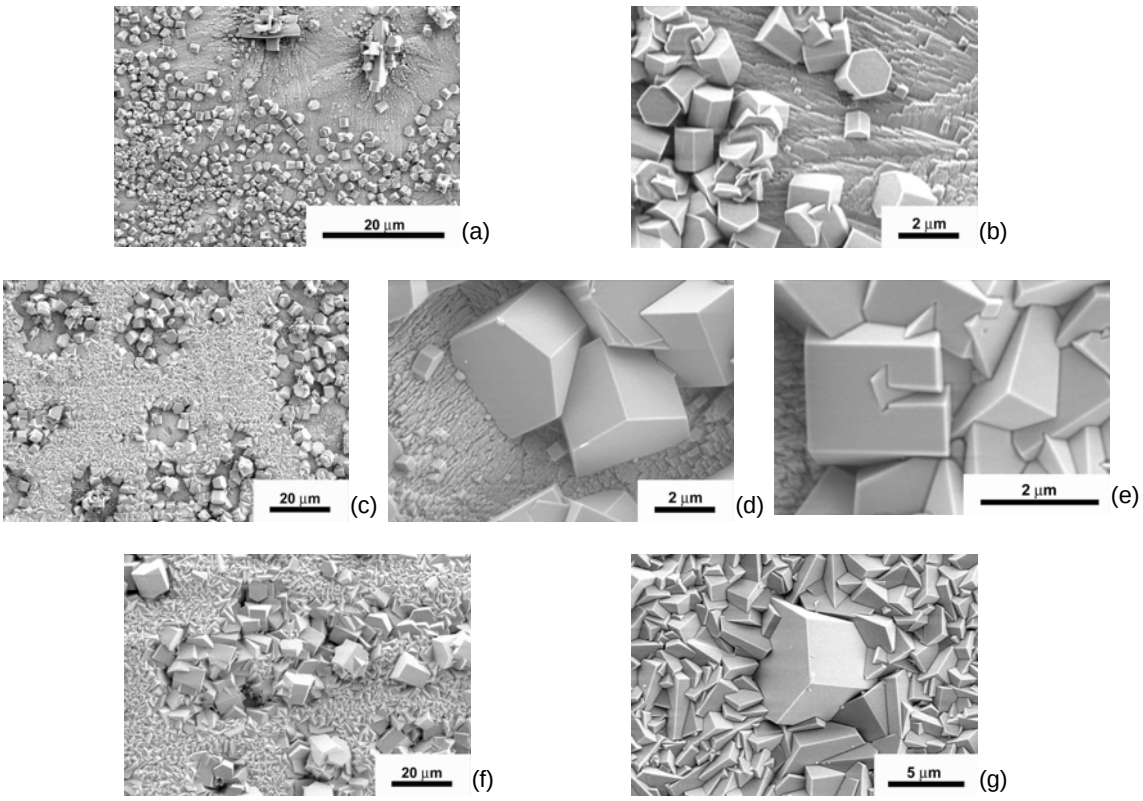

Figure 3.6

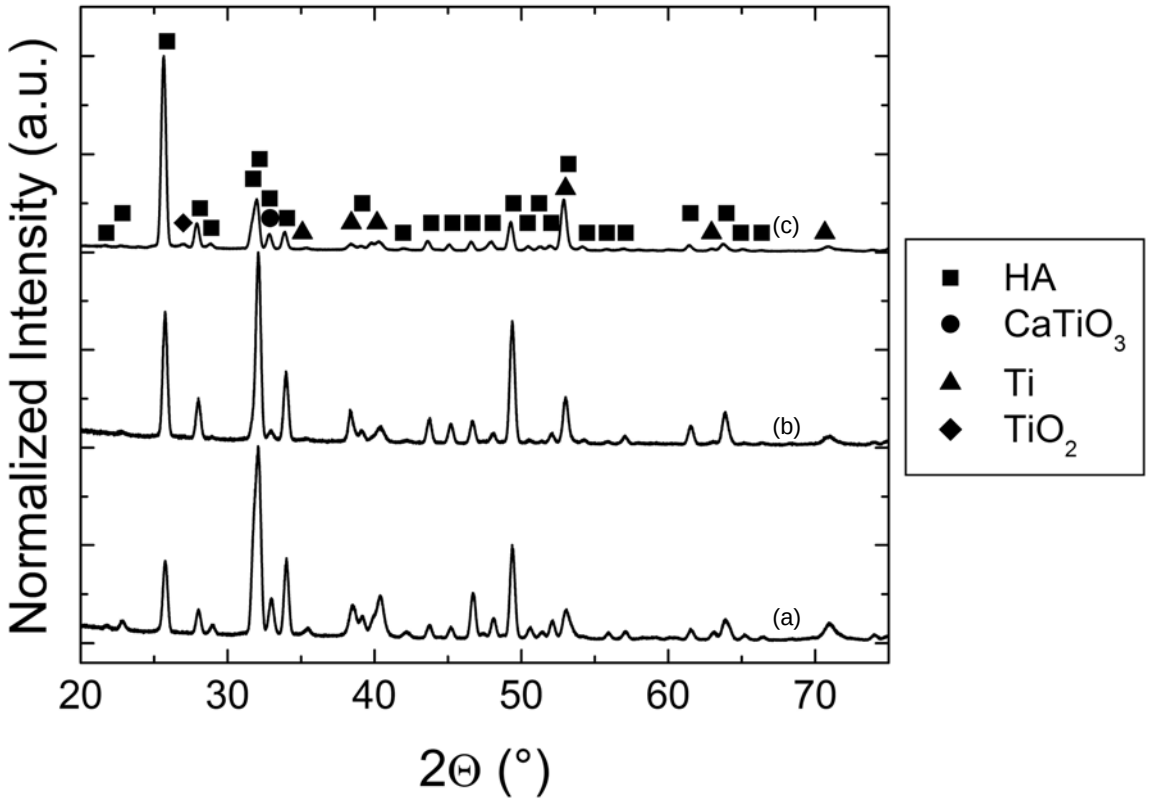
Normalized Intensity (a.u.)
20
30
40
50
60
70
2Θ (°)
(c)
(b)
(a)
HA
CaTiO3
Ti
TiO2

Figure 3.7

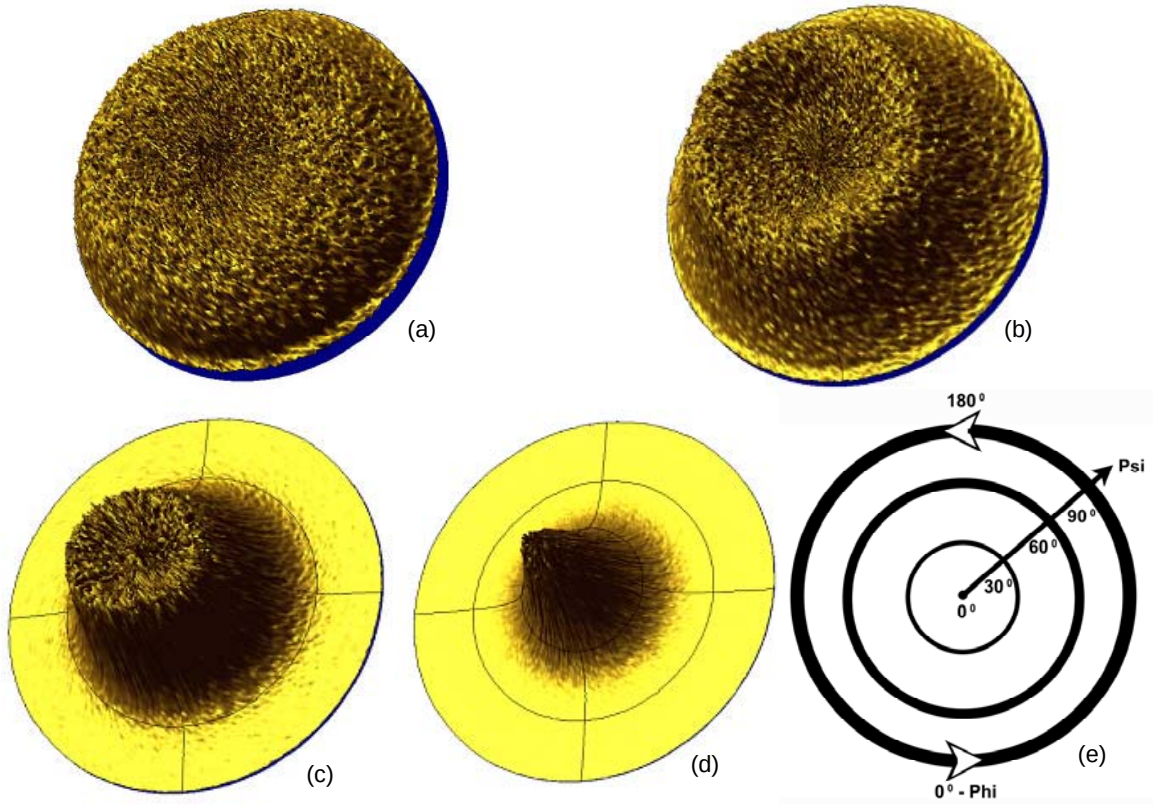

Figure 3.8

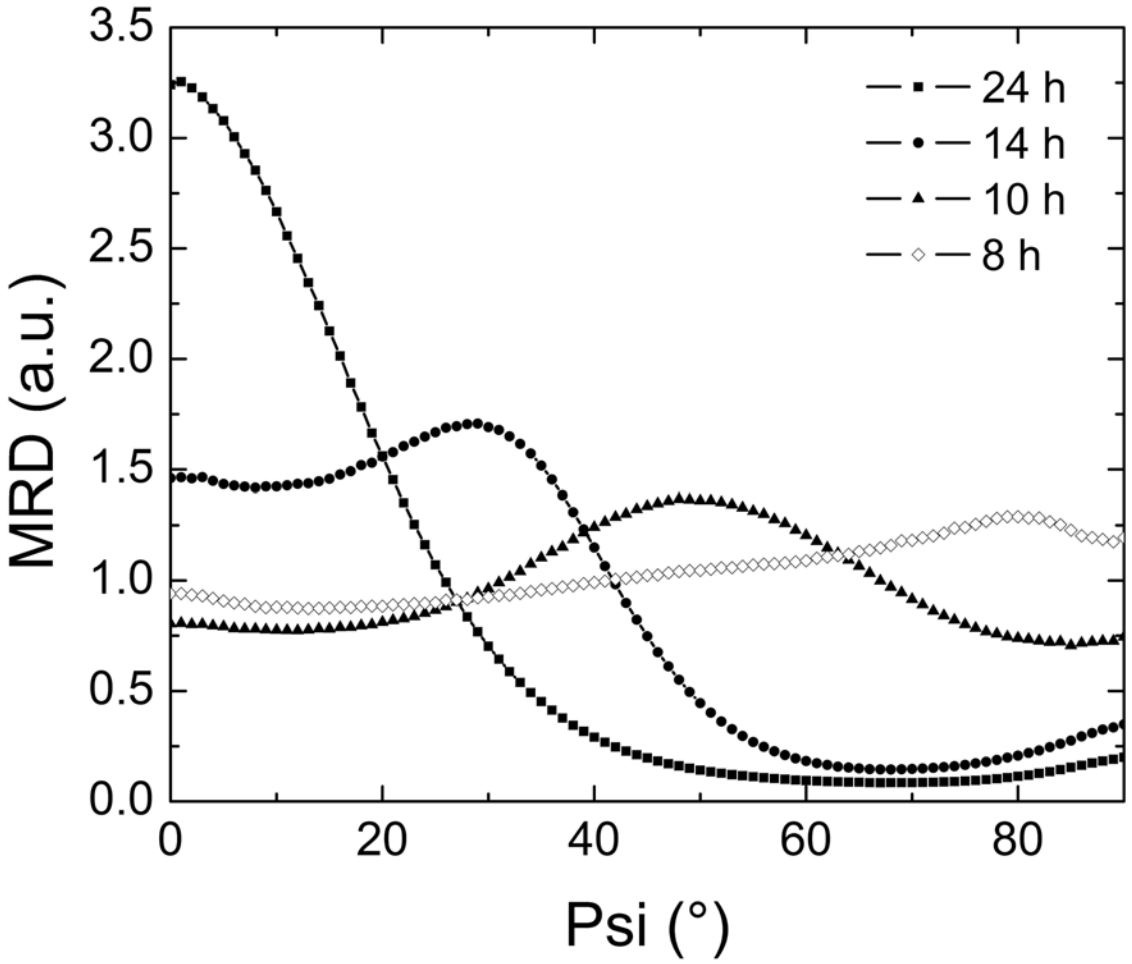

Figure 3.9

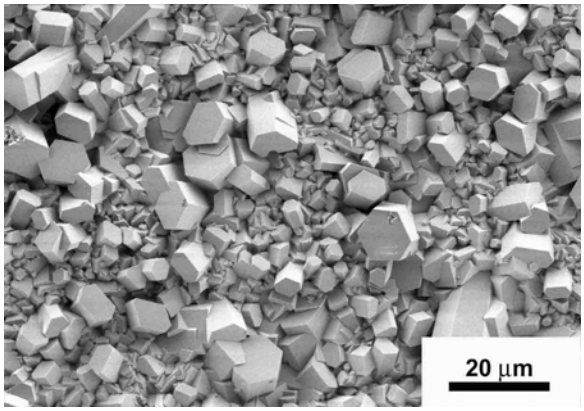

(a)

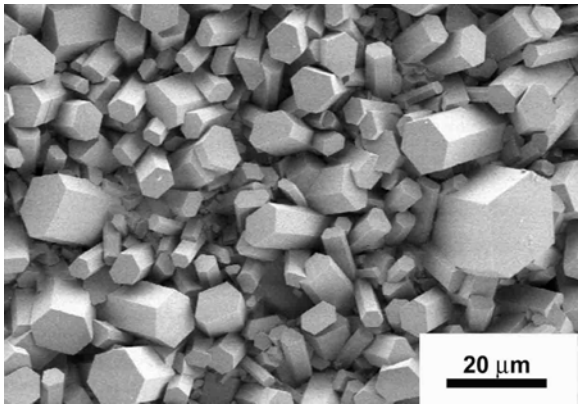

(b)

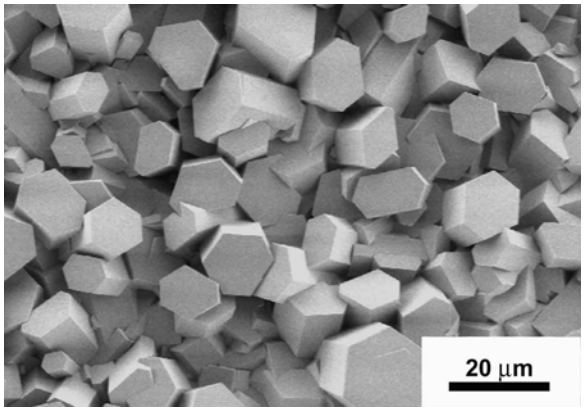

(c)

Figure 3.10

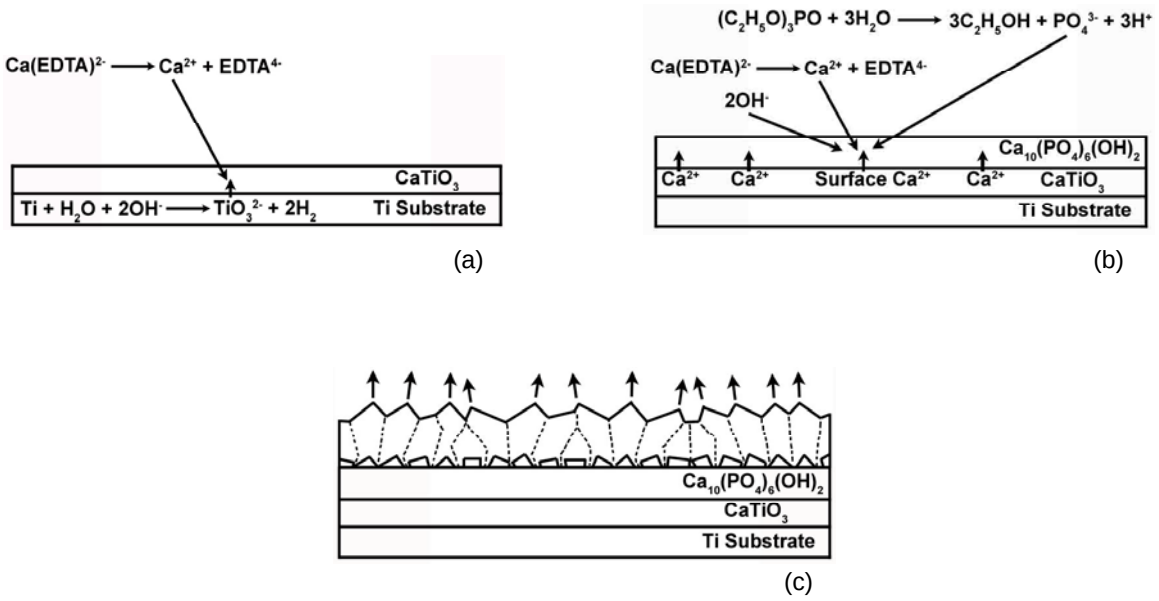
Ca(EDTA)2- → Ca2+ + EDTA4-
CaTiO3
Ti + H2O + 2OH- → TiO3 2- + 2H2
Ti Substrate
(a)
(C2H5O)3PO + 3H2O → 3C2H5OH + PO4 3- + 3H+
Ca(EDTA)2- → Ca2+ + EDTA4-
2OH-
Ca10(PO4)6(OH)2
Ca2+
Ca2+
Surface Ca2+
Ca2+
CaTiO3
Ti Substrate
(b)
Ca10(PO4)6(OH)2
CaTiO3
Ti Substrate
(c)

Figure 3.11

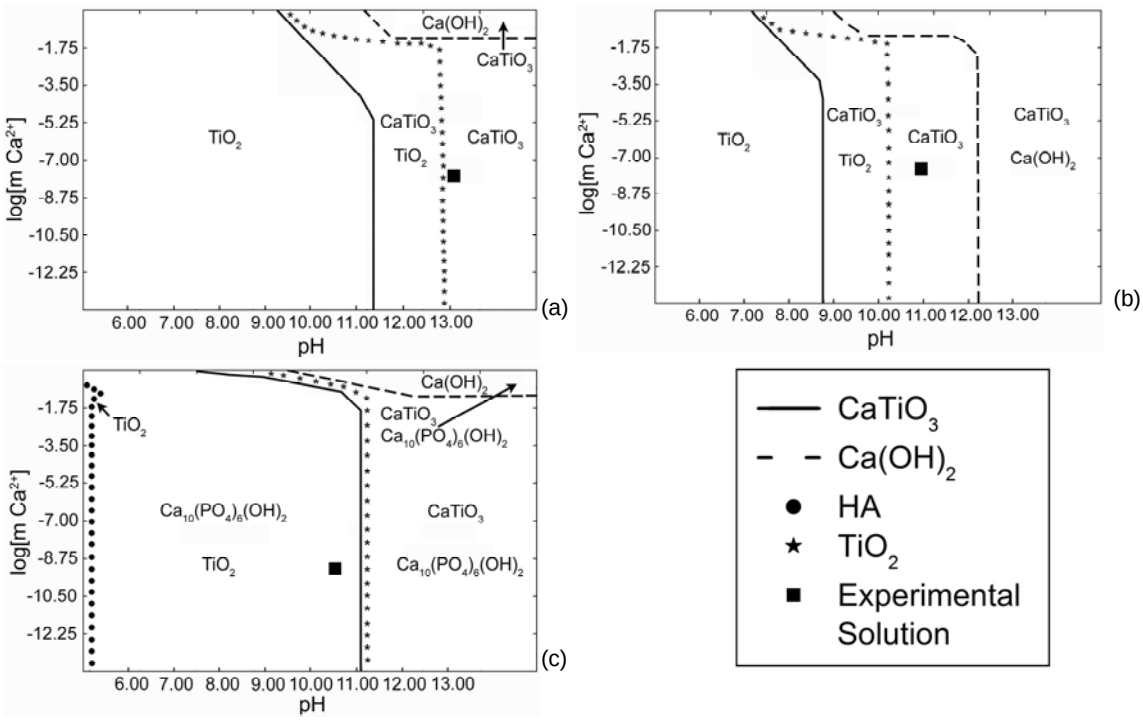
Ca(OH)2
CaTiO3
TiO2
CaTiO3
TiO2
CaTiO3
log[m Ca2+]
-1.75
-3.50
-5.25
-7.00
-8.75
-10.50
-12.25
6.00 7.00 8.00 9.00 10.00 11.00 12.00 13.00
pH
(a)
CaTiO3
TiO2
CaTiO3
Ca(OH)2
(b)
Ca(OH)2
TiO2
CaTiO3
Ca10(PO4)6(OH)2
Ca10(PO4)6(OH)2
CaTiO3
TiO2
Ca10(PO4)6(OH)2
(c)
CaTiO3
Ca(OH)2
HA
TiO2
Experimental Solution

Figure 3.12

Chapter 4

Crystallographically Engineered, Hydrothermally Crystallized Hydroxyapatite Films – an *In vitro* Study of Bioactivity

D.J. Haders[1,2], C.C. Kazanecki[3], A. Burukhin[1], D.T. Denhardt[3], R.E. Riman[1].

[1] Department of Material Science and Engineering, Rutgers, The State University of New Jersey, Piscataway, New Jersey

[2] Department of Biomedical Engineering, Rutgers, The State University of New Jersey, Piscataway, New Jersey

[3] Department of Cell Biology and Neuroscience, Rutgers, The State University of New Jersey, Piscataway, New Jersey

Abstract

The aim of this study was to evaluate the bioactivity of adhesive, passivating, hydroxyapatite (HA) films composed of hexagonal single crystals that display $\{10\bar{1}0\}$ and {0001} HA crystallographic faces. The effect of engineered [0001] crystallographic orientation (texture) on film bioactivity was investigated in parallel. Films were deposited by TEP/EDTA doubly regulated hydrothermal crystallization on Ti6Al4V substrates for 10, 14, and 24 h. The general bioactivity of HA films was investigated by analysis of MC3T3-E1 pre-osteoblast spreading using SEM and quantitative analysis of total cell metabolic activity (Alamar Blue™ assay) from 0 – 28 d. SEM and XRD were used to evaluate the ability of films to support the differentiation of MC3T3-E1 pre-osteoblasts into mature, matrix secreting, mineralizing osteoblasts. Substrates with known biocompatibility, namely tissue culture plastic (TCP), polished Ti6Al4V, and roughened

Ti6Al4V, were evaluated for comparison. Results demonstrated that all HA films enabled MC3T3-E1 cells to spread, grow, and differentiate into matrix secreting, mineralizing osteoblasts in a manner similar to HA films reported in the literature. Biomineral deposited on HA films could not be removed from the films after extraction of organic material by 6.15 vol% sodium hypochlorite. Differences in [0001] HA crystallographic orientation were not, however, found to significantly affect bioactivity. Based on these results, it is concluded that HA films synthesized by our process are non-toxic, bioactive, osteoconductive, and bone bonding. The demonstrated crystallinity, phase purity, passivation, and adhesion properties of these films taken together with these biological results indicate that they are candidates for use on clinical orthopedic implants. The lack of a relationship between reported HA crystallographic face specific protein absorption and bulk HA bioactivity are discussed in terms of crystallographic texture, surface roughness, assay robustness, and competitive protein absorption.

Introduction

Several types of coatings have been applied to commercial metallic orthopedic implants including sintered metallic beads, sintered metallic fiber meshes, plasma sprayed metal, and hydroxyapatite [7,11,65-67]. These coatings and others like them have been or are being developed to overcome limitations inherent in the classic cemented orthopedic implant developed by Charnley in 1958 [7,65]. The ceramic phase of bone, however, is a poorly crystalline, anion/cation-substituted, non-stoichiometric hydroxyapatite (HA), $Ca_{10}(PO_4)_6(OH)_2$ [1,2,52]. Consequently, due to its biocompatibility but poor mechanical properties, HA is considered the ideal material for non-load bearing hard tissue

replacement, and the ideal coating for load bearing metallic orthopedic implants [2-5]. Numerous reviews have described how HA-coated metallic orthopedic implants bridge larger gaps between the implant and bone with new bone tissue, accelerate bone apposition, enable more fixation in osteoporotic bone, and have increased bone-implant bond strength as compared with alternative orthopedic implant surfaces including sintered metallic porous coatings, plasma-sprayed titanium coatings, and roughened or untreated metallic implant surfaces [2,5,7-12].

Commercial hydroxyapatite films are most often applied to metallic substrates using the plasma spray method (PS-HA), which is a high temperature process that sprays molten hydroxyapatite particles onto the implant surface at high pressures [2,13,14]. Since the introduction of PS-HA coatings in the 1980's [2], however, concerns have been raised about the consequences of PS-HA's low crystallinity, lack of phase purity, passivation properties, and difficulty in coating substrates with complex geometry (line-of-sight-process) [2,4,12,13,16,17,19,22]. Critically, PS-HA films applied to the clinically relevant Ti6Al4V alloy (alloyed titanium with 6 wt.% aluminum and 4 wt.% vanadium) lack a Ti-HA chemical intermediate bonding layer such as $CaTiO_3$, and rely on mechanical interlock rather than chemical bonding to adhere the film to the substrate [16,19,61]. As a result, *in vivo* coating delamination has been reported due to the greater interfacial strength between HA and bone, than HA and titanium [6,10,15,20,21]. HA films deposited by other techniques including sol-gel, pulsed laser deposition, magnetron sputtering, ion-beam deposition, and biomimetic crystallization share all or some of PS-HA's limitations [3,28-32]. Consequently, there is a need to develop inexpensive reproducible next generation

HA film deposition techniques, which deposit chemically bonded, high crystallinity, phase pure, passivating, conformal HA films on clinically used substrates such as Ti6Al4V.

In two previous papers, we reported on the use of Triethyl Phosphate/ Ethylenediamine-tetraacetic acid (TEP/EDTA) doubly regulated hydrothermal crystallization to deposit HA films on metallic substrates [58,62]. Results demonstrated that highly crystalline, phase-pure, passivating HA films were formed on all examined substrates [58,62]. The utilization of the delayed-release phosphate source, TEP, enabled the deposition of $CaTiO_3$ and then HA in a single, phase-sequenced process on Ti substrates, the first process of its kind reported in the hydrothermal HA literature [58]. The process chemically bonded HA to Ti, which enabled a high film adhesion value to be obtained (5, ASTM D3359) [62]. It was also demonstrated that films were composed of hexagonal single crystals of HA, which display the $\{10\bar{1}0\}$ ($\{hkil\}$ – Equivalent hexagonal crystallographic plane Miller indices) crystallographic face on the 6 equivalent hexagonal faces and the {0001} face on the cap of the hexagonal rod. Importantly, molecular modeling and *in vitro* studies have shown that acidic bone proteins and other proteins found to bind HA with high affinity, bind to the $\{10\bar{1}0\}$ face [26,27]. Thus, it is hypothesized that the films reported here will demonstrate robust bioactivity due to the functionalization of the film surface with highly bioactive HA crystallographic faces, which together with previously reported material properties, including film-substrate chemical bonding, will make these films potential candidates for use on clinical Ti6Al4V orthopedic implants.

Previous work also demonstrated that the [0001] ([*uvtw*] – Hexagonal crystallographic direction), c-axis, crystallographic orientation (texture) of hexagonal single crystals of HA could be engineered through control of synthesis time [58]. By taking advantage of the ability to control crystal surfaces (faces) and crystallographic texture this film deposition process may enable a novel route to further functionalize the film surface with highly bioactive crystallographic faces. More specifically, engineering the orientation of hexagonal HA crystals may, together with aspect ratio and crystal spacing, enable the ratio of $\{10\bar{1}0\}/\{0001\}$ faces presented to the extracellular fluid to be altered, allowing modulation of HA protein adhesion, bioactivity, and potentially properties such as implant integration and healing time. For example, crystals that compose the 10 h film have an aspect ratio of approximately 1, no spacing between the crystals, and a nominally random [0001] orientation indicating that there is likely a nominally equal representation of $\{10\bar{1}0\}$ and $\{0001\}$ planes on the film surface. Crystals that compose the 24 h film have a larger aspect ratio, spacing between crystals, and a large volume fraction of crystals with their [0001] direction near $2\theta = 0\ ^\circ$ potentially creating a large $\{10\bar{1}0\}/\{0001\}$ ratio. In addition to the crystal face specific protein absorption data cited above, others have demonstrated that self-directed HA protein absorption and matrix formation from serum increases cell attachment and spreading as compared to HA surfaces functionalized with integrin binding (RGD) and proteoglycan binding peptides [68], indicating that HA contains all the surface functionalization cues necessary for efficient protein adhesion, initial matrix formation, and cell attachment within its own crystal structure. Thus, it is hypothesized that HA contains surface functionalization cues for protein adhesion, initial matrix formation, and cell attachment within its own crystal

structure, and that these cues may be accentuated by engineering both crystal morphology and crystallographic orientation.

Although it is not the focus of this paper, it is recognized that surface roughness is also an important cell biology variable for tailoring bioactivity. For example, surface roughness has been reported to effect the spreading, proliferation, and differentiation (alkaline phosphatase (ALP) activity, type I collagen production, and *Runx 2* gene expression) of pre-osteoblast cells on titanium substrates [69,70]. Previous studies from our laboratory demonstrate obvious differences in the surface roughness profiles of HA films with differing degrees of [0001] crystallographic orientation [58]. Thus, it is critical that any substrate-dependent changes in MC3T3-E1 behavior be evaluated in terms of both [0001] crystallographic orientation and substrate surface roughness.

This study examines the effect of crystal faces and crystal orientation on HA film bioactivity. Bioactivity is evaluated by observation of cell spreading and quantitative analysis of total cell metabolic activity on hydrothermally crystallized HA films deposited for 10, 14, and 24 h with differing degrees of [0001] crystallographic orientation. The ability of these adherent films to support the differentiation of pre-osteoblasts into matrix secreting, mineralizing osteoblasts is then evaluated.

Experimental

a. HA Film Synthesis and Ti6Al4V Substrate Preparation

Ti6Al4V was chosen as the metallic substrate for this study due to both its clinical use in load-bearing orthopedic applications, and results for HA films previously deposited by the method reported here, on this substrate [58,62]. Previous results from our laboratory demonstrate the crystallization of adhesive (5, ASTM D3359) chemically bonded films composed of hexagonal single crystals of HA that display $\{10\bar{1}0\}$ and {0001} HA crystallographic faces [58,62]. Results have also demonstrated that the [0001] crystallographic orientation of HA films may by engineered through control of synthesis time [58,62]. At 10 h the [0001] orientation of crystals is nominally random, at 24 h the volume fraction of crystals with their [0001] direction parallel to the sample surface is several multiples greater than expected for a randomly oriented sample, and at 14 h an intermediate [0001] texture is obtained. Thus, here, Ti6Al4V substrates (McMaster Carr, Dayton, NJ) were treated hydrothermally for 10, 14, and 24 h using the previously reported hydrothermal crystallization process [58,62] and used to investigate the bioactivity of chemically bonded HA films composed of hexagonal single crystals with engineered [0001] crystallographic texture.

Ti6Al4V was utilized as an internal standard for bioactivity testing due to its clinical use in load-bearing orthopedic applications. Both polished and roughened Ti6Al4V substrates were used so that differences in bioactivity could be interpreted in terms of surface roughness, irrespective of crystallographic orientation. Polished Ti6Al4V samples were the same as those used for HA film deposition. Roughened Ti6Al4V alloy substrates were formed by grit blasting polished Ti6Al4V samples using 35-100 Al_2O_3 media (McMaster Carr). Grit was removed by cleaning in an ultrasonic bath (FS30, Fisher

Scientific, Hampton, NH). All Ti6Al4V samples were then cleaned with detergent (Alconox, White Plains, NY), ethyl alcohol (Pharmco-AAPER, Brookfield, CT), and distilled water.

b. Film/Substrate Characterization

The surface roughness, Ra, of 10, 14, and 24 h HA films was measured by profilometry (scan length 500 μm, Dektak 3030, Veeco, Woodbury, NY). The average surface roughness of six measurements for each film type, and the standard deviation of the means were calculated. Polished Ti6Al4V and roughened Ti6Al4V substrates were characterized by profilometry in a previous study [62].

c. *In vitro* Cell Culture Work

MC3T3-E1 subclone 4, mouse calvaria-derived, pre-osteoblast cells [71] were used to study the biocompatibility of crystallographically tuned HA films synthesized for 10, 14, and 24 h on Ti6Al4V substrates; in addition to polished and roughened Ti6Al4V substrates, which were used as internal standards. Cells were cultured at 37 °C and 5 % CO_2 (Forma Scientific, Marietta, OH) in complete cell growth medium - α-Minimum Essential Medium (α-MEM) (Invitrogen Corp, Carlsbad, CA), 10% Fetal Bovine Serum (FBS) (Hyclone, Logan UT), 50 units/mL penicillin (Invitrogen Corp), 50 micrograms/mL streptomycin (Invitrogen Corp), and 1 mM glutamine (Invitrogen Corp) – prior to seeding onto samples. Specimens were sterilized by autoclaving for 20 min with a 10 min dry cycle (Consolidated Stills and Sterilizers, Boston, MA), and placed in individual wells of a 6-well tissue culture plate (Falcon, Becton Dickinson and Company, Franklin Lakes, NJ) under sterile conditions for all studies. Cells were then seeded onto specimens at the densities noted below in cell growth medium and incubated. Tissue culture plastic

(TCP) was used as a control for all studies. For some experiments, cells were switched to complete induction medium - α-MEM (Invitrogen Corp), 10% FBS (Hyclone), 50 units/mL penicillin (Invitrogen Corp), 50 μg/mL streptomycin (Invitrogen Corp), 1 mM glutamine (Invitrogen Corp), 50 μg/mL ascorbic acid (Sigma-Aldrich, St. Louis, MO), and 10 mM β-glycerolphosphate (Sigma-Aldrich) - at the indicated times.

c1. Cell Spreading

The general bioactivity of substrates was evaluated, in terms of cell spreading, by seeding MC3T3-E1 subclone 4 passage 17 cells onto TCP, polished Ti6Al4V, roughened Ti6Al4V, and HA films synthesized on polished Ti6Al4V for 10, 14, and 24 h at a density of $1 \bullet 10^4$ cells/cm^2 in complete cell growth medium, and allowing them to attach and spread for 3 d. Cells were then fixed by incubating in cold 2% glutaraldehyde (Fisher Scientific) in phosphate-buffered saline (PBS) for 2 h, washed twice in PBS (15 min each), rinsed twice with distilled water (10 min each), and dehydrated by incubating in 50, 70, 80, 95, 100, and 100 vol% ethanol (Pharmco-AAPER) for 15 min each. Samples were then critical point dried (CPD 020, OC Oerlikon Balzers AG, Balzers, Liechtenstein), sputter coated with a conducting ~25 nm Au/Pd film (SCD 004, OC Oerlikon Balzers AG), and observed by Field emission scanning electron microscopy (FESEM, Model DSM 962 Gemini, Carl Zeiss, Oberkochen, Germany).

c2. Cell Metabolic Activity – Alamar Blue™ Assay

The ability of substrates to support osteoblast cell growth, in terms of total cell metabolic activity, was evaluated by seeding MC3T3-E1 subclone 4 passage 15 cells onto TCP, polished Ti6Al4V, roughened Ti6Al4V, and HA films synthesized on polished Ti6Al4V for 10, 14, and 24 h at a density of $1 \bullet 10^4$ cells/cm^2 in complete cell growth medium, and

incubating. All samples were studied in triplicate. Cells were allowed to attach for 1 d after which polished Ti6Al4V, roughened Ti6Al4V, and 10, 14, and 24 h HA film samples were moved to wells in new 6-well plates containing fresh complete cell growth medium under sterile conditions. This was done to eliminate cells from assay measurements that were attached to the tissue culture plastic rather than the samples. For consistency, complete cell growth medium was changed on TCP wells at this time. Triplicate blank wells containing only complete growth medium were also added at this time. This point was considered 0 d.

Alamar Blue™ (BioSource International, Camarillo, CA) is a vital dye that is taken up by cells and reduced from a non-fluorescent state to a fluorescent state by metabolic intermediates. At the following intervals, 0, 1, 3, 5, 8, 13, 15, 17, 20, 24, and 28 d, it was added to each culture well to a final concentration of 10%. After 2 h, 3-250 μL replicate aliquots were taken from each well and placed in a 96-well plate. Fluorescence was measured by exiting at 530 nm and measuring emission at 590 nm using a fluorometer (FluoroCount, Packard Instrument Co., Meriden CT). After each measurement, or every 2-3 d, the cell growth medium was removed, samples/wells were rinsed in PBS and fresh complete induction medium was added.

Data were expressed as a fraction of cell activity on the TCP control using the following equation:

$$(1)\ \alpha = \frac{S_i - B_i}{C_i - B_i}$$

where S_i is sample fluorescence intensity, C_i is TCP/control fluorescence intensity, B_i is blank/background fluorescence intensity, and α is cell activity as a fraction of control. The average cell activity for each sample type and the standard deviation of the means were calculated. To determine if differences in cell activity between sample groups at each time point were statistically significant ($p < 0.05$) a One Way ANOVA was calculated (Excel 2000, Microsoft, Redmond, WA) followed by a Tukey's Honest Significant Difference (HSD) post-test [72].

c3. Cell Differentiation – Extracellular Matrix Formation

The ability of substrates to support osteoblast cell differentiation in terms of extracellular matrix formation was evaluated by seeding MC3T3-E1 subclone 4 passage 15 cells onto TCP, polished Ti6Al4V, roughened Ti6Al4V, and HA films synthesized on polished Ti6Al4V for 10, 14, and 24 h at a density of $1 \bullet 10^4$ cells/cm^2 in complete cell growth medium, and incubating. After 1 d the cell growth medium was changed to complete induction medium. The medium was then changed every 2-3 d. After 105 d (15 weeks) samples were fixed, dehydrated, critical point dried, and sputter coated, as above, and then observed by FESEM (DSM 982 Gemini, Carl Zeiss).

c4. Cell Differentiation – Mineralization

The ability of substrates to support osteoblast cell differentiation, in terms of biomineralization, was evaluated by seeding MC3T3-E1 subclone 4 passage 15 cells onto TCP, polished Ti6Al4V, roughened Ti6Al4V, and HA films synthesized on polished Ti6Al4V for 10, 14, and 24 h at a density of $1 \bullet 10^4$ cells/cm^2 in complete cell growth medium and incubating. After 1 d, the medium was changed to complete induction medium. The medium was changed every 2-3 d. After 98 d (14 weeks) samples were

removed from the incubator and washed twice in PBS. Organic cell layers were then extracted by adding 6.15 vol% sodium hypochlorite (Ultra Clorox Bleach, The Clorox Company, Oakland, C.A.) to each sample well, and placing the culture plate in an 85 °C water bath for 2 h as previously described [73]. The liquid/mineral suspension was removed from each well, and placed in a conical. Each well/sample was then rinsed twice in distilled water, and this was also added to the corresponding conical. Mineral suspensions were then centrifuged for 3 min at 210 x g in a clinical centrifuge (International Equipment Company, Nashville, T.N.). The supernatant was removed, 10 mL of fresh distilled water was added, and samples were centrifuged again. This process was repeated 3 times. All supernatant except ~250 μL was then removed. The remaining solution was then pipetted to re-create a biomineral suspension. The suspension was removed and added drop-wise onto a glass slide, creating as small of a footprint as possible. The glass slides were then dried at 70 °C for 1-2 h. The resulting powder biomineral samples were then examined by X-ray diffraction (XRD) (step size = 0.02 °, 4 step/sec, 45 KV, 40 mA, Ni-filtered CuK_{α} radiation, parallel beam optics, Philips Hi-Resolution X'PERT X-Ray Diffractometer, PANalytical B.V., Almelo, Netherlands) and FESEM (DSM 982 Gemini, Carl Zeiss). Experimental XRD patterns were matched to patterns in the Powder Diffraction File (PDF, ICDD, Newtown Square, PA) database using Jade 8.0 software (MDI, Livermore, CA). The substrates (polished Ti6Al4V, roughened Ti6Al4V, and 10, 14, and 24 h HA films) were also dried at 70 °C for 1-2 h and then examined by FESEM (DSM 982 Gemini, Carl Zeiss).

Results

a. Substrate Characterization

Polished Ti6Al4V (P-Ti6Al4V), roughened Ti6Al4V (R-Ti6Al4V), and HA films hydrothermally synthesized on polished Ti6Al4V for 10, 14, and 24 h have been extensively characterized previously [58,62]. Surface roughness, Ra, results for 10, 14, and 24 h HA samples obtained in this study are reported in Table 4.1 along with previously reported values for P-Ti6Al4V and R-Ti6Al4V. Results demonstrate an increase in surface roughness with synthesis time, and average values that fall between that of P-Ti6Al4V (Ra = 414 nm) and R-Ti6Al4V (Ra = 3569 nm). Surface roughness is an important cell biology variable and has been reported to affect the spreading, proliferation, and differentiation (alkaline phosphatase (ALP) activity, type I collagen production, and *Runx 2* gene expression) of pre-osteoblast cells on titanium substrates [69,70]. Based on this information, it is concluded that differences in MC3T3-E1 behavior are possible in this study due differences in substrate surface roughness.

b. Cell Spreading

General substrate bioactivity was evaluated by observation of cell spreading on P-Ti6Al4V, R-Ti6Al4V, and 10, 14, and 24 h HA films (Figure 4.1). The cell spreading assay is a qualitative assay that evaluates the general bioactivity of a surface. Cells in contact with toxic surfaces minimize their surface area that is in contact with those surfaces, while cells in contact with bioactive surfaces maximize their surface area. Figure 4.1 displays MC3T3-E1 subclone 4 pre-osteoblast cells on substrates after 3 d in culture. In general, it is observed that cells are attached and spread on all substrates, such that they are extended more than 40 μm in their longest direction. This result is comparable to MC3T3-E1 cell spreading on HA films reported elsewhere [74]. From these

results it is concluded both that all substrates are non-toxic and biocompatible and that the HA films reported here display results similar to those reported in the HA literature.

For Ti6Al4V substrates, a difference in average surface roughness of ~3 μm is observed to significantly affect MC3T3-E1 cell spreading. Cell spreading on P-Ti6Al4V (Ra = 414 nm) is 2-dimensional. Spreading is directed along and within the polishing grooves on the substrate. This observation agrees with reports of contact guidance reported previously for MC3T3-E1 cells on grooved Ti6Al4V substrates [75]. On the other hand, cell spreading on R-Ti6Al4V (Ra = 3569 nm) is observed to be 3-dimensional. Spreading occurs over and around surface features of different heights with cell filopodia and cell bodies that bridge gaps from one surface feature to the next. It is also observed that the aspect ratio of cells is affected by surface roughness. Cells on polished Ti6Al4V fill the entire width of the grooves and have aspect ratios of ~1-2 as compared to cells on R-Ti6Al4V, which have aspect ratios of ~5. Differences in neither average surface roughness (~1.9 μm) nor [0001] crystallographic orientation were found to have a significant affect on cell spreading on HA films, however. Cells on all HA samples demonstrated spreading patterns similar to that seen on R-Ti6AL4V. Interestingly, 10, 14, and 24 h samples like the R-Ti6Al4V sample have micron scale surface roughness, as compared to the nanometer scale surface roughness of P-Ti6Al4V sample. From this result it may be concluded that changes in substrate surface roughness from the nanometer scale (P-Ti6Al4V) to the micron scale (R-Ti6Al4V, 10 h, 14 h, 24 h) affects MC3T3-E1 cell spreading patterns in the same general manner on these substrates, regardless of substrate chemistry or [0001] crystallographic orientation. Differences in micron scale roughness

between HA samples or between HA and the R-Ti6Al4V sample do not lead to a measurable effect on cell spreading.

c. Metabolic Activity

The ability of P-Ti6Al4V, R-Ti6Al4V, and 10, 14, and 24 h HA films to support the growth of cell cultures was measured in terms of total metabolic activity using the Alamar Blue™ assay. Figure 4.2 displays the metabolic activity profiles of MC3T3-E1 subclone 4 cell cultures from 0-28 d as a fraction of TCP controls. All substrates demonstrate a significant, multi-fold increase in metabolic activity from day 0 to their peak at day 15 or day 17. After this time, total metabolic activity levels stagnate and decline due to the formation of confluent cell layers. In reference to the HA literature, cell activity as a fraction of control at day 0, 1, and 3 on all HA substrates is comparable to the best performing HA films reported by Ball et al. at day 2, using the same assay [76]. The increase in non-normalized cell activity is 3-4 fold from day 3 to day 13 (data not shown), as compared to a single fold increase in the same parameter for the best performing HA films reported by Thian et al. between day 3 and day 14, using the same assay [77]. Thus, it is concluded both that all substrates support the growth of MC3T3-E1 culture total metabolic activity, and consequently cell number, and that the HA films reported here display results equal to or better than those reported in the HA literature.

For Ti6Al4V substrates, a difference in average surface roughness of ~3 μm is observed to significantly ($p = 0.05$) affect total metabolic activity at day 1. Differences in metabolic activity are statistically insignificant at all other time points. These results are not unexpected. Reduced rates of cell proliferation and reduced cell number have been

reported previously and attributed to increasing surface roughness on Ti6Al4V substrates for MC3T3-E1 and MG63 osteoblast like cells, respectively, at early culture time points [69,70]. Differences in neither average surface roughness (~1.9 μm) nor [0001] crystallographic orientation were found to have a significant ($p = 0.05$) affect on MC3T3-E1 metabolic activity on HA films, however. This is unexpected at least in terms of surface roughness based upon the work of Kim et al., which demonstrated significant differences in cell proliferation between Ti surfaces with surface roughness values similar to the HA films reported here, ~1-3 μm [70]. In general, however, metabolic activity patterns on all HA samples were similar to that seen on R-Ti6AL4V. All HA films demonstrated significantly ($p = 0.05$) lower total metabolic activity levels on day 1 as compared to cells on P-Ti6Al4V. The 24-h film had significantly lower metabolic activity levels on day 3 as well. Thus, it is concluded that changes in substrate surface roughness from the nanometer scale (P-Ti6Al4V) to the micron scale (R-Ti6Al4V, 10 h, 14 h, 24 h) affects MC3T3-E1 culture total metabolic activity patterns in the same general manner on these substrates, regardless of substrate chemistry or [0001] crystallographic orientation. Differences in micron scale roughness between HA samples or between HA and the R-Ti6Al4V sample do not lead to a measurable effect on total metabolic activity.

d. Cell Differentiation – Extracellular Matrix

The ability of substrates to support the differentiation of MC3T3-E1 subclone 4 pre-osteoblasts into mature, matrix-secreting osteoblasts was evaluated by culturing cells for 105 d on each substrate. Scanning electron micrographs of the surface of TCP, P-Ti6Al4V, R-Ti6Al4V, and 10, 14, and 24 h HA films after 105 d in culture are displayed

in Figure 4.3. All micrographs demonstrate the formation of an extensive extracellular matrix that completely covers and obscures the topology of the underlying substrate. The only observable substrate features are “shadows” of hexagonal HA crystals under the surface of the extracellular matrix formed on the 24 h sample. Thus, it may be concluded that all substrates support the differentiation of MC3T3-E1 subclone 4 pre-osteoblasts into mature, matrix-secreting osteoblasts. No difference in extracellular matrix formation was observed in terms of [0001] crystallographic orientation on HA substrates, or in terms of surface roughness on HA and Ti6Al4V substrates.

e. Cell Differentiation – Mineralization

The ability of substrates to support the differentiation of MC3T3-E1 subclone 4 pre-osteoblasts into fully differentiated, mineralizing osteoblasts was evaluated by culturing cells for 98 d on each substrate, chemically removing the cell/ECM layer (6.15 vol% sodium hypochlorite), and pelleting the non-solubilized mineralized portion of the matrix. Figure 4.4 and Figure 4.5 display X-ray diffraction patterns and SEM micrographs of the mineralized portion of the extracellular matrix isolated from TCP, P-Ti6Al4V, and R-Ti6Al4V substrates. No measurable amount of biomineral was isolated from the cell layers extracted from HA films. All observed peaks in the XRD patterns correspond to HA diffraction peaks reported in the Powder Diffraction File (PDF). Patterns are similar to those reported in the literature for *in vitro* biomineral deposited in MC3T3-E1 and fresh rat marrow cell cultures, and rat cortical bone [73,78]. The large background hump below $2\theta = 30\ ^\circ$ has been attributed to residual extracellular matrix [78]. Scanning electron micrographs of the biomineral on all substrates display a fibrous structure, which reflects the structure of the extracellular matrix that was deposited and subsequently mineralized.

All the various microstructures observed in Figure 4.5 were observed for all substrates. Thus, it may be concluded that TCP, P-Ti6Al4V, and R-Ti6Al4V substrates all support the differentiation of pre-osteoblasts cultures into fully differentiated, mineralizing osteoblasts as reported extensively elsewhere.

No mineral was isolated from cell layers extracted from HA films. Consequently, the ability of the HA films reported here to support the differentiation of MC3T3-E1 subclone 4 pre-osteoblasts into fully differentiated, mineralizing osteoblasts is unclear from the data reported above. To further evaluate differentiation the surface of each substrate was examined after chemical removal of the cell/ECM layer. SEM analysis of HA substrates revealed the presence of inorganic nodules on the surface of each HA film (Figure 4.6). SEM analysis of polished and roughened Ti6Al4V substrates did not, however, reveal inorganic nodules confirming that this was a HA-film-specific phenomenon (data not shown). This nodular inorganic phase is similar to biomineralized HA deposited *in vitro* and *in vivo* on HA films observed by others [79-82]. The nodules do not appear to have a preferential epitaxial relationship with the two populations of crystallographic faces provided by the film. Nodules appear to be adhered to both $\{10\bar{1}0\}$ (6 equivalent hexagonal faces) and {0001} (2 equivalent faces that cap the hexagonal rod) crystallographic faces. It is concluded then that 10, 14, and 24 h HA films support the differentiation of MC3T3-E1 pre-osteoblast into fully differentiated, mineralizing osteoblasts. Because the deposited mineral is associated with the HA film and cannot be removed by chemical means, it may also be concluded that there is a direct chemical bond between the HA film and the biomineral. Interestingly, other HA films

that are reported to be bone bonding have not necessarily had the biomineral-HA film bond challenged by chemical attack [80-82]. Thus, these hydrothermally synthesized HA films are concluded to be bone bonding and osteoconductive in addition to bioactive.

Discussion

In a previous study, SEM analysis of the internal angles between adjacent equivalent faces of hexagonal grains and the application of Steno's Law demonstrated that the films reported here were composed of hexagonal single crystals of HA [58]. Importantly, molecular modeling and *in vitro* studies have shown that a number of acidic bone proteins and other proteins found to bind HA with high affinity, bind to the $\{10\bar{1}0\}$ crystallographic face of HA, which is prominently displayed on the six equivalent faces of hexagonal single crystals [26,27]. Previous results also demonstrated that these films are high crystallinity, Ca-P phase pure, passivating, and chemically bonded to titanium substrates [58,62]. Thus, it was hypothesized that the films reported here would demonstrate robust bioactivity due to the functionalization of the film surface with highly bioactive HA crystallographic faces, which together with material properties, including film-substrate chemical bonding, would make these films potential candidates for use on clinical orthopedic implants such as Ti6Al4V.

Analysis of MC3T3-E1 subclone 4 pre-osteoblast spreading, metabolic activity (Alamar Blue™ assay), and differentiation confirmed this hypothesis. Hydrothermally synthesized HA films reported here were found to be non-toxic, bioactive, osteoconductive, and bone bonding at levels comparable to the highest performing HA films reported elsewhere

[74,76,77,79-82]. The bone-bonding characteristic of these films is particularly interesting. In review of the literature, Ducheyne et al. reported that bone bonding is the combined result of physiochemical processes including dissolution, precipitation, and ion-exchange, protein adsorption and cellular processes, which occur primarily as a result of physiochemical processes [83]. Davies et al. have reasoned, however, that independent cell-mediated formation of cement lines – a mineralized collagen free matrix that serves as an interface between new and old bone - together with physiochemical processes enabled bone bonding in a material dependent fashion [81]. Data from de Bruijin et al. support this claim demonstrating mineralized glycosaminoglycan (GAG)-positive layers of increasing size and decreasing GAG density at the film-ECM interface of HA films with decreasing crystallinity [80]. Epitaxial growth of biomineral on the HA film surface has also been cited as a potential bone bonding mechanism [79,80]. The films reported in this study are highly crystalline (99 %+) [62] and do not demonstrate surface pitting due to dissolution after 98 d in cell culture in SEM micrographs. Findings from preliminary, dissolution studies in protein free physiological solution confirm this result, reporting the release of only 0.17 ppm of Ca^{2+} (Atomic Absorption Spectroscopy, model 4000, Perkin Elmer, Waltham, MA) from the films and into solution and no surface pitting after 1-month. Therefore, dissolution and precipitation do not likely play a large role in bone bonding here. Bone bonding on these films then is likely due to one or a combination of cellular processes and epitaxy. Irrespective of bonding mechanism, the biological properties of these HA films in combination with previously described crystallinity, phase, adhesion, and passivation characteristics, suggest that these films are excellent candidates for use as coatings on Ti6Al4V orthopedic implants.

Previous work also demonstrated that the [0001], c-axis, crystallographic orientation (texture) of hexagonal single crystals of HA could be engineered through control of synthesis time [58]. By taking advantage of the ability to control the crystal surfaces (faces) presented to the extracellular medium through control of crystallographic texture, and based on $\{10\bar{1}0\}$ HA-protein absorption studies cited above it was thought that this film deposition process might enable a novel route to further functionalize the film surface with bioactive crystallographic faces. More specifically, engineering the orientation of hexagonal HA crystals may, together with aspect ratio and crystal spacing, enable the ratio of $\{10\bar{1}0\}/\{0001\}$ faces presented to the extracellular fluid to be altered, allowing modulation of HA protein adhesion, bioactivity, and potentially properties such as implant integration and healing time. For example, the crystals that compose the 10 h film have an aspect ratio of approximately 1, no spacing in between the crystals, and a nominally random [0001] orientation indicating that there is likely a nominally equal representation of $\{10\bar{1}0\}$ and $\{0001\}$ planes on the film surface. The crystals that compose the 24-h film have a larger aspect ratio, a large volume fraction of crystals at $2\theta = 0\ °$, and spacing between crystals, potentially creating a large $\{10\bar{1}0\}/\{0001\}$ ratio. In addition to the crystal face specific protein absorption data cited above, others have demonstrated that self-directed HA protein absorption and matrix formation from serum increases cell attachment and spreading as compared to HA surfaces functionalized with integrin binding (RGD) and proteoglycan binding peptides [68], indicating that HA contains all the surface functionalization cues necessary for efficient protein adhesion, initial matrix formation, and cell attachment within its own crystal structure. Thus, it was

hypothesized that HA contains surface functionalization cues for protein adhesion, initial matrix formation, and cell attachment within its own crystal structure, and that these cues maybe accentuated by engineering both crystal morphology and crystallographic orientation.

Analysis of MC3T3-E1 subclone 4 pre-osteoblast spreading, metabolic activity (Alamar Blue™ assay), and differentiation was not able to affirm the hypothesis above. These studies found no significant difference in bioactivity on films synthesized for 10 h that have a nominally random [0001] crystallographic orientation, for 24 h that have a [0001] orientation several multiples greater than expected for a randomly oriented sample at $2\theta = 0\ °$, or for 14 h that have an intermediate [0001] texture [58]. This finding may be due to a number of reasons. One potential explanation is that bioactivity, as measured in this study, may not be sensitive to the limited [0001] orientation differences of the 10, 14, and 24 h samples. If samples representing more limiting cases of [0001] orientation could be crystallized, such that all crystals were oriented at $2\theta = 0\ °$ or $2\theta = 90\ °$ and only the $\{10\bar{1}0\}$ or the {0001} were, respectively, displayed to the extracellular fluid, a significant increase in bioactivity on the former sample might still be expected. Figure 4.7 graphically displays these limiting cases. It is also feasible that although care was taken to account for both surface roughness and [0001] crystallographic orientation, the effect of these variables masked each other. As evidence, Kim et al. has reported significant differences in cell proliferation between Ti surfaces that vary in surface roughness on the same scale as in the HA films reported here, ~1-3 μm. Thus, based on

surface roughness alone, a significant decrease in total metabolic activity with increasing surface roughness and synthesis time should be expected across the HA films.

It is also feasible that reported differences in $\{10\bar{1}0\}$ and {0001} protein adsorption are incompletely understood. For example, Fujisawa et al. reports that a number of acidic bone proteins including phosphophoryn, osteocalcin (bone Gla protein), osteonectin, and bone small proteoglycan II are all preferentially absorbed on the $\{10\bar{1}0\}$ equivalent plane *in vitro* [27]. However, Flade et al. reports preferential absorption of osteocalcin onto the {0001} equivalent plane *in vitro* [84]. Thus, there are inconsistencies in the literature regarding which plane specific proteins preferentially absorb to. One or a combination of three factors may explain differences in the results of Fujisawa et al. and Flade et al. The first factor is protein concentration. Fujisawa et al. utilized protein concentrations of 1-100 μg/mL for binding studies, while Flade et al. utilized a protein concentration of 250 μg/mL. Consequently, protein concentration differences of this magnitude have been demonstrated to affect protein-mineral interactions [85]. The second factor relates to the use of buffers. Fujisawa et al. utilized a trishydroxymethylaminomethane (Tris)-HCl/NaCl buffer, while Flade et al. utilized a Na_3PO_4/NaCl buffer at different salt concentrations. Consequently, changing concentrations of salts, especially phosphate salts, are known to modulate protein-HA absorption [86]. The third factor is the hydroxyapatite used for the binding experiments. Both manuscripts made a qualitative assessment of the HA crystal faces presented to the protein solutions in their experiments based on HA grain morphology. Neither manuscript explicitly characterizes the crystallography of the HA that is used for absorption experiments. This is in contrast to the films reported in this

study, which previously underwent a careful and detailed analysis including pole figure orientation analysis to determine the crystal faces presented to the extracellular fluid [58]. Consequently, the omission of a robust analysis of the crystallography of the HA utilized in each study confounds the resulting conclusions reached by Fujisawa et al. and Flade et al. Thus, its seems that more comprehensive and robust studies of the interaction of individual bone proteins in physiological solution with well-characterized HA crystals need to be undertaken.

Even if more comprehensive and robust studies of the interaction of individual bone proteins in physiological solution with specific HA crystal faces are undertaken, their applicability to the cellular or tissue scale bioactivity of implanted HA is unclear given the results of this manuscript. First, competitive protein absorption from serum, which contains numerous proteins is a different and much more complex process than single protein absorption experiments. HA is well known to bind numerous proteins regardless of specific crystallographic faces, which is why HA is used as a substrate in protein chromatography. Under physiological conditions, a single protein will absorb onto the surface of HA in the presence of numerous other serum proteins and bio-molecules after implantation. This competitive absorption means that the proteins that absorb to HA non-specifically may inhibit or severely limit the crystallographic face specific protein absorption observed in single protein experiments. At the tissue level, the cell-mediated formation of cement lines at HA implant interfaces noted above may further make HA crystallographic face specific protein absorption a mute point. Thus, while crystallographic face specific protein absorption experiments may help model and explain

phenomenon such as the nucleation and growth of individual mineral crystals, it may not be applicable to phenomenon such as bulk implant bioactivity given the results of this manuscript.

Conclusions

The high crystallinity, Ca-P phase-pure, adhesive, passivating, HA films deposited by TEP/EDTA doubly regulated hydrothermal crystallization on Ti6Al4V substrates examined in this study were found to be non-toxic, biocompatible, bioactive, osteoconductive, and bone bonding. Differences in the [0001] crystallographic orientation of the hexagonal HA single crystals, which compose the film, were not found to cause a significant difference in these parameters. The lack of significant bioactivity differences indicates that there may be no relationship between HA crystallographic face specific protein absorption and bulk HA bioactivity. Nonetheless, based on material and biological properties it is concluded that these films should be considered as candidates for use on clinical Ti6Al4V orthopedic implants.

Acknowledgements

We gratefully acknowledge the research support by the Rutgers Center for Ceramic Research, the National Science Foundation/Rutgers IGERT on Biointerfaces, which supported both D.J. Haders and C.C. Kazanecki, the Department of Education/Rutgers GAANN in Molecular, Cellular, and Nanosystems Bioengineering, the Rutgers University Graduate School New Brunswick, the New Jersey Center for Biomaterials, the Rutgers University Roger G. Ackerman Fellowship, and the Rutgers University

Technology Commercialization Fund. The authors wish to thank Valentin Starovoytov for sputter coating biological specimens.

Abbreviations

HA – Hydroxyapatite
PS-HA – Plasma sprayed hydroxyapatite
EDTA – Ethylenediamine-tetraacetic acid, $C_{10}H_{16}N_2O_8$
TEP - Triethyl phosphate, $C_6H_{15}O_4P$
Ca-P – Calcium-Phosphate
XRD – X-Ray diffraction
FESEM – Field emission scanning electron microscopy
TCP – Tissue culture plastic
PDF – Powder diffraction file
Ti6Al4V - Alloyed titanium with 6 wt.% aluminum and 4 wt.% vanadium
(*hkil*) – Hexagonal crystallographic plane Miller indices
{*hkil*} – Equivalent hexagonal crystallographic plane Miller indices
[*uvtw*] – Hexagonal crystallographic direction

Tables

Table 4.1 Substrate surface roughness (Ra)

Substrate	Roughness, Ra (nm)
Ti6Al4V	414 +/- 81*
R-Ti6Al4V	3569 +/- 1014*
10 h	1096 +/- 87
14 h	2025 +/- 445
24 h	2975 +/- 600

* Data presented previously in Haders et al.

Captions for Figures

Figure 4.1 Scanning electron micrographs of MC3T3-E1 subclone 4 p.17 pre-osteoblast cell spreading on substrates after 3 days in cell culture: (a) Ti6Al4V, (b) grit-blasted Ti6Al4V, (c) HA 10 h, (d) HA 14 h, (e) HA 24 h.

Figure 4.2 Total Cell Metabolic activity of MC3T3-E1 subclone 4 p.15 osteoblast-like cells on various substrates as a fraction of TCP control from 0 – 28 d measured using the Alamar Blue™ biochemical assay. * Indicates statistically significant ($p<0.05$) difference in measured cell activity between substrate types at a specific time point.

Figure 4.3 Scanning electron micrographs of MC3T3-E1 subclone 4 p.15 osteoblast-like cells and their deposited extracellular matrix on various substrates after 105 d in culture: (a) TCP, (b) Ti6Al4V, (c) grit-blasted Ti6Al4V, (d) HA 10 h, (e) HA 14 h, (f) HA 24 h.

Figure 4.4 X-ray diffraction patterns of biomineral harvested from various substrates seeded with MC3T3-E1 subclone 4 p.15 osteoblast-like cells after 98 d in culture: (a) TCP, (b) Ti6Al4V, (c) grit-blasted Ti6Al4V.

Figure 4.5 Scanning electron micrographs of biomineral harvested from various substrates seeded with MC3T3-E1 subclone 4 p.15 osteoblast-like cells after 98 d in culture: (a) TCP, (b) Ti6Al4V, (c) grit-blasted Ti6Al4V.

Figure 4.6 Scanning electron micrographs of biomineral on the surface of various substrates seeded with MC3T3-E1 subclone 4 p.15 osteoblast-like cells after 98 d in culture: (a) HA 10 h, (b) HA 14 h, (c) HA 24 h.

Figure 4.7 Limiting cases of [0001] preferred orientation of HA films composed of hexagonal single crystals of HA (a) A HA film composed of hexagonal single crystals with all crystals having a preferred [0001] orientation at $2\theta = 0\ ^\circ$ will only present {0001} crystallographic faces to the body. (b) A HA film composed of hexagonal single crystals with all crystals having a preferred [0001] orientation at $2\theta = 90\ ^\circ$ will only present $\{10\bar{1}0\}$ crystallographic faces to the body. (c) Indexed micrograph of HA film from Figure 4.1e.

Figures

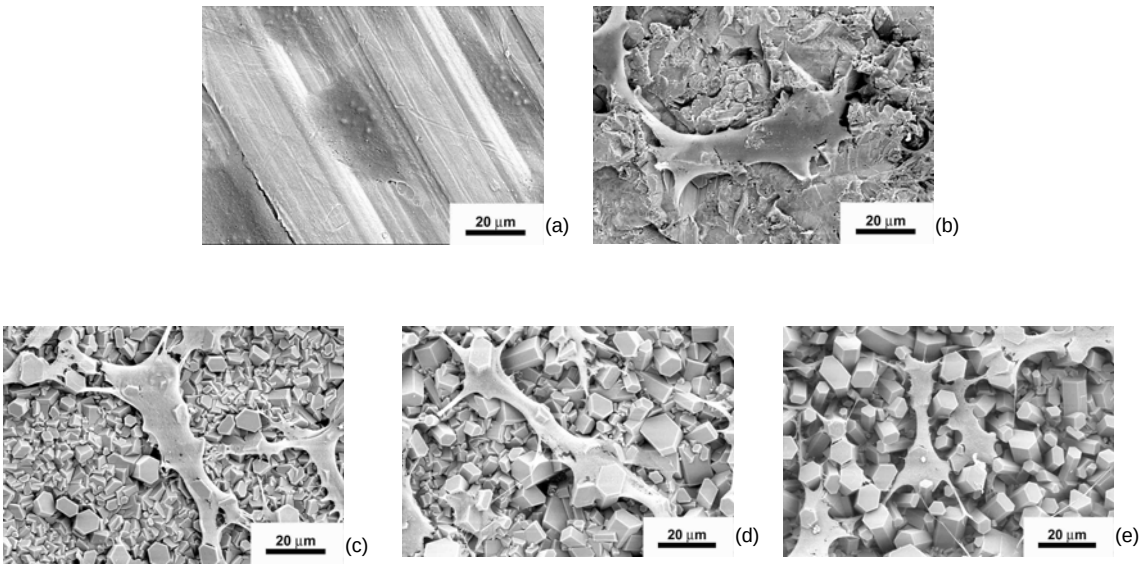

Figure 4.1

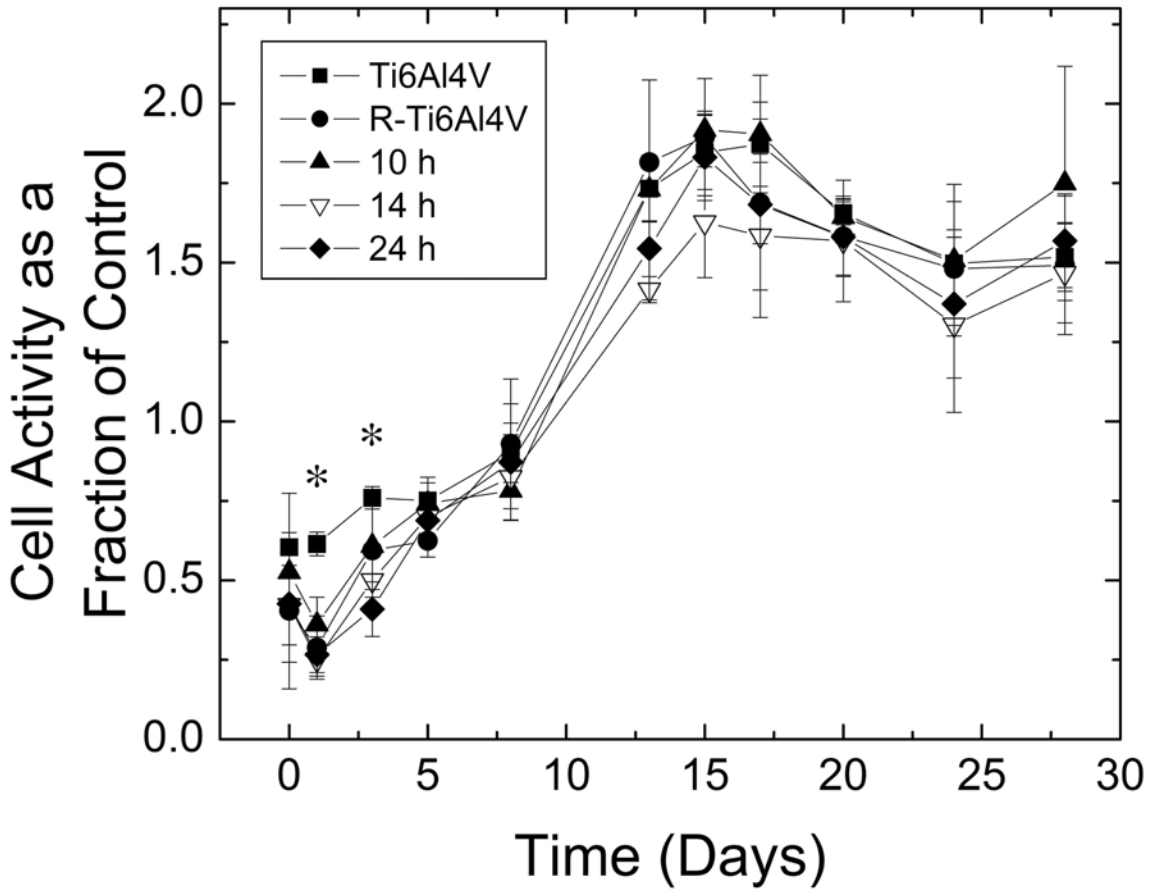
Ti6Al4V
R-Ti6Al4V
10 h
14 h
24 h
Cell Activity as a Fraction of Control
Time (Days)
0.0
0.5
1.0
1.5
2.0
0
5
10
15
20
25
30
*
*

Figure 4.2

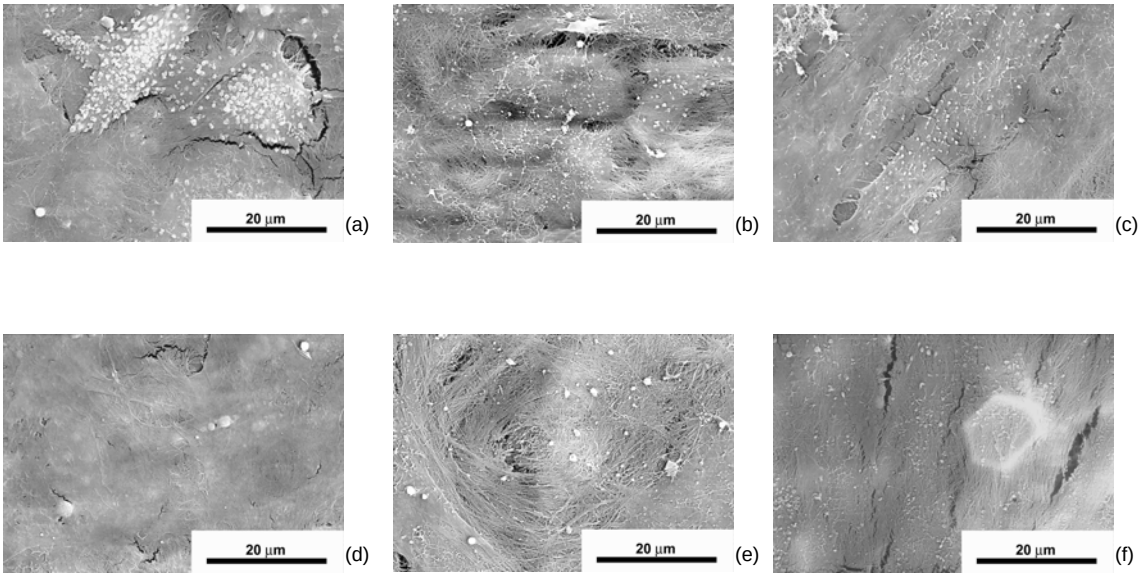

Figure 4.3

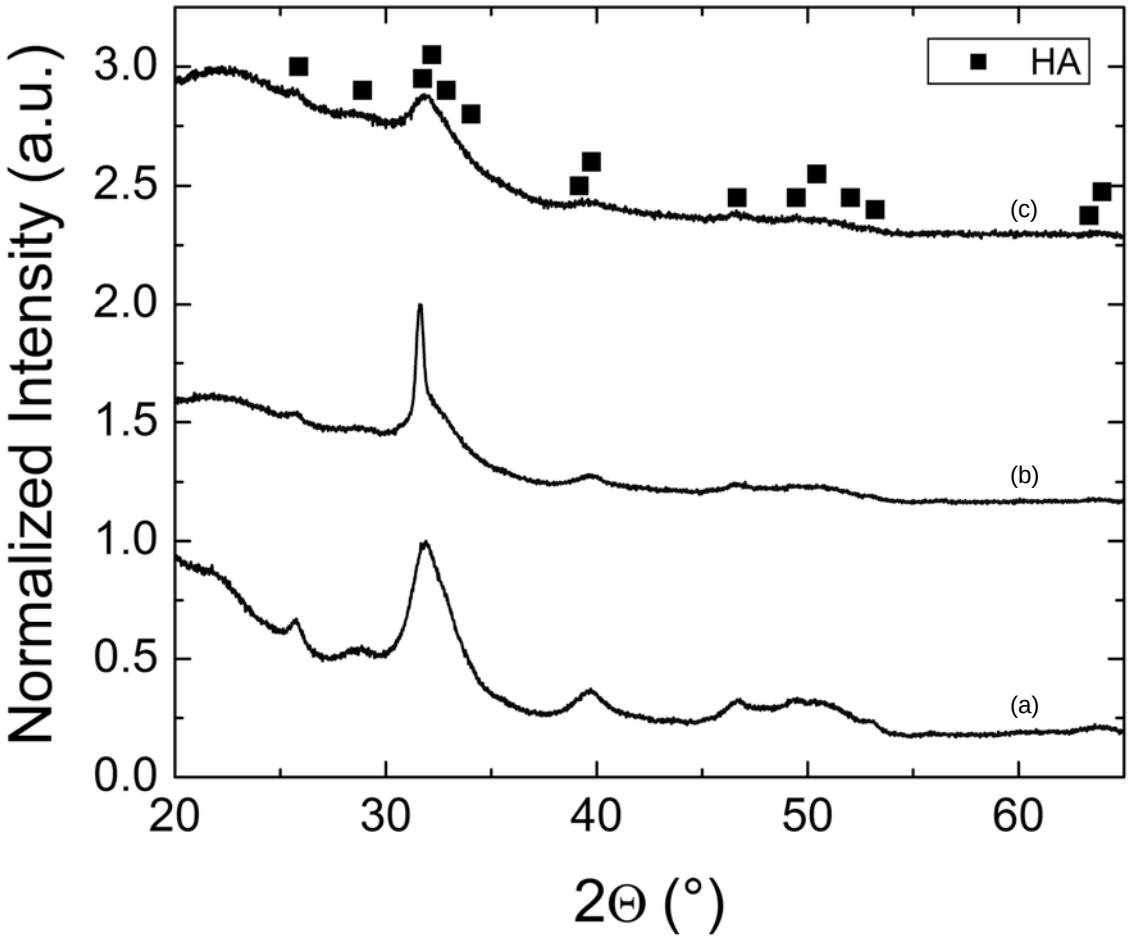
HA
(c)
(b)
(a)
Normalized Intensity (a.u.)
3.0
2.5
2.0
1.5
1.0
0.5
0.0
20
30
40
50
60
2Θ (°)

Figure 4.4

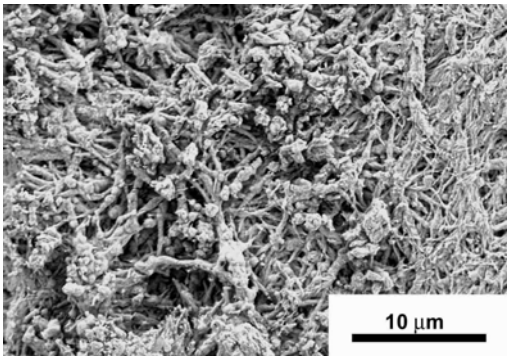

(a)

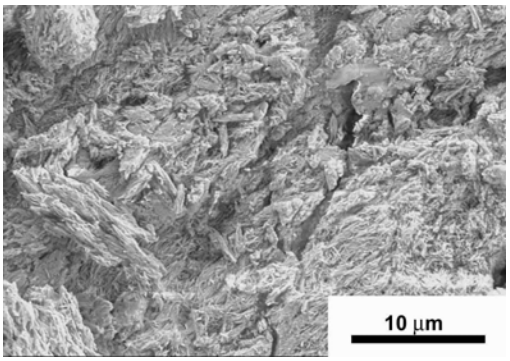

(b)

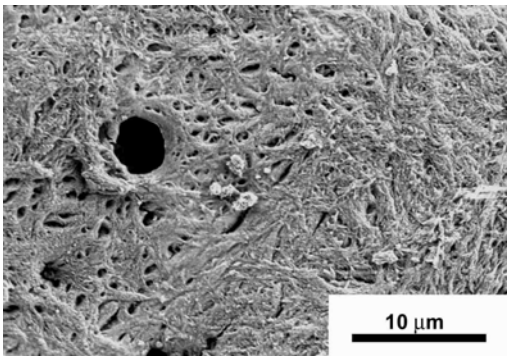

(c)

Figure 4.5

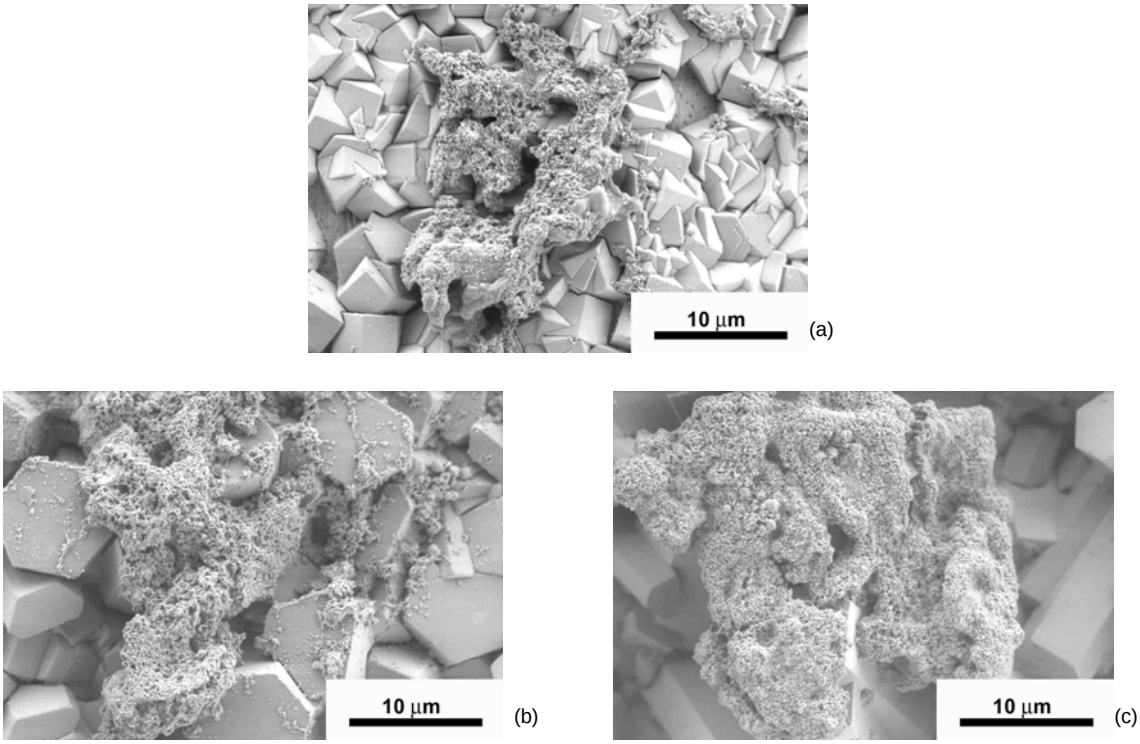

Figure 4.6

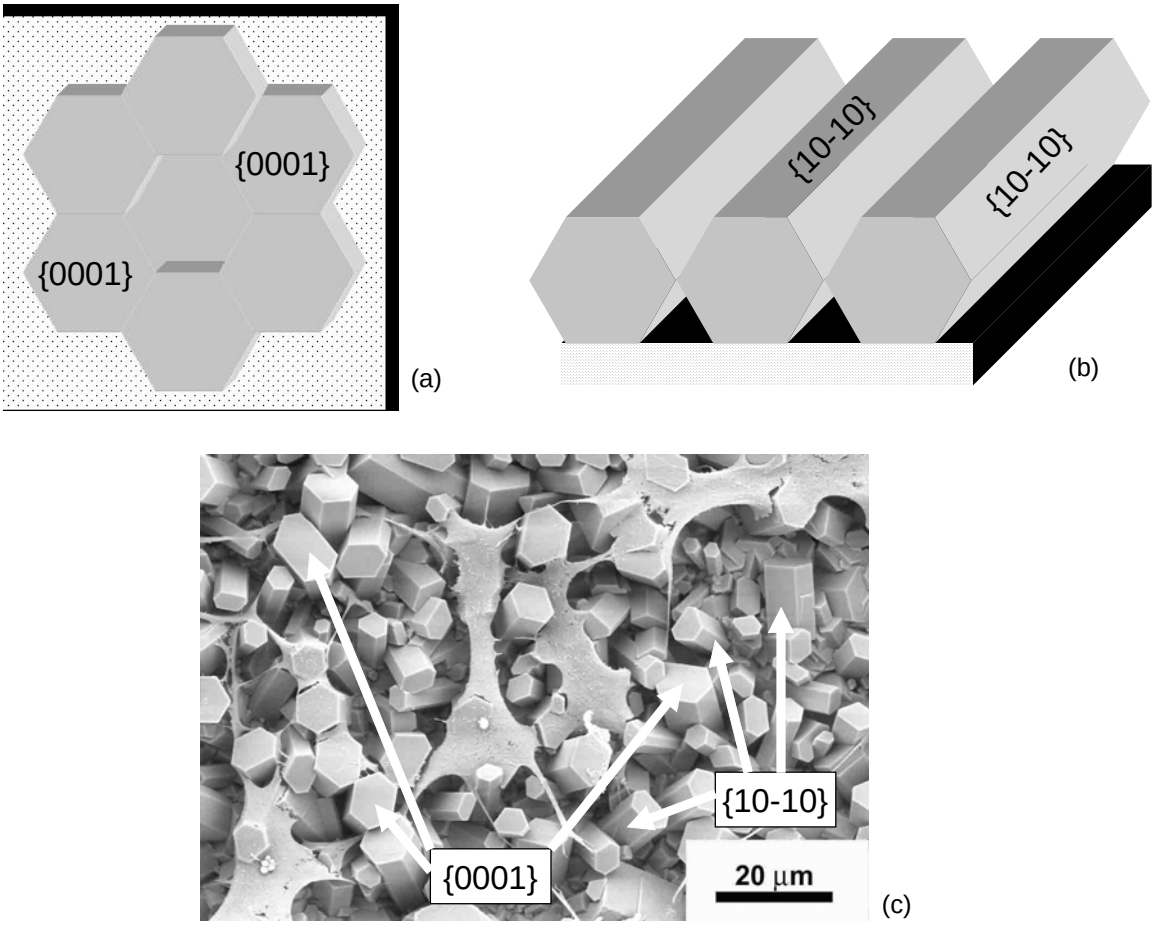

Figure 4.7

Chapter 5

CONCLUSIONS

The goal of this dissertation was to intelligently synthesize and characterize the material and biological properties of HA films on metallic substrates synthesized by hydrothermal crystallization, using thermodynamic phase diagrams as the starting point. In three overlapping interdisciplinary studies the potential of using EDTA/TEP doubly regulated hydrothermal crystallization to deposit HA films, the TEP-regulated, time-and-temperature-dependent process by which films were deposited, and the bioactivity of crystallographically engineered films were investigated.

The goal of initial study was to investigate the use of $Ca(EDTA)^{2-}$ and tri-ethyl phosphate (TEP) to regulate the hydrothermal crystallization of hydroxyapatite (HA) films. HA was coated on various substrates including titanium, Ti6Al4V, grit-blasted Ti6Al4V, 316 stainless steel, and Co28Cr6Mo via hydrothermal synthesis at 200 °C for 24 h utilizing a 0.232 molal $Ca(NO_3)_2$-0.232 molal EDTA-0.187 molal TEP-1.852 molal KOH - H_2O chemical system. The role of film deposition processing variables on HA crystallization was studied using thermodynamic process simulation and experimental TEP hydrolysis kinetics data. Profilometry, XRD, FESEM, and adhesion testing (ASTM D3359) were used to characterize substrates and films. Kinetics studies of TEP hydrolysis revealed that phosphate was available for the formation of HA at temperatures above 180 °C and synthesis times greater than 4 h. Thermodynamic modeling demonstrated both that the formation of phase pure HA was thermodynamically favored at 200 °C on all substrates and that the equilibrium concentration of free Ca^{2+} was lower in this system than in

hydrothermal HA film crystallization systems reported elsewhere. Materials characterization results indicated that high crystallinity (99+ %), (0002) crystallographically oriented, passivating, Ca-P (calcium-phosphate) phase pure HA films composed of hexagonal faceted grains (8-12 μm diameter) were formed on all substrates. Based on these results, it was concluded that the use of TEP necessitates a continuous two-step film deposition process that deposits phase pure HA at temperatures above 180 °C. The use of $Ca(EDTA)^{2-}$/pH regulation of Ca^{2+} concentration enables the hydrothermal HA crystallization process to be growth dominated, producing films composed of high crystallinity, hexagonal grains.

The aim of the second study was to investigate the use of tri-ethyl phosphate (TEP) to regulate the hydrothermal crystallization of hydroxyapatite (HA) films onto Ti6Al4V substrates. The growth mechanism of the HA film and development of [0001] HA crystallographic texture were studied. Films were crystallized in a 0.232 molal $Ca(NO_3)_2$-0.232 molal EDTA-0.187 molal TEP–1.852 molal KOH-H_2O chemical system with a final isothermal temperature of 200 °C, and then evaluated at synthesis times from 0-46 h by XRD, FESEM, TEM, EDX, and X-ray pole figures. Thermodynamic phase stability diagrams were calculated to validate experimental findings. XRD, FESEM, TEM, and EDX results demonstrated the crystallization of a $CaTiO_3$ film below 180 °C and a HA film above 180 °C. SEM and X-ray pole figure analysis revealed a refinement of the orientation of the (0002) HA crystallographic plane and the c-axis of hexagonal single crystals of HA, [0001], with increasing synthesis time. Based on these results it was concluded that the use of TEP-regulated hydrothermal crystallization enabled the

deposition of $CaTiO_3$, and then HA in a single, phase-sequenced process, the first such process reported in the hydrothermal HA literature. The HA film was deposited by means of a competitive growth mechanism that enabled the [0001] crystallographic orientation of hexagonal single crystals to be engineered with synthesis time.

The aim of the final study was to evaluate the bioactivity of adhesive, passivating, hydroxyapatite (HA) films composed of hexagonal single crystals that display $\{10\bar{1}0\}$ and {0001} HA crystallographic faces. The effect of engineered [0001] crystallographic orientation (texture) on film bioactivity was investigated in parallel. Films were deposited by TEP/EDTA doubly regulated hydrothermal crystallization on Ti6Al4V substrates for 10, 14, and 24 h. The general bioactivity of HA films was investigated by analysis of MC3T3-E1 pre-osteoblast spreading using SEM and quantitative analysis of total cell metabolic activity (Alamar Blue™ assay) from 0 – 28 d. SEM and XRD were used to evaluate the ability of films to support the differentiation of MC3T3-E1 pre-osteoblasts into mature, matrix-secreting, mineralizing osteoblasts. Substrates with known biocompatibility, namely tissue culture plastic (TCP), polished Ti6Al4V, and roughened Ti6Al4V, were evaluated for comparison. Results demonstrated that all HA films enabled MC3T3-E1 cells to spread, grow, and differentiate into matrix-secreting, mineralizing osteoblasts in a manner similar to HA films reported in the literature. Biomineral deposited on HA films could not be removed from the films after extraction of organic material by 6.15 vol% sodium hypochlorite. Differences in [0001] HA crystallographic orientation were not, however, found to significantly affect bioactivity. Based on these results, it was concluded that HA films synthesized by our process are non-toxic,

bioactive, osteoconductive, and bone bonding. The demonstrated crystallinity, phase purity, passivation, and adhesion properties of these films taken together with these biological results indicate that they are candidates for use on clinical orthopedic implants. Our results also indicate that there is no significant relationship between reported HA crystallographic face specific protein absorption and bulk HA bioactivity.

In summary, this dissertation demonstrates that thermodynamic process simulation facilitates the engineering of hydrothermal processes for the development of designer hydroxyapatite films. More specifically, results demonstrate that EDTA/TEP doubly regulated hydrothermal crystallization may be successfully used to deposit inexpensive, reproducible, high crystallinity, phase-pure, adhesive, passivating, conformal, hexagonal grained, bioactive, bone-bonding HA films on a number of metallic substrates, including the clinically used Ti6Al4V alloy. Based on a review of the literature, these characteristics represent an improvement over current HA films for orthopedic implants applied using the plasma spray method. Therefore, it may be concluded that these films are potential candidates for use on clinical Ti6Al4V orthopedic implants.

Chapter 6

FUTURE WORK

A number of research projects may be initiated based on the findings of this dissertation. A further investigation into the affect of crystallography and crystal orientation on bioactivity and mineralization that 1) examines the adhesion of fluorescently tagged extracellular proteins to the HA film and/or 2) examines the crystallographic relation between the film and the bio-mineral may be warranted. It may be appropriate to explore non-biological applications for these films that capitalize on the passivation properties, adhesion properties, and the chemical stability of the films such as corrosion barriers. In addition, the hexagonal crystal morphology and [0001] engineered crystallographic orientation of the films may be applicable to chromatography. However, to further investigate the potential of these films to serve as coatings on metallic orthopedic substrates and to investigate potential methods to improve the properties of the current films three specific studies are proposed.

In vivo animal studies of film bioactivity, and mechanical and chemical properties should be investigated in the near-term. The results of this dissertation demonstrate that that EDTA/TEP doubly regulated hydrothermal crystallization may be successfully used to deposit inexpensive, reproducible, high crystallinity, phase pure, adhesive, passivating, conformal, hexagonal grained, bioactive, bone-bonding HA films on a number of metallic substrates, including the clinically used Ti6Al4V alloy *in vitro*. Based on a review of the literature, these characteristics represent an improvement over current HA films for orthopedic implants applied using the plasma spray method. From this examination it

may be concluded then that these films should be considered as potential candidates for use on clinical metallic orthopedic implants. Thus, *in vivo* animal testing is the first step required to determine if this potential will translate to real improved health and health care for patients with applicable orthopedic conditions.

Film bioactivity may potentially be improved by creating a multi-layer Ca-P film. The multi-layer structure would utilize the film reported in this dissertation as the base layer. A resorbable Ca-P layer, such as low crystallinity HA or tri-calcium phosphate (TCP), capable of releasing Ca^{2+} and PO_4^{3-} in a controlled manner would then be deposited upon the initial film. Extracellular Ca^{2+} has been shown to have a positive dose-dependent affect on DNA synthesis, proliferation, in an osteoblastic rat cell line, rat calvaria cells, and MC3T3-E1 cells [87-89]. Extracellular Ca^{2+} has also been shown to increase chemeotaxis, alkaline phosphatase activity, osteocalcin expression, total protein, sodium-dependent phosphate uptake, COX-2 expression, TGF-β1 expression, and prostaglandin E_2 (PGE_2) production, while also inducing phosphorylation of extracellular signal regulated kinase (ERK) in multiple osteoblast sources [87,88,90,91]. Extracellular inorganic phosphate has been shown to independently regulate gene expression, including osteopontin, through the ERK1/2 MAP kinase pathway, in a manner that closely resembles typical osteoblast differentiation [92-95]. Blocking of cellular membrane Na-dependent phosphate transporters, the primary mechanism for phosphate entry, has been shown to inhibit both phosphate-mediated gene regulation and mineralization [92-94]. In opposition to these studies one group has published work stating that inorganic phosphate induces apoptosis in osteoblasts in a time and dose-dependent (1-7mM) manner and that

Ca^{2+} causes an enhancement of the effect [96,97]. However, blocking Ca^{2+} channels exerted no affect on apoptosis, and using inorganic phosphate in the same doses produced no such affect in other studies noted above [92,94,95]. Thus, the controlled release of Ca^{2+} and PO_4^{3-} from a multilayer HA structure represent a potential pathway to increase the bioactivity of the films described in this dissertation, without sacrificing any of the properties of the film.

In addition to up regulating osteoblast behavior, the controlled release of extracellular Ca^{2+} may down regulate osteoclast activity. Osteoclastic bone resorption, as measured by resorption pit area and number, has been shown to be affected by Ca^{2+} in a negative dose-dependent manner between 0-20mM Ca [98,99]. Super oxide anion (O_2^-) production, thought to facilitate collagen fibril disruption allowing enzyme digestion by osteoclasts is also down-regulated by increased extracellular Ca concentration [100]. Inorganic phosphate (Pi) has been shown to inhibit osteoclast cell formation and bone resorbing activity [93,98]. Together, the up-regulation of osteoblast activity and the down-regulation of osteoclast activity may enable post-implantation bone remodeling to favor bone deposition rather than resorption, potentially decreasing implant fixation and patient recovery time.

Bacterial infection after implantation is a painful and costly complication in orthopedics often leading to implant failure. To decrease the infection rate and resulting failure rate of the HA coatings developed in this dissertation, anti-bacterial agents may be incorporated into the primary coating or any multi-layer coatings, as suggested above, such that the HA film becomes a drug delivery vehicle. One potential method to reduce infection rates

in this manner is to introduce metal ions, particularly silver (Ag). Ag incorporation into HA films has been demonstrated to reduced the number of the RP12 strain of *Staphylococcus epidermidis* (ATCC 35984) and the Cowan I strain of *Staphylococcus aureus* on Ag-HA surfaces when compared to titanium and HA surfaces without affecting the proliferation or differentiation of human embryonic palatal mesenchyme cells on the same films [101,102]. Incorporation of Ag or zinc (Zn) into HA films has been shown to create a dose-dependent growth inhibition zone for *Streptococcus mutans* around films [103]. Elsewhere, however, only Ag-HA was found to reduce the number of *Escherichia coli* in a study that included Zn-HA and copper(Cu)-HA [104]. Antibiotics may also be incorporated into HA films to fight infection. For example, gentamicin crobefat-loaded and vancomycin-loaded hydroxyapatite packed into rabbit osteomyelitic bone defects have demonstrated a significant reduction in infection over controls and other delivery vehicles [105,106]. Other antibiotics and anti-bacterials have also been incorporated into HA films to combat infection including, but not limited to, gentamicin sulphate, lactoferrin, tetracycline, and gatifloxacin [107,108]. Beyond fighting infection, these HA films could be used to deliver other drugs that reduce pain and swelling, up- or down-regulate cells, etc. at the implantation site.

The results of this dissertation project may be used to seed a number of additional projects related to protein adhesion and cell biology or applications such as corrosion barriers and chromatography. In terms of orthopedic applications the currently reported films may be improved through the creation of a multi-layer structure and/or incorporation of anti-bacterial agents or other drugs into that structure. In the near-term,

however, the results of this dissertation necessitate that an *in vivo* animal study be performed to validate the potential of these films to improve the health and health care of patients with applicable orthopedic conditions.

Chapter 7

BIBLIOGRAPHY

(1) Daculsi, G.; Bouler, J. M.; LeGeros, R. Z. *Int Rev Cytol* **1997**, *172*, 129-191.
(2) Sun, L.; Berndt, C. C.; Gross, K. A.; Kucuk, A. *J Biomed Mater Res* **2001**, *58*, 570-592.
(3) Suchanek, W.; Yoshimura, M. *Journal of Materials Research* **1998**, *13*, 94-117.
(4) Porter, A. E.; Taak, P.; Hobbs, L. W.; Coathup, M. J.; Blunn, G. W.; Spector, M. *Biomaterials* **2004**, *25*, 5199-5208.
(5) Dunn, M. G.; Maxian, S. H. *J Long Term Eff Med Implants* **1991**, *1*, 193-203.
(6) Spivak, J. M.; Ricci, J. L.; Blumenthal, N. C.; Alexander, H. *J Biomed Mater Res* **1990**, *24*, 1121-1149.
(7) Bauer, T. W.; Schils, J. *Skeletal Radiol* **1999**, *28*, 423-432.
(8) Capello, W. N.; D'Antonio, J. A.; Manley, M. T.; Feinberg, J. R. *Clin Orthop Relat Res* **1998**, 200-211.
(9) Thomas, K. A. *Orthopedics* **1994**, *17*, 267-278.
(10) LeGeros, R. Z.; Craig, R. G. *J Bone Miner Res* **1993**, *8 Suppl 2*, S583-596.
(11) Dumbleton, J.; Manley, M. T. *J Bone Joint Surg Am* **2004**, *86-A*, 2526-2540.
(12) Geesink, R. G. *Clin Orthop Relat Res* **2002**, 53-65.
(13) Cheang, P.; Khor, K. A. *Biomaterials* **1996**, *17*, 537-544.
(14) Tsui, Y. C.; Doyle, C.; Clyne, T. W. *Biomaterials* **1998**, *19*, 2015-2029.
(15) Dalton, J. E.; Cook, S. D. *J Biomed Mater Res* **1995**, *29*, 239-245.
(16) Park, E.; Condrate, R. A.; Hoelzer, D. T.; Fischman, G. S. *J Mater Sci Mater Med* **1998**, *9*, 643-649.
(17) Ji, H.; Ponton, C. B.; Marquis, P. M. *J Mat. Sci. Mat. Med.* **1992**, *3*, 283-287.
(18) Klein, C. P.; Wolke, J. G.; de Blieck-Hogervorst, J. M.; de Groot, K. *J Biomed Mater Res* **1994**, *28*, 909-917.
(19) Filiaggi, M. J.; Coombs, N. A.; Pilliar, R. M. *J Biomed Mater Res* **1991**, *25*, 1211-1229.
(20) Kangasniemi, I. M.; Verheyen, C. C.; van der Velde, E. A.; de Groot, K. *J Biomed Mater Res* **1994**, *28*, 563-572.
(21) Lin, H.; Xu, H.; Zhang, X.; de Groot, K. *J Biomed Mater Res* **1998**, *43*, 113-122.
(22) Browne, M.; Gregson, P. J. *Biomaterials* **2000**, *21*, 385-392.
(23) Okazaki, Y.; Gotoh, E.; Manabe, T.; Kobayashi, K. *Biomaterials* **2004**, *25*, 5913-5920.
(24) Puleo, D. A.; Huh, W. W. *J Appl Biomater* **1995**, *6*, 109-116.

(25) Kirkham, J.; Brookes, S. J.; Shore, R. C.; Wood, S. R.; Smith, D. A.; Zhang, J.; Chen, H.; Robinson, C. *Current Opinion in Colloid & Interface Science* **2002**, *7*, 124-132.
(26) Huq, N. L.; Cross, K. J.; Reynolds, E. C. *J Mol. Mod* **2000**, *6*, 35-47.
(27) Fujisawa, R.; Kuboki, Y. *Biochim Biophys Acta* **1991**, *1075*, 56-60.
(28) Wang, D.; Chen, C.; Liu, X.; Lei, T. *Colloids Surf B Biointerfaces* **2007**, *57*, 237-242.
(29) van Dijk, K.; Schaeken, H. G.; Wolke, J. G.; Jansen, J. A. *Biomaterials* **1996**, *17*, 405-410.
(30) Ong, J. L.; Lucas, L. C. *Biomaterials* **1994**, *15*, 337-341.
(31) Garcia, F.; Arias, J. L.; Mayor, B.; Pou, J.; Rehman, I.; Knowles, J.; Best, S.; Leon, B.; Perez-Amor, M.; Bonfield, W. *J Biomed Mater Res* **1998**, *43*, 69-76.
(32) Jonasova, L.; Muller, F. A.; Helebrant, A.; Strnad, J.; Greil, P. *Biomaterials* **2004**, *25*, 1187-1194.
(33) Byrappa, K.; Yoshimura, M. *Handbook of Hydrothermal Cystallization*; Noyes Publications: Park Ridge, NJ, 2001.
(34) Riman, R. E.; Suchanek, W. L.; Lencka, M. M. *Annales de Chimie (Science des Materiaux)* **2002**, *27*, 15-36.
(35) Ohba, Y.; Watanabe, T.; Sakai, E.; Daimon, M. *Journal of the Ceramic Society of Japan* **1999**, *107*, 907-912.
(36) Toriyama, M.; Kawamoto, Y.; Suzuki, T.; Yokogawa, Y.; Nishizawa, K.; Nagata, F.; Mucalo, M. R. *Journal of Materials Science Letters* **1996**, *15*, 179-181.
(37) Jung-Soo Ha. Rahaman, M. N. *Ceramic Engineering and Science Proceedings* **2003**, *24*, 239-244.
(38) Fujishiro, Y.; Sato, T.; Okuwaki, A. *Journal of Materials Science: Materials in Medicine* **1995**, *6*, 172-176.
(39) Fujishiro, Y.; Sugimori, A.; Okuwaki, A.; Sato, T. *J Mater Sci Mater Med* **2001**, *12*, 333-337.
(40) Fujishiro, Y.; Fujimoto, A.; Sato, T.; Okuwaki, A. *Journal of Colloid and Interface Science* **1995**, *173*, 119-127.
(41) Fujishiro, Y.; Sato, N.; Uchida, S.; Sato, T. *J Mater Sci Mater Med* **1998**, *9*, 363-367.
(42) Ha, J. S.; Rahaman, M. N. *Ceramic Engineering and Science Proceedings* **2003**, *24*, 239-244.
(43) Klein, C.; Hurlbut, C.; Dana, J. D. *John Wiley & Sons* **1985**, *20th ed*.
(44) Andres-Verges, M.; Fernandez-Gonzales, C.; Martinez-Gallego, M. *Journal of Ihe European Ceramic Sociefy* **1998**, *18*, 1245-1250.
(45) Fujishiro, Y.; Yabuki, H.; Kawamura, K.; Sato, T.; Okuwaki, A. *Journal of Chemical Technology and Biotechnology* **1993**, *57*, 349-353.
(46) Shu, P.; Schmitt, K. *Colloids and Surfaces A: Physicochemical and Engineering Aspects* **1996**, *110*, 273-285.
(47) Barnard, P. W. C.; Bunton, C. A.; Llewellyn, D. R.; Vernon, C. A.; Welch, V. A. *J. Chem. Society* **1961**, 2670.
(48) Kumamoto, J.; Cox, J. R.; Westheimer, F. H. *Journal of the American Chemical Society* **1956**, *78*, 4858 - 4860.

(49) Zhu, P.; Masuda, Y.; Koumoto, K. *Biomaterials* **2004**, *25*, 3915-3921.
(50) Takadama, H.; Kim, H.; Kokubo, T.; Nakamura, T. *Chemistry of Materials* **2001**, *13*, 1108 - 1113.
(51) Riman, R. E.; Suchanek, W. L.; Byrappa, K.; C.W., C.; Shuk, P.; Oakes, C. S. *Solid State Ionics, Diffusion & Reactions* **2002**, *151*, 393-402.
(52) Boskey, A. L.; Posner, A. S. *Orthop Clin North Am* **1984**, *15*, 597-612.
(53) Lencka, M. M.; Riman, R. E. *Chemistry of Materials* **1993**, *5*, 61-70.
(54) Fulmer, M. T.; Ison, I. C.; Hankermayer, C. R.; Constantz, B. R.; Ross, J. *Biomaterials* **2002**, *23*, 751-755.
(55) Zwicky, F. *Reviews of Modern Physics* **1934**, *6*, 193-208.
(56) Ha, J. S. *Journal of the Korean Ceramic Society* **2003**, *40*, 1154-1158.
(57) Jones, J. L.; Slamovich, E. B.; Bowman, K. J. *Journal of Materials Research* **2004**, *19*, 3414-3422.
(58) Haders, D. J.; Burukhin, A.; Huang, Y.; Cockayne, D. J. H.; Riman, R. E. *In Preparation* **2008**.
(59) Thompson, C. V. *Annual Review of Materials Science* **2000**, *30*, 159-190.
(60) Nainville, I.; Lemarchand, A.; Badiali, J.-P. *Physical Review E. Statistical Physics, Plasmas, Fluids, and Related Interdisciplinary Topics* **1996**, *53*, 2537-2546.
(61) Ji H, P. C., Marquis PM. *J Mat. Sci. Mat. Med.* **1992**, *3*, 283-287.
(62) Haders, D.; Burukhin, A.; Zlotnikov, E.; Riman, R. E. *Accepted to Chemistry of Materials pending revisions* **2008**.
(63) Seabaugh, M. M.; Vaudin, M. D.; Cline, J. P.; Messing, G. L. *Journal of the American Ceramic Society* **2000**, *83*, 2049-2054.
(64) Hung, C. C.; Riman, R. E.; Caracciolo, R. *Ceramic Powder Science III* **1990**, 17-24.
(65) Pilliar, R. M. *Orthop Clin North Am* **2005**, *36*, 113-119.
(66) Haddad, R. J.; Cook, S. D.; Thomas, K. A. *J Bone Joint Surg Am* **1987**, *69*, 1459-1466.
(67) Galante, J. O.; Jacobs, J. *Clin Orthop Relat Res* **1992**, 41-49.
(68) Sawyer, A. A.; Hennessy, K. M.; Bellis, S. L. *Biomaterials* **2006**.
(69) Linez-Bataillon, P.; Monchau, F.; Bigerelle, M.; Hildebrand, H. F. *Biomol Eng* **2002**, *19*, 133-141.
(70) Kim, M. J.; Kim, C. W.; Lim, Y. J.; Heo, S. J. *J Biomed Mater Res A* **2006**, *79*, 1023-1032.
(71) Wang, D.; Christensen, K.; Chawla, K.; Xiao, G.; Krebsbach, P. H.; Franceschi, R. T. *J Bone Miner Res* **1999**, *14*, 893-903.
(72) Green, J. R.; Margerison, D. *Statistical Treatment of Experimental Data*; Elsevier Scientific Publishing Company: New York, 1978.
(73) Franceschi, R. T.; Iyer, B. S. *J Bone Miner Res* **1992**, *7*, 235-246.
(74) Chou, Y. F.; Huang, W.; Dunn, J. C.; Miller, T. A.; Wu, B. M. *Biomaterials* **2005**, *26*, 285-295.
(75) Soboyejo, W. O.; Nemetski, B.; Allameh, S.; Marcantonio, N.; Mercer, C.; Ricci, J. *J Biomed Mater Res* **2002**, *62*, 56-72.

(76) Ball, M. D.; Downes, S.; Scotchford, C. A.; Antonov, E. N.; Bagratashvili, V. N.; Popov, V. K.; Lo, W. J.; Grant, D. M.; Howdle, S. M. *Biomaterials* **2001**, *22*, 337-347.
(77) Thian, E. S.; Huang, J.; Best, S. M.; Barber, Z. H.; Bonfield, W. *Biomaterials* **2005**, *26*, 2947-2956.
(78) Ohgushi, H.; Dohi, Y.; Katuda, T.; Tamai, S.; Tabata, S.; Suwa, Y. *J Biomed Mater Res* **1996**, *32*, 333-340.
(79) Bagambisa, F. B.; Joos, U.; Schilli, W. *Journal of Biomedical Materials Research* **1993**, *27*, 1047 - 1055.
(80) de Bruijin, J. D.; Flach, J. S.; de Groot, K.; van Blitterswijk, C. A.; Davies, J. E. *Cells and Materials* **1993**, *3*, 115-127.
(81) Davies, J. E.; Baldan, N. *J Biomed Mater Res* **1997**, *36*, 429-440.
(82) de Bruijn, J. D.; Bovell, Y. P.; van Blitterswijk, C. A. *Biomaterials* **1994**, *15*, 543-550.
(83) Ducheyne, P.; Qiu, Q. *Biomaterials* **1999**, *20*, 2287-2303.
(84) Flade, K.; Lau, C.; Mertig, M.; Pompe, W. *Chemistry of Materials* **2001**, *13*, 3596-3602.
(85) Boskey, A. L.; Maresca, M.; Doty, S.; Sabsay, B.; Veis, A. *Bone Miner* **1990**, *11*, 55-65.
(86) Schmidt, S. R.; Schweikart, F.; Andersson, M. E. *J Chromatogr B Analyt Technol Biomed Life Sci* **2007**, *849*, 154-162.
(87) Schmid, C.; Keller, C.; Schlapfer, I.; Veldman, C.; Zapf, J. *Biochem Biophys Res Commun* **1998**, *245*, 220-225.
(88) Yamaguchi, T.; Chattopadhyay, N.; Kifor, O.; Butters, R. R., Jr.; Sugimoto, T.; Brown, E. M. *J Bone Miner Res* **1998**, *13*, 1530-1538.
(89) Quarles, L. D.; Hartle, J. E., 2nd; Siddhanti, S. R.; Guo, R.; Hinson, T. K. *J Bone Miner Res* **1997**, *12*, 393-402.
(90) Choudhary, S.; Wadhwa, S.; Raisz, L. G.; Alander, C.; Pilbeam, C. C. *J Bone Miner Res* **2003**, *18*, 1813-1824.
(91) Matsuoka, H.; Akiyama, H.; Okada, Y.; Ito, H.; Shigeno, C.; Konishi, J.; Kokubo, T.; Nakamura, T. *J Biomed Mater Res* **1999**, *47*, 176-188.
(92) Beck, G. R., Jr.; Moran, E.; Knecht, N. *Exp Cell Res* **2003**, *288*, 288-300.
(93) Beck, G. R., Jr. *J Cell Biochem* **2003**, *90*, 234-243.
(94) Beck, G. R. J.; Zerler, B.; Moran, E. *Proc Natl Acad Sci U S A.* **2000**, *97*, 8352-8357.
(95) Beck, G. R. J.; Knecht, N. *J Biol Chem* **2003**, *278*, 41921-41929.
(96) Meleti, Z.; Shapiro, I. M.; Adams, C. S. *Bone* **2000**, *27*, 359-366.
(97) Adams, C. S.; Mansfield, K.; Perlot, R. L.; Shapiro, I. M. *J Biol Chem* **2001**, *276*, 20316-20322.
(98) Yates, A. J.; Oreffo, R. O.; Mayor, K.; Mundy, G. R. *J Bone Miner Res* **1991**, *6*, 473-478.
(99) Kameda, T.; Mano, H.; Yamada, Y.; Takai, H.; Amizuka, N.; Kobori, M.; Izumi, N.; Kawashima, H.; Ozawa, H.; Ikeda, K.; Kameda, A.; Hakeda, Y.; Kumegawa, M. *Biochem Biophys Res Commun* **1998**, *245*, 419-422.
(100) Datta, H. K.; Manning, P.; Rathod, H.; McNeil, C. J. *Exp Physiol* **1995**, *80*, 713-719.

(101) Chen, W.; Liu, Y.; Courtney, H. S.; Bettenga, M.; Agrawal, C. M.; Bumgardner, J. D.; Ong, J. L. *Biomaterials* **2006**, *27*, 5512-5517.
(102) Chen, W.; Oh, S.; Ong, A. P.; Oh, N.; Liu, Y.; Courtney, H. S.; Appleford, M.; Ong, J. L. *J Biomed Mater Res A* **2007**, *82*, 899-906.
(103) Chung, R. J.; Hsieh, M. F.; Huang, C. W.; Perng, L. H.; Wen, H. W.; Chin, T. S. *J Biomed Mater Res B Appl Biomater* **2006**, *76*, 169-178.
(104) Kim, T. N.; Feng, Q. L.; Kim, J. O.; Wu, J.; Wang, H.; Chen, G. C.; Cui, F. Z. *J Mater Sci Mater Med* **1998**, *9*, 129-134.
(105) Shirtliff, M. E.; Calhoun, J. H.; Mader, J. T. *Clin Orthop Relat Res* **2002**, 239-247.
(106) Cornell, C. N.; Tyndall, D.; Waller, S.; Lane, J. M.; Brause, B. D. *J Orthop Res* **1993**, *11*, 619-626.
(107) Sanchez, E.; Baro, M.; Soriano, I.; Perera, A.; Evora, C. *Eur J Pharm Biopharm* **2001**, *52*, 151-158.
(108) Oyane, A.; Yokoyama, Y.; Uchida, M.; Ito, A. *Biomaterials* **2006**, *27*, 3295-3303.

Chapter 8

CURRICULUM VITA

Daniel Joseph Haders II

EDUCATION

2002 - Present

Ph.D., Interdisciplinary Doctoral Candidate

Rutgers, The State University of New Jersey

Department Biomedical Engineering & Department of Materials Engineering

New Brunswick, NJ, U.S.A.

- Dissertation Topic – Synthesis and Characterization of TEP-EDTA-Regulated Bioactive Hydroxyapatite

Fall 2005

Recognized Visiting Graduate Student

University of Oxford

Department of Materials

Oxford, England, U.K.

- Research Topic - Electron microscopy and microanalysis characterization of the hydroxyapatite/titanium interface for hydrothermally synthesized HA films.

1997 - 2001

B.S.

Columbia University, School of Engineering and Applied Science

Department of Biomedical Engineering (major)

Department of Materials Engineering (minor)

New York, NY

PUBLICATIONS

Ligler FS, Breimer M, Golden JP, Nivens DA, Dodson JP, Green TM, Haders DJ, Sadik OA., Integrating Waveguide Biosensor. Anal Chem 2002 Feb 1;74(3):713-719

Shaw TM, Jimerson D, Haders D, Murray CE, Grill A, Edelstein DC, Chidambarrao D. Moisture and Oxygen Uptake in Low k/Copper Interconnect Structures. Advanced Metallization Conference 2003 (AMC 2003), Mater Res Soc, 2004, 77-84.

Haders D.J., Burukhin A, Zlotnikov E, Riman R. E. TEP/EDTA Doubly Regulated Hydrothermal Crystallization of Hydroxyapatite Films on Metal Substrates. Submitted to Chemistry of Materials.

Haders D.J., Burukhin A, Huang Y, Cockayne D.J.H., Riman R. E. Phase Sequenced Deposition of Calcium Titanate/Hydroxyapatite Films with Controllable Crystallographic Texture onto Ti6Al4V by TEP Regulated Hydrothermal Crystallization. Submission to Crystal Growth and Design April 2008.

Haders D.J., Kazanecki C.C., Burukhin A, Denhardt D.T., Riman R.E. Crystallographically Engineered, Hydrothermally Crystallized Hydroxyapatite Films – an *In-vitro* Study of Bioactivity. Submission to Biomaterials April 2008.